OBSERVATION OF RESONANT ELECTRIC DIPOLE-DIPOLE INTERACTIONS BETWEEN COLD RYDBERG ATOMS USING MICROWAVE SPECTROSCOPY

by

Kourosh Afrousheh

A thesis
presented to the University of Waterloo
in fulfillment of the
thesis requirement for the degree of
Doctor of Philosophy
in
Physics

Waterloo, Ontario, Canada 2006

©Kourosh Afrousheh, 2006

I hereby declare that I am the sole author of this thesis. This is a true copy of the thesis, including any required final revisions, as accepted by my examiners.

I understand that my thesis may be made electronically available to the public.

Abstract

This thesis reports the first observation of the resonant electric dipole-dipole interaction between cold Rydberg atoms using microwave spectroscopy, the observation of the magnetic field suppression of resonant interactions, and the development of a unique technique for precise magnetic field measurements.

A Rydberg state ($46d_{5/2}$) of laser cooled ^{85}Rb atoms has been optically excited. A fraction of these atoms has been transferred to another Rydberg state ($47p_{3/2}$ or $45f_{5/2,7/2}$) to introduce resonant electric dipole-dipole interactions. The line broadening of the two-photon $46d_{5/2} - 47d_{5/2}$ microwave transition due to the interaction of $46d_{5/2}$ with $47p_{3/2}$ or $45f_{5/2,7/2}$ atoms has been used as a probe of the interatomic interactions. This experiment has been repeated with a DC magnetic field applied. The application of a weak magnetic field ($\leq 0.6\,\mathrm{G}$) has reduced the line broadening due to the resonant electric dipole-dipole interaction, indicating that the interactions are suppressed by the field. Theoretical models have been developed that predict the energy shifts due to the resonant electric dipole-dipole interaction, and the suppression of interactions by magnetic fields. A novel technique for sensitive measurement of magnetic fields using the $34s_{1/2} - 34p_{1/2}$ one-photon microwave transition has also been presented. Using this technique, it has been possible to calibrate magnetic fields in the magneto-optical trap (MOT) apparatus to less than 10mG, and put an upper bound of 17mG on any remaining field inhomogeneity.

Acknowledgements

I would like to thank my supervisor James D. D. Martin for his help, support and enthusiasm throughout this work. He spent much of his time in the laboratory, and was always available to help his students with his technical and scientific advice. I worked closely with him in most parts of this thesis, and wish to thank him for his time.

The members of my Ph.D. advisory committee, professors Walt W. Duley, Donna T. Strickland, Peter Bernath, Joseph Sanderson, and Robert L. Brooks, deserve many thanks for their time, and for their constructive comments. Also, I wish to thank my thesis defence committee especially Prof. Francis Robicheaux for coming from Alabama for my defence, and Prof. Robert Le Roy for carefully reading my thesis and providing helpful comments.

Special thanks to my colleagues who helped me in different parts of this research, Parisa Bohlouli-Zanjani, Maria Fedorov, Ashley Mugford, Jeffery Carter, Owen Cherry, Dhruv Vagale, Poya Haghnegahdar, and Joseph Petrus. I would also like to thank Andy Colclough, the student machine shop supervisor, and Yacek Szubra, the electronic shop supervisor, who are always there to help students with their technical advice.

Many thanks to employees in the Physics Department, University of Waterloo, especially our very nice graduate coordinator Judy McDonnell and GWPI administrator Margaret O'Neill.

I wish to dedicate my warmest thanks and appreciation to my parents who have supported me in all stages of my life, and who have always encouraged me to work hard and have been the reason for any progress that I have made so far. Thank you for making me feel your pure love which is the most precious thing in my life. My deepest thanks to my brothers and sisters: Abolfazl, Sara, Dariush, Zahra, and Mehdi, for being the best siblings I could ever have; for being my best friends, and for their constant love and support over the years. Many thanks to all my friends in Kitchener-Waterloo region with whom I have lots of memorable time, especially Mohammad Kohandel who helped me find my way when I first came to Canada.

I reserved the last line to thank my lovely wife Samaneh who came to my life in the last two years of my Ph.D., and has since been my companion in happiness and hardship. Her love and her warm temper was the most valuable thing that I experienced during the last two years of finishing and writing this thesis. Thanks my dear for putting up with lots of late nights, and for being always supportive.

To my mother and father
(Mehrangiz & Emamgholi)

Contents

List of Tables

List of Figures

Chapter 1

Introduction

1.1 Rydberg Atoms

Rydberg atoms are atoms that are excited to states of high principal quantum number n. An example of excitation to Rydberg states of sodium is given in Fig. 1-1 [1]. Rydberg atoms have a number of peculiar properties including an exaggerated response to electric fields, long radiative decay times, large transition dipole moments, and electron wavefunctions that under some conditions approximate classical orbits of electrons about the nuclei.

In Rydberg atoms the valence electrons, in high n, have binding energies that decrease as $1/n^2$, orbital radii that increase as n^2, and geometric cross-sections that scale as n^4 [1]. Therefore, Rydberg atoms are extremely large and are easily perturbed or ionized by collisions or external fields. For instance, the orbital radius of $n = 100$ of Rb is roughly $0.5\,\mu$m, and it has a binding energy ($\sim 0.047\,$eV) comparable to thermal energies at $300\,$K. The n^2 scaling of the size of Rydberg atoms for $24 \leq n \leq 56$ was confirmed in a clever experiment by Fabre *et al.* in 1983 [2]. In general, different properties of Rydberg atoms scale with some power of n, and can be exaggerated. Because of these unusual properties, Rydberg atoms have been of interest in physics and chemistry for a long time. The lack of an efficient method of producing single-state Rydberg atoms had made it difficult, however, to study these atoms systematically. Electron impact excitation and charge exchange excitations were the only available schemes of producing Rydberg atoms that were used by scientists in the 1950s and 1960s. These methods, however, resulted in the spread of Rydberg population over many states. In the 1970s, with

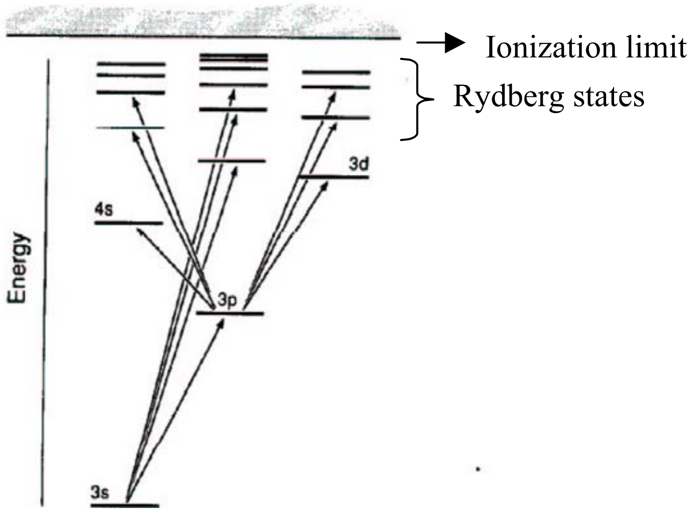

Figure 1-1: Excitation to Rydberg states in sodium atom (from Ref. [1]).

the advent of tunable dye lasers, it became possible to produce samples of single-state Rydberg atoms (atoms excited to the same energy level). Since then, the interest in Rydberg atoms has increased constantly owing to the development of techniques to create and study Rydberg atoms. Laser cooling and trapping is one example of these techniques that has opened new areas of research related to Rydberg atoms such as ultracold plasmas [3,4], quantum computing with cold neutral atoms (see for example [5] and [13]), and Rydberg atom-surface interaction in atom-chip experiments.

One of the interesting properties of Rydberg atoms that has been the subject of investigations for a long time is their particular sensitivity to external fields. Over the years, studies of atom-field interactions have provided important keys to understanding atomic structure, spin-dependent interactions, and angular momentum coupling schemes in atoms. The effects of external perturbations (such as electric and magnetic fields) on ground state atoms are usually small compared to intra-atomic interactions. However, in highly excited atoms, these two types of interaction can be comparable, especially for large fields. This is because the excited electron is so far away from the nucleus that its Coulombic interaction with the nucleus is diminished, and it can be perturbed easily by moderate fields. Rydberg atoms strongly resemble the hydrogen atom in many aspects, and are readily accessible, for instance, for detailed studies of the influence of external magnetic and electric fields on the level structure. Because of the sensitivity of Rydberg atoms to external fields, they are sometimes used as sensitive tools for probing small electric and magnetic fields [6,7].

1.2 Dipole-dipole interaction between Rydberg atoms

Due to the large separation of the valence electron from the ion-core in highly excited Rydberg atoms, these atoms have large electric transition dipole moments compared to ground state atoms [1]. The strength of the dipole-dipole interaction between two atoms is dictated by the size of their dipole transition moments. This means that the dipole-dipole interaction, which is negligible for ground state atoms, can be turned on by excitation to Rydberg states. Several groups around the world have designed experiments to study different aspects of dipole-dipole interactions between highly excited atoms. These experiments were initially focussed on interactions between Rydberg atoms produced in atomic beam experiments [1,2,4]. With the arrival of magneto-optical trap (MOT), this focus changed to the study of interactions between cold Rydberg atoms [9-16].

In 1981 Raimond *et al.* [8] observed for the first time the spectral line broadening due to van der Waals interactions (nonresonant dipole-dipole interactions) between Rydberg atoms. They showed that for high density samples of Rydberg atoms, when the average interatomic separation is just a few times larger than the Rydberg atom radius, the direct van der Waals interactions between Rydberg atoms become comparable to the binding energy of the Rydberg electron. There have also been experiments on the observation of nonresonant dipole-dipole interactions (van der Waals) between cold Rydberg atoms [14,15]. In these experiments, it has been shown that excitation to Rydberg states in a cold cloud of atoms in a MOT saturates due to the van der Waals interaction between Rydberg atoms.

In some cases Rydberg atoms do not interact in zero field conditions, but start to resonantly interact when a specific electric field is applied. Here, the applied electric field shifts the Rydberg energy levels due to the Stark effect, and makes them interact through resonant energy transfer. Resonant energy transfer between Rydberg atoms was first studied in atomic beam experiments (see chapter 14 of Ref. [1]), and then between cold Rydberg atoms in a MOT [9-13].

Recently, dipole-dipole interactions between cold Rydberg atoms have received attention in the context of quantum information processing using cold neutral atoms [5] and [13]. *Dipole blockade* is one of the proposals that utilizes dipole-dipole interaction between cold Rydberg atoms to store qubits in clouds of cold atoms without the need for individual addressing of atoms [13]. In dipole blockade a single atom excited to a Rydberg state blocks further resonant excitation of atoms to same Rydberg state due to the dipole-dipole interaction. However, this has not yet been experimentally observed.

1.3 Structure of thesis

In this thesis, the resonant electric dipole-dipole interaction between cold Rydberg atoms is studied. For the first time, microwave spectroscopy is used to probe the influence of resonant electric dipole-dipole interactions on radiative transitions between nearby Rydberg states. Also, the effect of applied DC magnetic fields on the strength of resonant dipole-dipole interactions is investigated. Cold Rydberg atoms are produced by laser excitation of laser cooled and trapped atoms in a MOT. Microwave radiation is then used to transfer Rydberg atoms to different states and to probe interatomic interactions. For the observation of the resonant dipole-dipole interaction and its suppression due to applied magnetic fields presented in this thesis, $46d_{5/2}$ is excited. Then, using microwave radiation, a fraction of these atoms may be transferred to other nearby Rydberg states, such as $46p_{3/2}$, $47p_{3/2}$, or $45f_{5/2,7/2}$, to study resonant dipole-dipole interactions. The linewidth broadening of the two-photon $46d_{5/2} - 57p_{3/2}$ microwave transition is used to probe the interactions between Rydberg atoms. These experiments are repeated when a DC magnetic field is deliberately applied to investigate its effect on linewidth broadening due to resonant dipole-dipole interactions.

In chapter 2 of this thesis, a summary of the background theory for this work is presented, together with some experimental techniques that were used in these experiments. Then, in chapter 3, the use of microwave transitions between Rydberg states for measuring stray electric and magnetic fields is explained. The results of the observation of the resonant electric dipole-dipole interaction between cold Rydberg atoms, and its suppression by an applied magnetic field are presented in chapter 4. Theoretical models that explain the agreement of the experimental results with theory are presented in chapter 5. Chapter 6 includes a summary and discussion of the results along with proposed future work. The method for determining the density of the interacting Rydberg atoms is presented in Appendix A.

Bibliography

[1] T. F. Gallagher, “*Rydberg Atoms*”, Cambridge University Press 1994.

[2] C. Fabre, M. Gross, J. M. Raimond, and S. Haroche, “*Measuring atomic dimensions by transmission of Rydberg atoms through micrometre size slits*”, J. Phys. B: At. Mol. Phys. 16, L671 (1983).

[3] T. C. Killian, S. Kulin, S. D. Bergeson, L. A. Orozco, C. Orzel, and S. L. Rolston, “*Creation of an ultracold neutral plasma*”, Phys. Rev. Lett., 83, 4776 (1999).

[4] M. P. Robinson, B. L. Tolra, M. W. Noel, T. F. Gallagher, and P. Pillet, “*Spontaneous evolution of Rydberg atoms into an ultracold plasma*”, Phys. Rev. Lett. 85, 4466 (2000).

[5] D. Jaksch, J. I. Cirac, P. Zoller, S. L. Rolston, R. Côté, and M. D. Lukin,“*Fast quantum gates for neutral atoms*”, Phys. Rev. Lett. 85, 2208 (2000).

[6] M. T. Frey, X. Ling, B. G. Lindsay, K. A. Smith, and F. B. Dunning, “*Use of the Stark effect to minimize residual electric fields in an experimental volume*”, Rev. Sci. Instrum. 64, 3649 (1993).

[7] A. Osterwalder and F. Merkt, “*Using high Rydberg states as electric field sensors*”, Phys. Rev. Lett., 82, 1831 (1999).

[8] J. M. Raimond, G. Vitrant, and S. Haroche, “*Spectral line broadening due to the interaction between very excited atoms: the dense Rydberg gas*”, J. Phys. B 14, L655 (1981).

[9] W. R. Anderson, J. R. Veale, and T. F. Gallagher, “*Resonant dipole-dipole energy transfer in a nearly frozen Rydberg gas*”, Phys. Rev. Lett. 80, 249 (1998).

[10] I. Mourachko, D. Comparat, F. de Tomasi, A. Fioretti, P. Nosbaum, V. M. Akulin, and P. Pillet, "*Many-body effects in a frozen Rydberg gas*", Phys. Rev. Lett. 80, 253 (1998).

[11] W. R. Anderson, M. P. Robinson, J. D. D. Martin, and T. F. Gallagher, "*Dephasing of resonant energy transfer in a cold Rydberg gas*", Phys. Rev. A 65, 063404 (2002).

[12] I. Mourachko, W. Li, and T. F. Gallagher, "*Controlled many-body interactions in a frozen Rydberg gas*", Phys. Rev. A 70, 031401 (2004).

[13] M. D. Lukin, M. Fleischhauer, and R. Cote, "*Dipole Blockade and quantum information processing in mesoscopic atomic ensembles*", Phys. Rev. Lett. 87, 037901 (2001).

[14] D. Tong, S. M. Farooqi, J. Stanojevic, S. Krishnan, Y. P. Zhanq, R. Cote, E. E. Eyler, and P. L. Gould, "*Local blockade of Rydberg excitation in an ultracold gas*", Phys. Rev. Lett. 93, 063001 (2004).

[15] K. Singer, M. Reetz-Lamour, T. Amthor, L. G. Marcassa, and M. Weidemuller, "*Suppression of excitation and spectral broadening induced by interactions in a cold gas of Rydberg atoms*", Phys. Rev. Lett. 93, 163001 (2004).

[16] K. Afrousheh, P. Bohlouli-Zanjani, D. Vagale, A. Mugford, M. Fedorov, J. D. D. Martin, "*Spectroscopic observation of resonant electric dipole-dipole interaction between cold Rydberg atoms*", Phys. Rev. Lett. 93, 233001 (2004).

Chapter 2

Theoretical Background and Experimental Techniques

2.1 Introduction

As explained in the previous chapter, resonant electric dipole-dipole interactions between cold Rydberg atoms with and without the presence of a DC magnetic field are studied experimentally in this thesis. To help the discussions in the following chapters, a summary of the basic theory related to these experiments is presented in this chapter, as well as some of the experimental techniques that were used. Details of the theory of Rydberg atoms, their properties, and their interactions with external fields have been discussed in many papers and books (see for example [1,2]). This chapter starts with a description of the operation of the magneto-optical trap used for production of cold atoms. Rydberg atoms are produced by exciting the cold atoms; this excitation scheme is also presented. Since studies of Rydberg atoms in the presence of external fields is a major part of this work, the effects of external fields (electric and magnetic fields) on Rydberg atoms are explained in greater detail. In the last section, the selective field ionization technique for Rydberg state detection is discussed.

2.2 Laser cooling and trapping of atoms

To study the interactions between cold Rydberg atoms, laser cooled and trapped atoms were excited to high energy levels. A standard vapour-cell rubidium magneto-optical trap (MOT) was used to make a cold cloud of atoms. In this section, I present a brief description of the operation of a MOT. Detailed studies of laser cooling and trapping can be found in literature, such as Ref. [3].

The magneto-optical trap has been the most commonly used apparatus for producing cold samples of neutral atoms since its invention in 1987 [4]. In the MOT a certain type of atom in the gas phase are exposed to a combination of electromagnetic radiation and an inhomogeneous magnetic field. By tuning the radiation field to an appropriate frequency, one can force the atoms to scatter photons from the radiation field that opposes their motion. The absorption and emission of photons on average results in a reduction of atomic velocities. An inhomogeneous magnetic field helps trap the atoms once they are cold. A schematic picture of a MOT is shown in Fig. 2-1. Atoms, which are captured from a vapour in a vacuum cell, are initially at room temperature and move randomly in all directions. To achieve cooling and trapping in three dimensions, three pairs of counter-propagating laser beams and an inhomogeneous magnetic field produced by a pair of anti-Helmholtz coils (AHCs) are used (see Fig. 2-1). To account for the Doppler effect caused by the atomic motion, the laser beams are detuned to the red of a specific atomic transition. In this case, atoms scatter more photons from the laser beam that opposes their motion. Also, the laser beams are circularly polarized such that counterpropagating beams have opposite helicity. The combination of an inhomogeneous magnetic field and circularly polarized laser beams ensures that atoms experience a space dependent force. This way, atoms experience a friction force (needed for cooling) that attempts to bring the atoms to rest, and a harmonic force (required for trapping) that bounds the atoms to the trap centre [3]:

$$\overrightarrow{F} = -\beta \overrightarrow{v} - k \overrightarrow{r}. \tag{2.1}$$

The primary force that atoms feel is a radiation pressure force or recoil each time they scatter a photon and receive its momentum. The momentum kick that the atom receives from each scattered photon is quite small; however, by exciting a strong atomic transition, it is possible

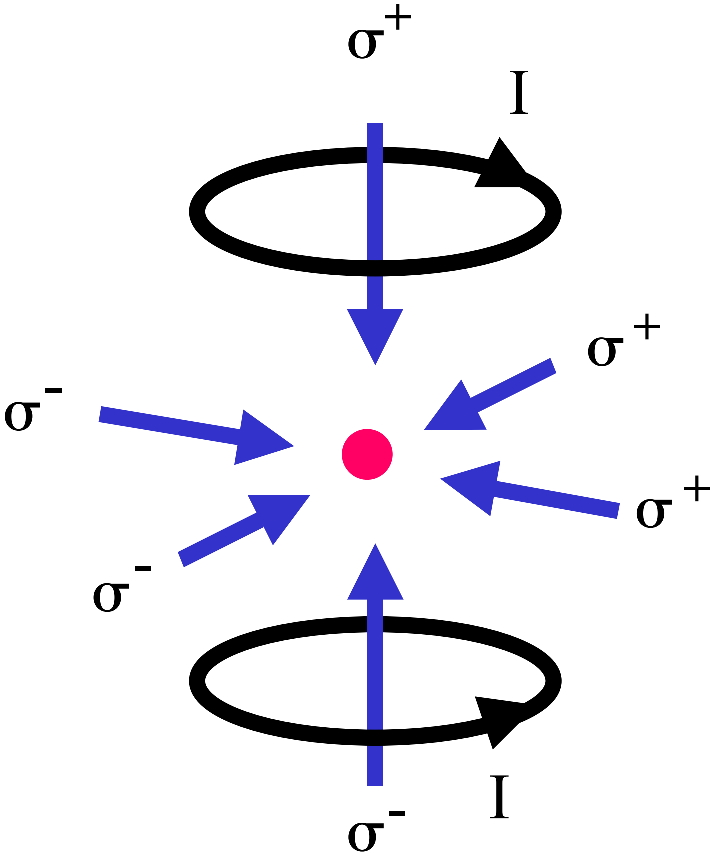

Figure 2-1: Schematic of the magneto-optical trap: the cloud of cold atoms is located at the intersection of three pairs of counterpropagating laser beams. In the ideal situation, where the laser beams are aligned properly and stray magnetic fields are nulled out, this is at the center of a pair of anti-Helmholtz coils.

to scatter more than 10^7 photons per atom per second and produce large deceleration [3]. For ^{85}Rb, the $5s_{1/2}(F=3) \rightarrow 5p_{3/2}(F=4)$ transition at 780 nm is an appropriate transition for laser cooling and trapping. A repump laser is used to drive the $5s_{1/2}(F=2) \rightarrow 5p_{3/2}(F=3)$ transition to make sure that atoms do not fall into the dark $F=2$ hyperfine sublevel of the ground state. The energy levels of ^{85}Rb for the ground state ($5s_{1/2}$), the first excited state ($5p_{3/2}$), and the transitions used for cooling and trapping in a MOT are shown in Fig. 2-2. Both cooling and trapping and repump lasers are locked to atomic transitions in ^{85}Rb using the dichroic atomic-vapor laser lock (DAVLL) technique [5]. Saturated absorption spectroscopy [6] was used to identify the cooling and trapping and repump atomic transitions for the purpose of laser frequency locking. These techniques are explained in Ref. [7].

Initially, for cooling and trapping and repump transitions, home-made external cavity diode lasers were used. The output beam of each laser (with a power of roughly 20 mW measured after a Faraday isolator used for laser protection) was split into two beams. One beam went to the setup for saturation absorption spectroscopy used for laser frequency stabilization [7], and carried roughly 3 mW power. The other beam of the cooling and trapping laser was focused down into an acousto-optical modulator (AOM) (IntraAction, Model ME-801ENG Modulator Driver) for possible fast switching off the MOT. The first-order diffracted output of the AOM was then split into six beams which were sent into the MOT setup in a configuration shown in Fig. 2-1. The remaining of the repump laser was split into two beams which were made collinear with a pair of counterpropagating cooling and trapping beams. In order to shape the MOT lasers, and also reduce the sensitivity of the MOT to any changes in the alignment of the lasers, it was decided to couple the lasers into single mode fibers. A higher power commercial external cavity, grating stabilized diode laser (Toptica DLX 110, output power: 380 mW) operating at 780 nm was used to compensate for the power loss in fiber coupling. Also, to enhance the repump power, this laser was used to injection lock a temperature stabilized, commercial, 780 nm diode laser (Thorlabs, DL7140-201S). The output power of the slave laser was 35 mW. The maximum coupling efficiency that was obtained for single mode fibers was roughly 50%.

A picture of the MOT setup that was used in this thesis is shown in Fig. 2-3. The larger coils on this figure are the compensating coils used to null out stray magnetic fields so that the zero of the inhomogeneous magnetic field lies at the center of the AHCs. Details of the stray

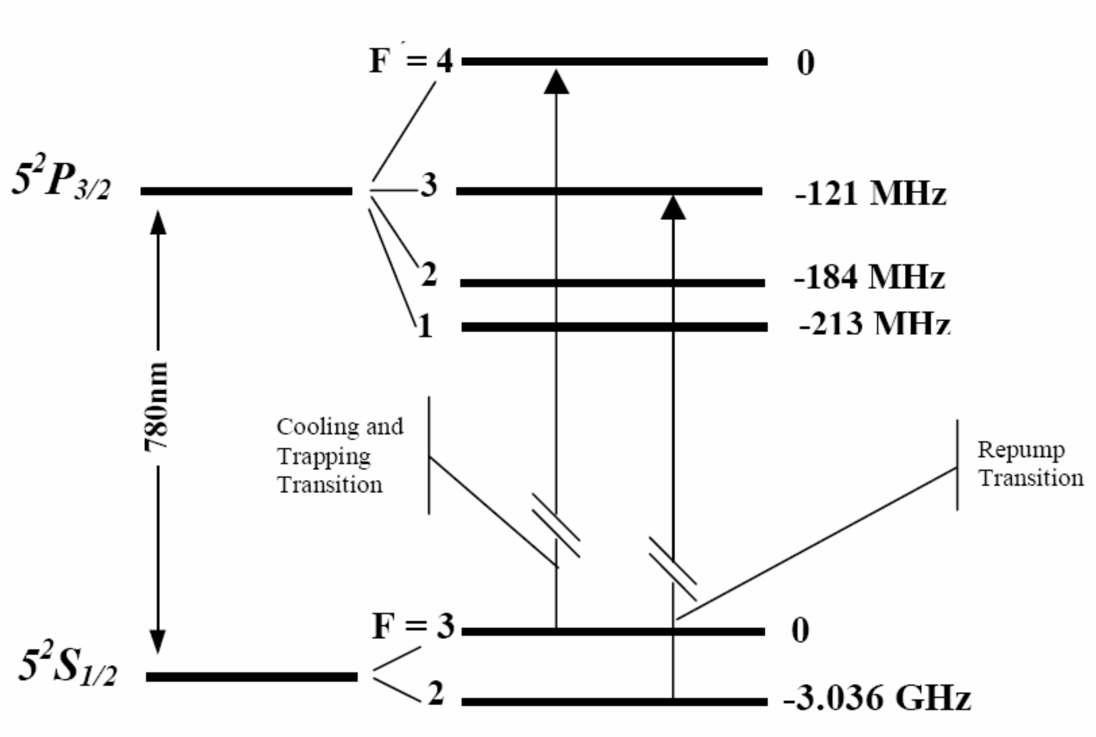

Figure 2-2: The ground state ($5s_{1/2}$) and the first excited state ($5p_{3/2}$) of ^{85}Rb, and the transitions used for cooling and trapping in a MOT [7].

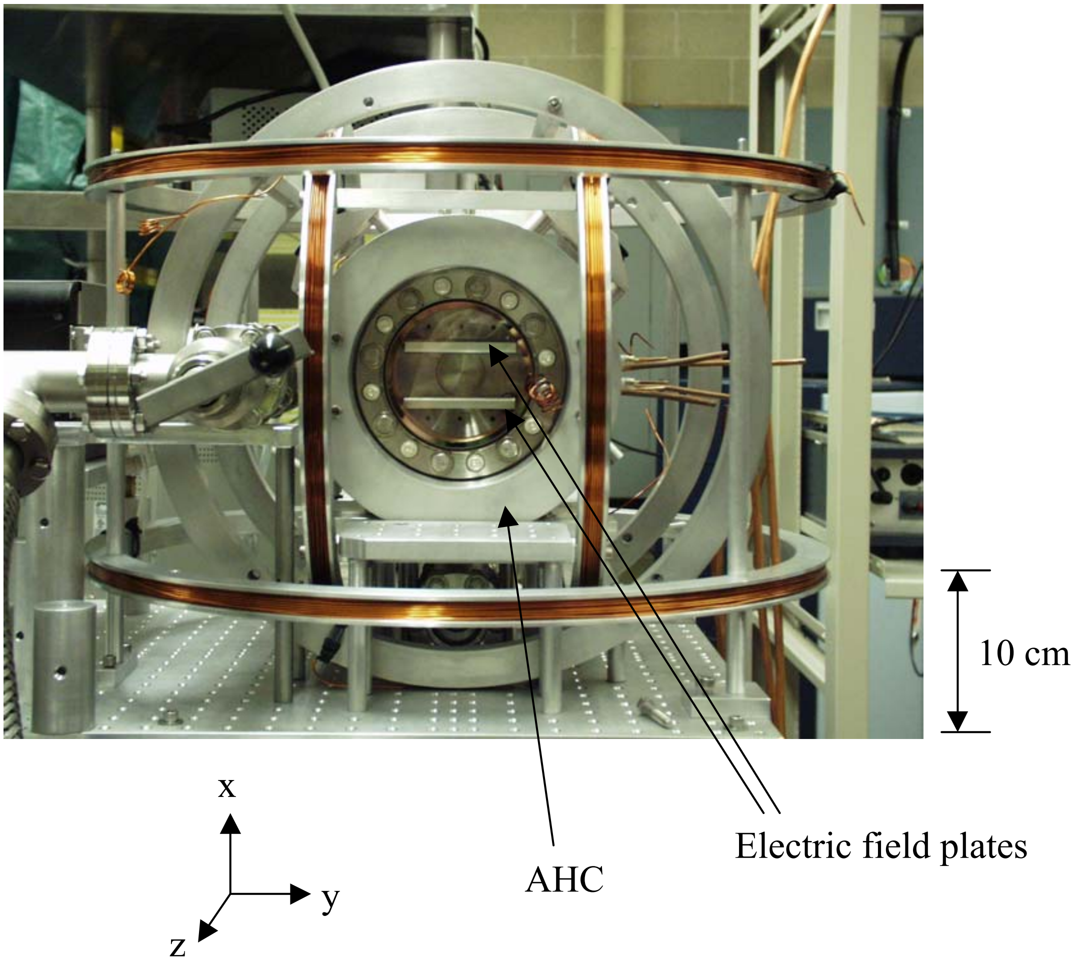

Figure 2-3: The magneto-optical trap setup used to produce cold Rb atoms. This picture was taken before optics and microwave components were set up.

field compensation and its importance are explained in chapter 3.

2.3 Production of Rydberg Atoms

Rydberg atoms may be produced in different processes such as electron impact, photoexcitation, charge exchange, and collisional and optical excitation [1]. Electron impact, charge exchange, and photoexcitation were common in last few decades ending in 1980, and laser excitation has been the dominant method used to produce Rydberg atoms in the past three decades.

In electron impact excitation of Rydberg states of atoms, a pulsed beam of electrons passes through the sample of target atoms and excites them to Rydberg states by collisions [8,9] ($A + e^- \rightarrow A(nl) + e^-$). Similarly, charge exchange or electron transfer collision [10] can be formulated as $A^+ + B \rightarrow A(nl) + B^+$. In both processes $A(nl)$ is the produced Rydberg atom in a state with principal quantum number n and orbital quantum number l. Based on kinetic energies of particles before and after collision, and their angular distribution at impact, excited atoms with different energy levels (with different principal quantum number n) may be produced. Also, the atoms initially excited to low l states, are redistributed over states with high l by subsequent collisions. Therefore, in general, these two methods distribute atoms over different energy states, and are not useful for selectively producing single state Rydberg atoms.

2.3.1 Optical excitation

Photoabsorption has been extensively used for a long time to produce and study Rydberg atoms. In this process, an atom or a molecule is excited to a Rydberg state by absorbing a photon from a light source:

$$A + h\nu \rightarrow A(nl). \tag{2.2}$$

In early experiments, Rydberg states of atoms and molecules were produced by absorbing photons from a source of light that emitted the appropriate wavelength [11-13]. The efficiency of excitation with a diffuse light source is poor, since the flux of emitted photons is small. This problem was solved by invention of dye lasers. A high photon flux may be achieved from lasers, unlike normal sources of light. Lasers can also be focussed into the cloud of atoms to produce high density samples of Rydberg atoms. This density may be varied systematically, where it is desirable, by changing the laser beam spot size or its power.

In the experiments of this thesis, excitation to Rydberg states of ^{85}Rb is a two-photon process for which two different sources of light are required. A 780 nm laser excites $5s_{1/2}$ ground state atoms to $5p_{3/2}$, which may then be excited to different Rydberg states by a tunable wavelength laser. In a Rb MOT, $5p_{3/2}$ atoms are continuously produced by the cooling and trapping laser, and with a tunable 480 nm laser, it is possible to selectively excite different Rydberg states from $5p_{3/2}$. Figure (2-4) shows the excitation of the ground state rubidium atoms to Rydberg states in a MOT.

2.4 Rydberg atoms in external fields

One of the interesting properties of Rydberg atoms that has been the subject of investigations for a long time is their particular sensitivity to external fields. In highly excited atoms, the excited electron is far away from the nucleus so that its Coulombic interaction with the nucleus is diminished, and it can be perturbed easily by moderate fields. Therefore, Rydberg atoms are readily accessible for detailed studies of the influence of external electric fields on the level structure. Also, because of the sensitivity of Rydberg atoms to external fields, they are sometimes used as sensitive tools for probing small electric fields. A brief explanation of the behaviour of Rydberg atoms in electric and magnetic fields is presented in this section.

2.4.1 Rydberg atoms in electric fields

Electric fields shift the atomic energy levels and split them into several spectral lines due to the Stark effect. The effect arises because of the interaction between the electric dipole moment of an atom with an external electric field. If the electric field is uniform over the length scale of the atom, then the perturbing Hamiltonian is of the form

$$\hat{H} = -\overrightarrow{\mu}.\overrightarrow{\varepsilon} = e\varepsilon_z z, \tag{2.3}$$

where $\overrightarrow{\mu}$ is the electric dipole moment and $\overrightarrow{\varepsilon}$ is the electric field. The first order energy shift of the state $|\Psi_m\rangle$ due to the perturbation is given by $\Delta E_m = e\varepsilon_z \langle \Psi_m |z| \Psi_m \rangle$. Since the unperturbed states may be degenerate, we normally need to use the eigenvectors of $\hat{H}$ when calculating the energy shifts. Fundamentally, the electric field changes the boundary conditions for the electron from closed to open, converting the bound states into continuum states. This effect starts to be important at a characteristic field which is given by $\varepsilon_c = 1/\left(16n^4\right)$ [1]. For $n = 15$, the value of ε_c is about $6\,\mathrm{kV}\,/\,\mathrm{cm}$.

To explain the detail of the Stark effect, the following simplified Hamiltonian (which neglects the relativistic and radiative interactions) is used [14]

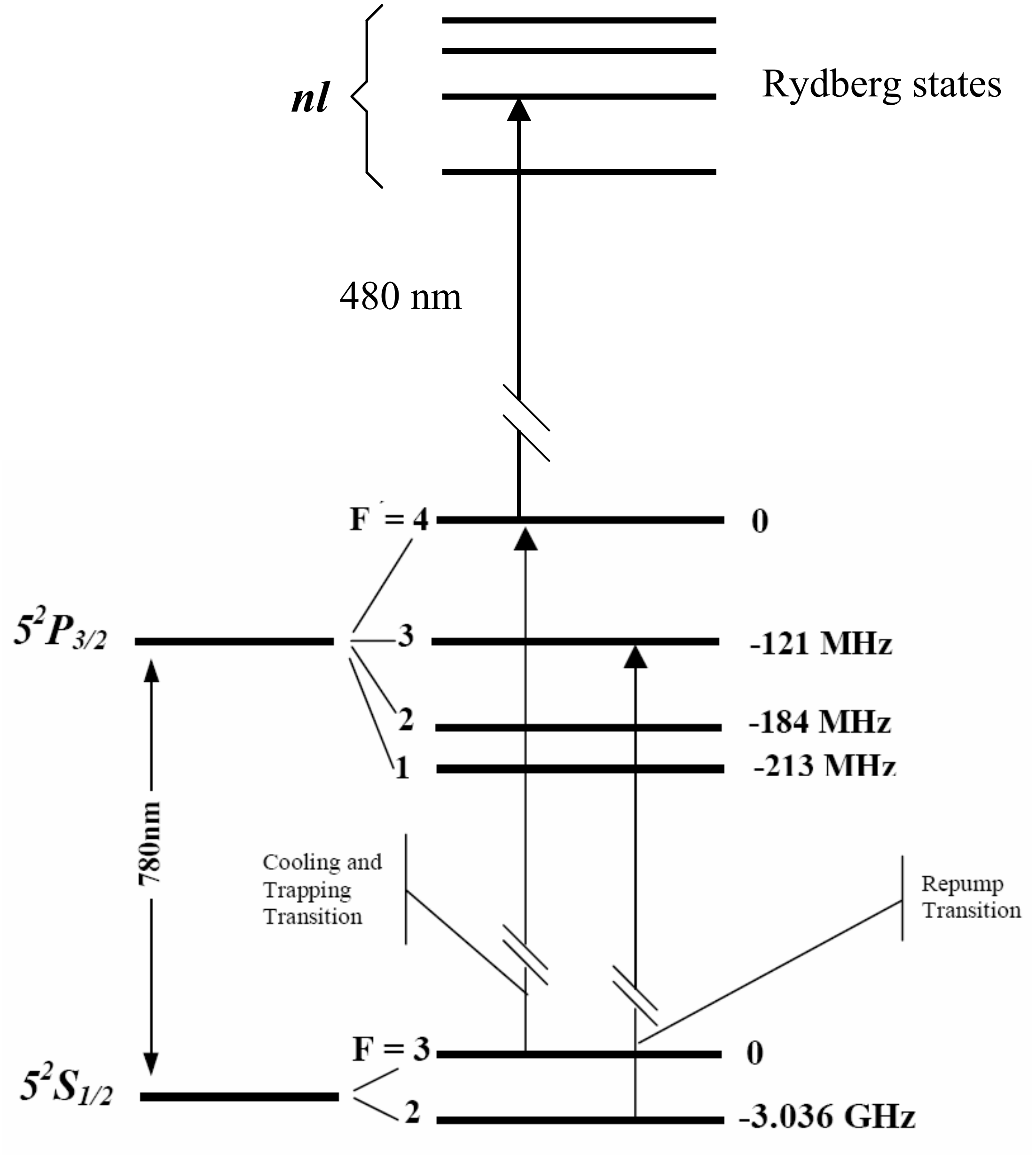

Figure 2-4: Excitation to Rydberg states of Rb using a two-colour two-photon process.

$$H = -\frac{1}{2}\nabla^2 + V(r) + \varepsilon z, \tag{2.4}$$

where the potential seen by the electron, when $V(r)$ is a central potential and electric field directed along the z axis, is given by $\acute{V}(r) = -\frac{1}{r} + \varepsilon z$. For hydrogen atom, the Schrodinger equation for an electron orbiting a singly charged ion with the Hamiltonian given by Eq. 2.4 is separable in parabolic coordinates, and it is possible to obtain exact expressions for the Stark effect of hydrogenic energy levels (see for example [15,16]).

An energy level diagram for $n = 8$ to $n = 14$ of the hydrogen atom is shown on Fig. 2-5. The levels exhibit linear Stark shift from zero field to the point at which field ionization occurs, which is shown by broken lines in Fig. 2-5. So, the first order energies are adequate for many purposes. We also see, in this diagram, that the red, or downshifted, Stark states ionize at lower fields compared to the blue, or upshifted, states. The classical threshold field for ionization of different Stark states, which is obtained from $E_c = -2\sqrt{\varepsilon}$ [1], is shown by a heavy line. As seen on this diagram, the Stark levels of the adjacent n cross in hydrogen atom, which is because of the lack of coupling between these states.

The behaviour of nonhydrogenic atoms in an electric field is not exactly the same as that of the hydrogen atom, and we cannot use the same approach for other atoms. The reason is that the Hamiltonian in Eq. 2.4 is not separable in parabolic coordinates for nonhydrogenic atoms. Therefore, in order to study the Stark effect in these atoms we should look for some approximation schemes.

In alkali atoms there is a core of closed-shell electrons and a single valence or outer electron. If we excite this electron to a high enough level, it will spend most of its time at large distances; hence, the potential experienced by this electron approaches $-1/r$. Ignoring the spin of the Rydberg electron, the Hamiltonian is given by

$$H = -\frac{1}{2}\nabla^2 + \frac{1}{r} + V_d(r) + \varepsilon z, \tag{2.5}$$

where $V_d(r)$ is the difference between the potential of the Rydberg atom in zero field and the Coulomb potential $-1/r$. Using this Hamiltonian, the energies of the alkali atoms in zero field are given by

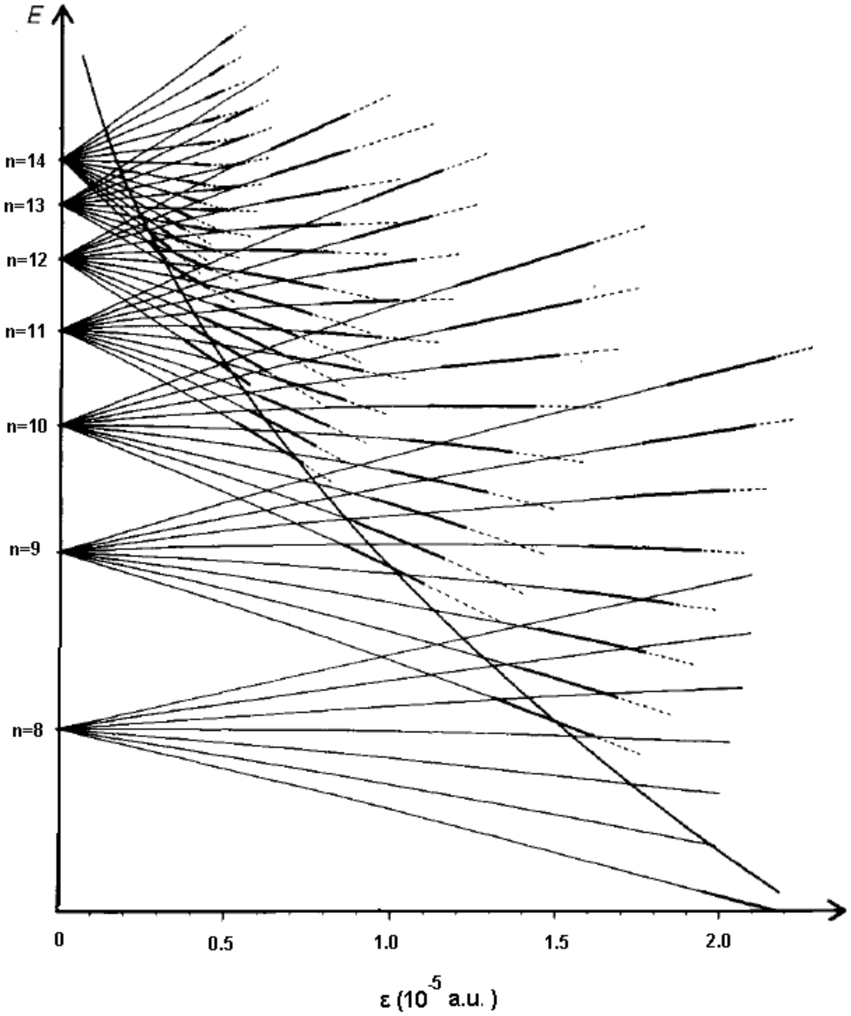

Figure 2-5: Energy level diagram for $n = 8$ to $n = 14$ of the hydrogen atom as a function of electric field [1]. The ionization threshold field for different Stark states is also shown by a heavy line. The electric field is in atomic units; 1 a.u. $\simeq 5.14 \times 10^9$ V/cm (from Ref. [1]).

$$E_{nl} = -\frac{1}{2(n-\delta_l)^2}, \tag{2.6}$$

where δ_l is a constant for a given l and is called the quantum defect. Quantum defects are large when l is less than the maximum angular momentum of a core electron and are small otherwise. The energies in Eq. 2.6 are actually the diagonal elements of the Hamiltonian matrix. The energy levels for the $|m| = 1$ sublevels of $n = 15$ of Na, which were obtained by diagonalization of the Hamiltonian matrix, are shown in Fig. 2-6. The energy levels of different n do not cross as in the case of hydrogen atom- indeed, we see avoided crossing in this figure. Another evident point in this figure is that in zero field the s and p states are displaced from the high l states and they show large Stark shift at higher fields.

2.4.2 Rydberg atom interactions with magnetic fields

Magnetic fields shift the atomic energy levels due to the Zeeman effect. Compared with electrostatic interactions, the Zeeman effect is small for the magnetic fields that are normally produced in laboratories (magnetic fields up to 30 T). The complete Hamiltonian for an electron in a magnetic field is given by [14]

$$H = H_0 + H_p + H_d + H_s + H_{hf}, \tag{2.7}$$

in which H_0 is the Hamiltonian for the free atom, and H_p, the paramagnetic term, H_d, the diamagnetic term, H_s, the spin-orbit term, and H_{hf}, the hyperfine term, are written as

$$H_p = \frac{1}{2}\alpha(L + g_s S)\cdot B, \tag{2.8}$$

$$H_d = \frac{1}{8}\alpha^2 B^2 r^2 sin^2\theta, \tag{2.9}$$

$$H_s = \xi(r) L \cdot S, \tag{2.10}$$

$$H_{hf} = A(I\cdot J) + \frac{1}{2}\alpha g_I^{'} I \cdot B. \tag{2.11}$$

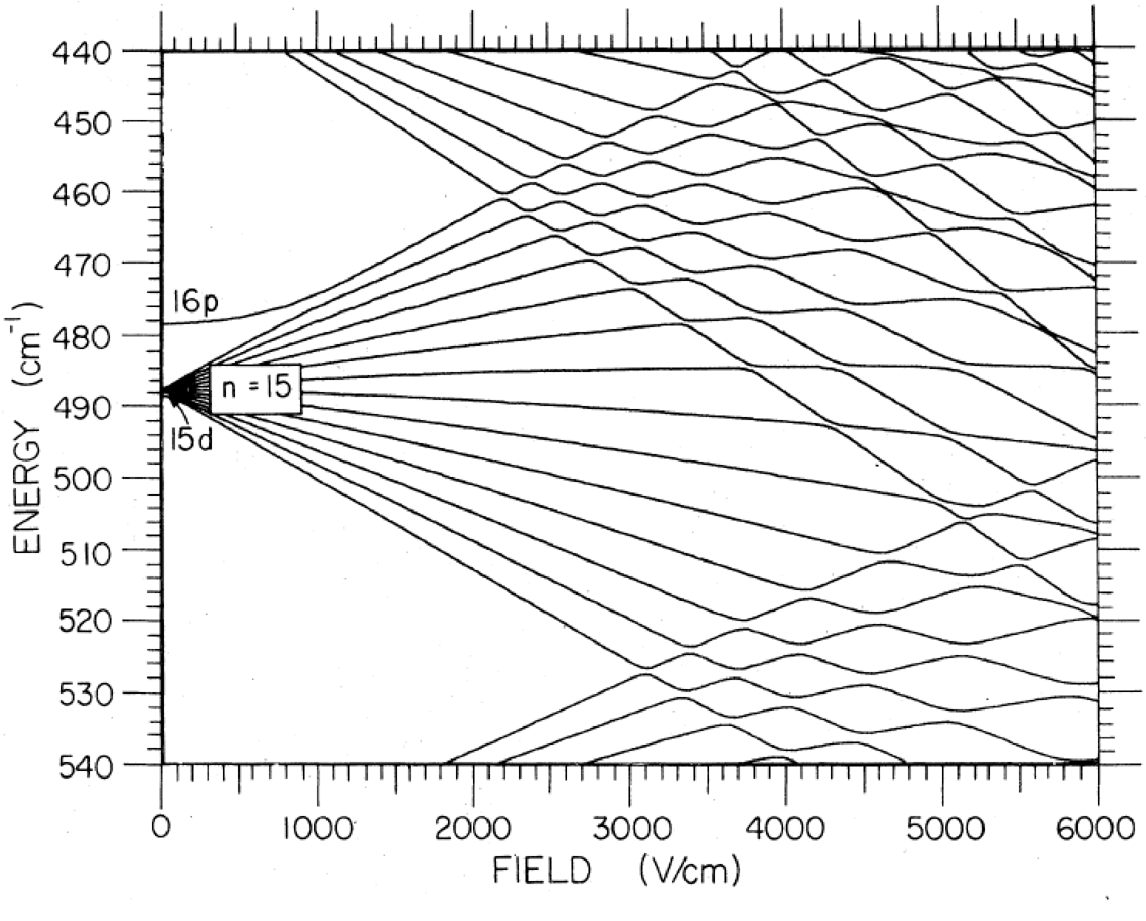

Figure 2-6: The Stark effect of energy levels for the $|m| = 1$ of $n = 15$ of Na (from Ref. [14]).

In these equations, r is the radial coordinate of the electron relative to the nucleus, α is the fine structure constant, g_s and g_I are the electronic spin and nuclear g factors, $\xi(r)$ is the radial spin-orbit operator, and A is the hyperfine constant. The operators L, S, J, and I are the electron orbital angular momentum, electron spin, total electronic angular momentum, and nuclear spin respectively. The Bohr magneton, which is the coupling constant for the paramagnetic effect, is small (in atomic units: $\mu_B = \alpha/2 \approx 4 \times 10^{-3}$); therefore, for small magnetic fields, the magnetic field interactions are small contributions to the Hamiltonian.

In theoretical studies of atom interactions with magnetic fields, different field strengths are usually considered. At low magnetic fields, the fine structure due to the L and S coupling, and the hyperfine structure due to J and I coupling are not altered appreciably. As the magnetic field is increased, the linear Zeeman effect due to the paramagnetic term in the Hamiltonian first becomes greater than the hyperfine splitting, and then exceeds the fine structure separations. For low magnetic fields, the diamagnetic term is small compared with the other terms in the Hamiltonian. The expectation value $\langle r^2 \rangle$ scales as n^4; therefore, the ratio of the diamagnetic to the paramagnetic term scales as $n^4 B$. If $n^4 B \ll 1$, the diamagnetic term in the Hamiltonian can be ignored. In this case, the shift in atomic energy levels is linear in magnetic field (linear Zeeman effect) and is given by $\mu_B m B$. Also, the magnetic effects are of the same order for high and low excited states of the same l, except for the fact that, due to the smaller sizes of the fine structure separations, the decoupling of L and S (Paschen-Back regime) is reached at lower magnetic fields for highly excited states.

The diamagnetic term becomes important in large magnetic fields, since it increases quadratically with field. This term, that scales as $n^4 B^2$, becomes especially important for highly excited Rydberg states at large fields, and it can even exceed the Coulombic interaction. However, the diamagnetic term is completely negligible at the fields used in this work.

Zeeman effect of the hyperfine structure

The Zeeman effect of the hyperfine structure comes from the interaction of the total electronic magnetic moment μ_J and the nuclear magnetic moment μ_I with the magnetic field. Because of the small size of the hyperfine interaction compared with the spin-orbit interaction, a field which is considered small for the fine structure can be large for the hyperfine structure. This is especially true for highly excited Rydberg atoms for which the hyperfine splittings are much smaller than that of ground state. As an example, the hyperfine splitting of $5s_{1/2}$ of Rb is $\sim$ 3GHz (see Fig. 2-2), and that of $34s_{1/2}$ is $\sim$ 500KHz (Ch. 3), and the Zeeman shift of an $F = 3$ hyperfine level at $B = 1$G is $\sim$ 1.4MHz. Since the microwave transitions between Rydberg states under different magnetic field conditions are studied in this thesis, it is reasonable to discuss the Zeeman effect of hyperfine structure separately.

We consider the IJ coupling and the interactions of the magnetic field with electron and nuclear magnetic moments as perturbations to all electrostatic and magnetic interactions internal to the electron system. This perturbation is given by [17]

$$\begin{aligned} H &= AI \cdot J + \mu_J \cdot B - \mu_I \cdot B \\ &= AI \cdot J + g_J \mu_B J_z B - g_I^{'} \mu_B I_z B. \end{aligned} \tag{2.12}$$

$g_I^{'}$ in this equation is defined as $g_I^{'} = \frac{\mu_I}{\mu_B I} = g_I \frac{\mu_N}{\mu_B}$, in which $\mu_N = \frac{e\hbar}{2M}$, and M is the mass of the proton. Therefore, $g_I^{'} = g_I \frac{m}{M} \approx \frac{1}{1836} g_I$, which is a very small number. Therefore, in defining the weak and strong field regions, we should only compare the first and second terms in Eq. 2.12. The condition $g_J \mu_B B \ll A$, defines the weak field region, $g_J \mu_B B \gg A$ the strong field, and between the two cases is the intermediate region. For $34s_{1/2}$ of ^{85}Rb, A/h is roughly 500 kHz in frequency units [17] (or $A/\mu_B \simeq 0.35\,\mathrm{G}$); hence, for weak fields $B \ll 0.35\,\mathrm{G}$, and for strong fields $B \gg 0.35\,\mathrm{G}$.

For a weak field, applying the Zeeman term $g_J \mu_B J_z B - g_I^{'} \mu_B I_z B$ as a perturbation using the $|IJFM_F\rangle$ representation, the first order energy shift is obtained as

$$\Delta E = g_F \mu_B B M_F, \tag{2.13}$$

where g_F is defined as [17]

$$g_F = g_J \frac{F(F+1) + J(J+1) - I(I+1)}{2F(F+1)} - g_I^{'} \frac{F(F+1) - J(J+1) + I(I+1)}{2F(F+1)}. \tag{2.14}$$

In the strong field case, $g_J\mu_B J_z B$ is the largest term in Eq. 2.12, and using the $|IJM_IM_J\rangle$ representation, the first-order energy shift is given by

$$\Delta E = g_J\mu_B BM_J - g_I^{'}\mu_B BM_I + AM_IM_J. \tag{2.15}$$

In the intermediate field region, the energy shift for $J = 1/2$ (and arbitrary I) is given by the Breit-Rabi formula [17]:

$$\Delta E = -\frac{h\Delta\upsilon}{2(2I+1)} - g_I^{'}\mu_B BM_F \pm \frac{1}{2}h\Delta\upsilon\left(1 + \frac{4M_F}{2I+1}x + x^2\right)^{1/2}, \tag{2.16}$$

where

$$x = \frac{(g_J + g_I^{'})\mu_B B}{h\Delta\upsilon}. \tag{2.17}$$

$h\Delta\upsilon$ is the separation of $F = I + 1/2$ and $F = I - 1/2$ at zero magnetic field (hyperfine separation at zero field). A graph of the Zeeman shifts of the hyperfine structure of $34s_{1/2}$ Rydberg state of Rb which was obtained using Eq. 2.16 is shown on Fig. 2-7.

2.5 Detection of Rydberg atoms

In Fig. 2-5, the broken lines show the ionization region, and the corresponding electric fields are the fields needed for ionizing different energy levels. The red or downshifted Stark states ionize at lower fields compared to the blue or upshifted states. We also see on this figure that the ionization region moves to lower electric fields as the principal quantum number n increases. This suggests that the application of a varying electric field may be a suitable technique for detecting Rydberg states. In this method, which is called the selective field ionization (SFI), the atoms are ionized in an increasing electric field, and the resulting electrons or ions are detected as a function of applied field (see for example Ref. [18]). SFI has become the most popular method of Rydberg atom detection in recent years, and is especially suitable for atoms in states with large principal quantum number that require a lower ionizing field [2]. Also, because atoms in different Rydberg states evolve differently in an increasing field, it is in principle possible to identify Rydberg atoms from the field dependence of their ionization signal. This became

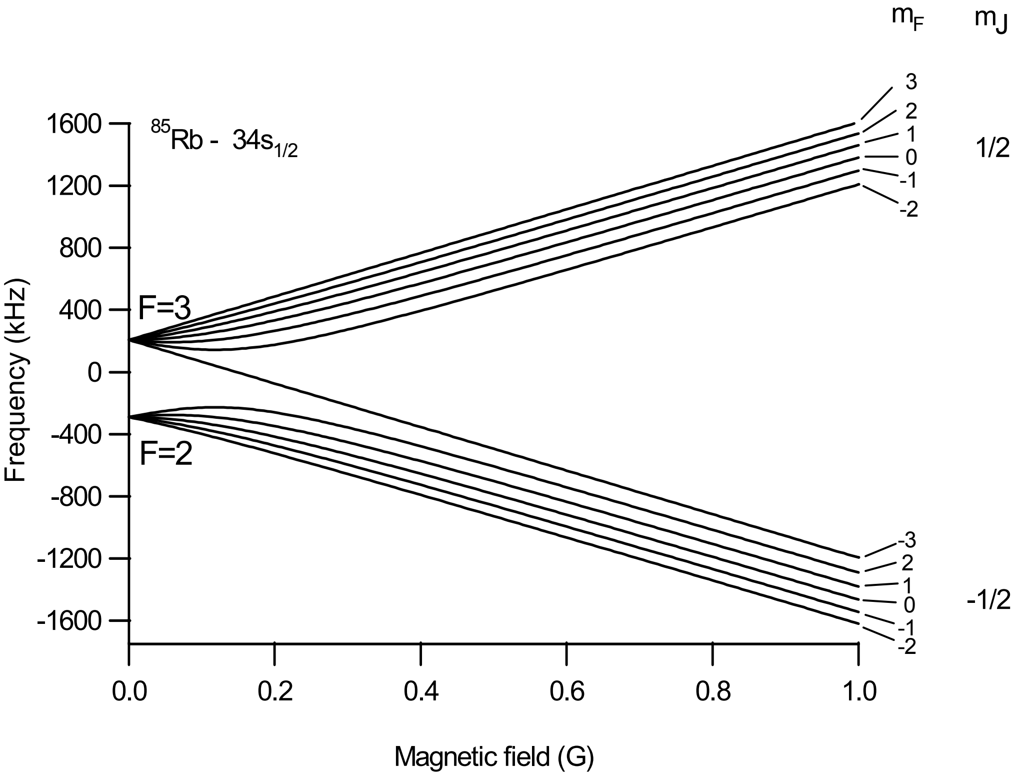

Figure 2-7: The Zeeman shifts of the hyperfine structure of the $34s_{1/2}$ state of Rb calculated using the Breit-Rabi formula, Eq. 2.16. The hyperfine splitting at zero magnetic field was obtained using $\nu_{hfs} = 14.6(\pm 1.4)\,\mathrm{GHz}(n^*)^{-5}$ [7], where n^* is the effective principal quantum number $n^* = n - \delta_s$, and $\delta_s = 3.1311804$ is the quantum defect of the $ns_{1/2}$ states [7].

more important with the arrival of tunable lasers that made the selective excitation of Rydberg states possible. When SFI is combined with multistep laser excitation of ground state atoms, Rydberg states may be populated and observed with a high degree of selectivity: an analysis of an individual SFI spectrum yields information on the initial magnetic sublevel population of Rydberg atoms [19].

For the experiments described in this thesis, the selective field ionization pulse, required for ionization of Rydberg atoms, is applied to one of the electric field plates shown in Fig. 2-3. Figure 2-8 provides a closer look at these plates. There are three holes in each plate to let the cooling and trapping laser beams into the trap, and for trap imaging and ion detection purposes. When varying the electric field, each Rydberg state is ionized when the field reaches the threshold value necessary for its ionization. The resultant ions (or electrons) are pushed to the microchannel plate detector (MCP) by the same electric field that produces them, and the detected signal is amplified and sent to a boxcar integrator for data analysis. A graph of the ionization pulse and the detected signals corresponding to two Rydberg states is shown in Fig. 2-9. Details of SFI and MCP equipment are explained in Ref. [7].

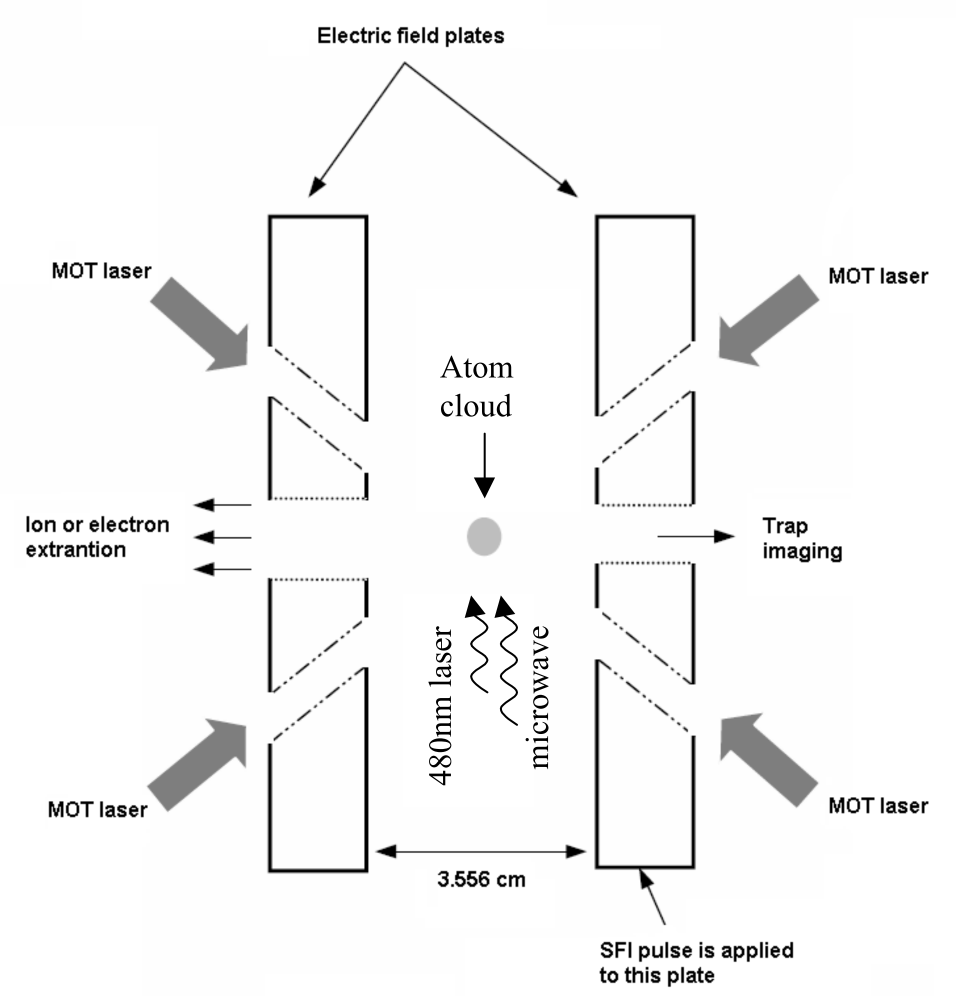

Figure 2-8: The electric field plates used for selective field ionization of Rydberg atoms (from Ref. [7]).

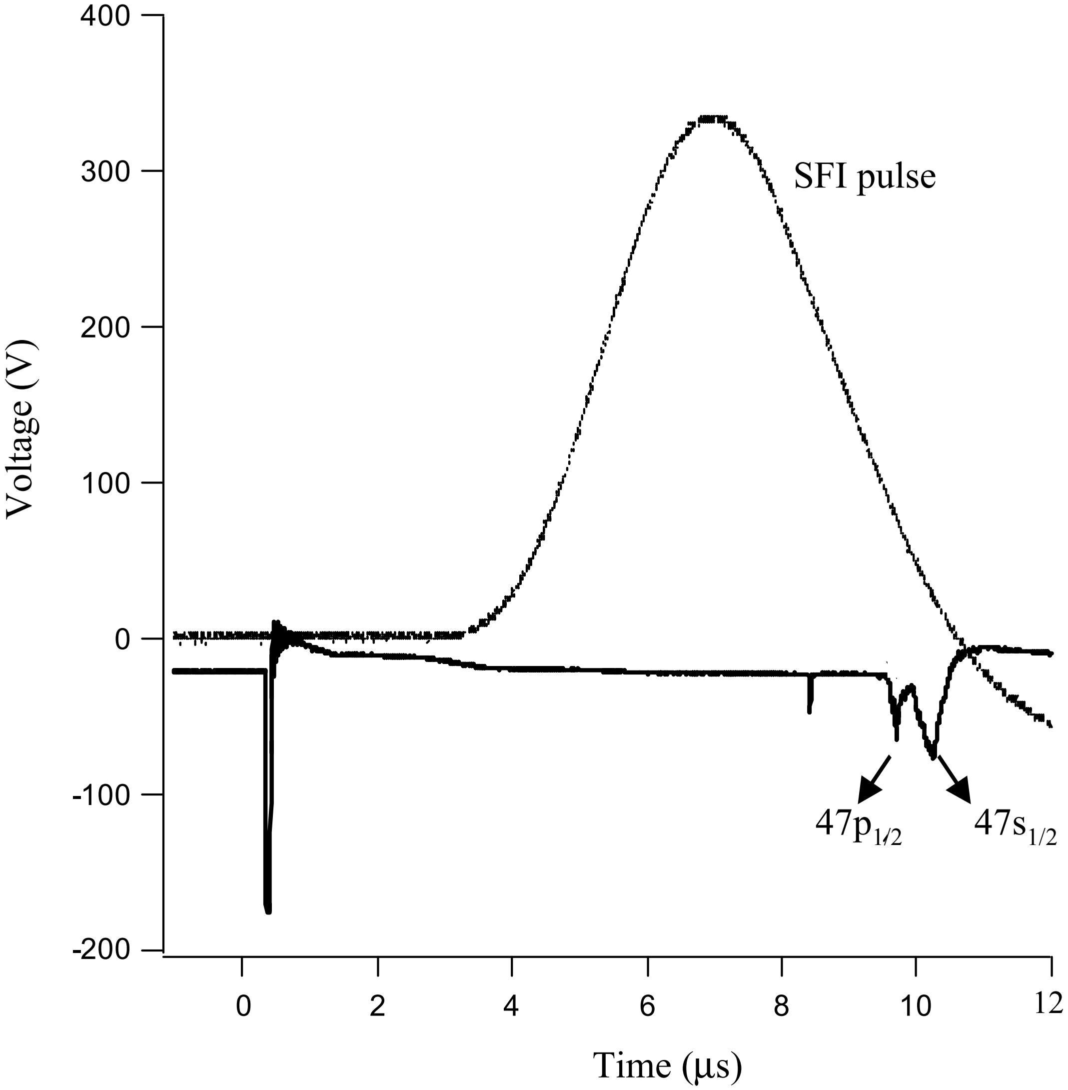

Figure 2-9: Selective field ionization pulse, and amplified MCP signal for two Rydberg states. Time is measured relative to the start of the excitation laser pulse.

Bibliography

[1] T. F. Gallagher, "*Rydberg Atoms*", Cambridge University Press 1994.

[2] R. F. Stebbings and F. B. Dunning, "*Rydberg states of atoms and molecules*", Cambridge University Press, 1983.

[3] H. J. Metcalf and P. van der Straten, "*Laser cooling and trapping*", Springer 1999.

[4] E. Raab, M. Prentiss, A. Cable, S. Chu, and D. Pritchard, "*Trapping of neutral sodium atoms with radiation pressure*", Phys. Rev. Lett. 59, 2631 (1987).

[5] K. L. Corwin, Z. T. Lu, C. F. Hand, R. J. Epstein, and C. E. Wieman, "*Frequency-stabilized diode laser with the Zeeman shift in an atomic vapor*", Appl. Opt. 37, 3295 (1998).

[6] Daryl W. Preston, "*Doppler-free saturated absorption: Laser spectroscopy*", Am. J. Phys. 64, 1432 (1996).

[7] Parisa Bohlouli Zanjani, *High resolution microwave spectroscopy of ultra cold Rydberg atoms as a probe of electric and magnetic fields*, Master's thesis, University of Waterloo, 2003.

[8] J. A. Schiavone, D. E. Donohue, D. R. Herrick, and R. S. Freund, "*Electron-impact excitation of helium: cross sections, n, and l distributions of high Rydberg states*", Phys. Rev. A 16, 48 (1977).

[9] J. A. Schiavone, S. M. Tarr, and R. S. Freund, "*Electron-impact excitation of the rare-gas atoms to high-Rydberg states*", Phys. Rev. A 20, 71 (1979).

[10] J. E. Bayfield, G. A. Khayrallah, and P. M. Koch, "*Production of fast highly excited atoms in proton collisions with atomic hydrogen and argon*", Phys. Rev. A 9, 209 (1974).

[11] F. A. Jenkins and E. Segre, "*The Quadratic Zeeman effect*", Phys. Rev. 55, 52 (1939).

[12] P. M. Dehmer and W. A. Chupka, "*Very high resolution study of photoabsorption, photoionization, and predissociation in* H_2", J. Chem. Phys. 65, 2243 (1976).

[13] G. Herzberg and C. Jungen, "*Rydberg series and ionization potential of the* H_2 molecule", J. Mol. Spectrosc. 41, 425 (1972).

[14] D. Kleppner, M. G. Littman, and M. L. Zimmerman, in "*Rydberg states of atoms and molecules*", edited by R. F. Stebbing and F. B. Dunning, Cambridge University Press 1983.

[15] M. Zimmerman, M. G. Littman, M. M. Kash, and D. Kleppner, "*Stark structure of the Rydberg states of alkali-metal atoms*", Phys. Rev. A 20, 2251 (1979).

[16] H. A. Bethe and E. A. Salpeter, "*Quantum mechanics of one and two electron atoms*", Plenum, New York 1977.

[17] G. K. Woodgate, "*Elementary atomic structure*", Second edition, Oxford science publications, 1980.

[18] T. F. Gallagher, L. M. Humphery, W. E. Cooke, R. M. Hill, and S. A. Edelstein, "*Field ionization of highly excited states of sodium*", Phys. Rev. A 16, 1098 (1977).

[19] T. H. Jeys, G. B. McMillian, K. A. Smith, F. B. Dunning, and R. F. Stebbings, "*Electric field ionization of highly excited sodium nd atoms*", Phys. Rev. A 26, 335 (1982).

[20] E. Luc-Koenig and A. Bachelier, "*Systematic theoretical study of the Stark spectrum of atomic hydrogen I: density of continuum states*", J. Phys. B: Atom. Molec. Phys. 13, 1743 (1980).

[21] C. Fabre, M. Gross, J. M. Raimond, and S. Haroche, "*Measuring atomic dimensions by transmission of Rydberg atoms through micrometer size slits*", J. Phys. B: At. Mol. Phys. 16, L671 (1983).

[22] M. T. Frey, X. Ling, B. G. Lindsay, K. A. Smith, and F. B. Dunning, "*Use of the Stark effect to minimize residual electric fields in an experimental volume*", Rev. Sci. Instrum. 64, 3649 (1993).

[23] A. Osterwalder and F. Merkt, "*Using high Rydberg states as electric field sensors*", Phys. Rev. Lett., 82, 1831 (1999).

[24] J. M. Raimond, G. Vitrant, and S. Haroche, "*Spectral line broadening due to the interaction between very excited atoms: the dense Rydberg gas*", J. Phys. B 14, L655 (1981).

[25] W. R. Anderson, J. R. Veale, and T. F. Gallagher, "*Resonant dipole-dipole energy transfer in a nearly frozen Rydberg gas*", Phys. Rev. Lett. 80, 249 (1998).

[26] I. Mourachko, D. Comparat, F. de Tomasi, A. Fioretti, P. Nosbaum, V. M. Akulin, and P. Pillet, "*Many-body effects in a frozen Rydberg gas*", Phys. Rev. Lett. 80, 253 (1998).

[27] W. R. Anderson, M. P. Robinson, J. D. D. Martin, and T. F. Gallagher, "*Dephasing of resonant energy transfer in a cold Rydberg gas*", Phys. Rev. A 65, 063404 (2002).

[28] I. Mourachko, W. Li, and T. F. Gallagher, "*Controlled many-body interactions in a frozen Rydberg gas*", Phys. Rev. A 70, 031401 (2004).

[29] M. D. Lukin, M. Fleischhauer, and R. Cote, "*Dipole Blockade and quantum information processing in mesoscopic atomic ensembles*", Phys. Rev. Lett. 87, 037901 (2001).

[30] D. Tong, S. M. Farooqi, J. Stanojevic, S. Krishnan, Y. P. Zhanq, R. Cote, E. E. Eyler, and P. L. Gould, "*Local blockade of Rydberg excitation in an ultracold gas*", Phys. Rev. Lett. 93, 063001 (2004).

[31] K. Singer, M. Reetz-Lamour, T. Amthor, L. G. Marcassa, and M. Weidemuller, "*Suppression of excitation and spectral broadening induced by interactions in a cold gas of Rydberg atoms*", Phys. Rev. Lett. 93, 163001 (2004).

[32] K. Afrousheh, P. Bohlouli-Zanjani, D. Vagale, A. Mugford, M. Fedorov, J. D. D. Martin, "*Spectroscopic observation of resonant electric dipole-dipole interactions between cold Rydberg atoms*", Phys. Rev. Lett. 93, 233001 (2004).

Chapter 3

Calibration of The Electric and Magnetic Fields

3.1 Introduction

Due to the MOT configuration, cold atoms experience an inhomogeneous magnetic field produced by a pair of anti-Helmholtz coils (AHCs). There are also sources of stray electric and magnetic fields in our MOT. Stray electric fields can be produced, for example, by the microchannel plate detector and the Rb dispenser. Stray magnetic field, on the other hand, are produced by the earth and an ion pump.

In this chapter, I initially explain the motivation for compensating for stray fields. Then, the properties of the inhomogeneous magnetic field of the AHCs are presented and the way AHCs are switched off is described. In the final section, the use of microwave transitions between Rydberg states for studying and compensating stray electric and magnetic fields is explained.

3.2 Motivations for compensating stray fields

For several reasons we would like to eliminate the stray fields in the trap region. Because of the Stark and Zeeman effects [1, 2], stray fields can mix atomic energy levels and make it difficult, and sometimes impossible, to excite a particular atomic level. In addition, stray fields broaden atomic transitions and reduce our sensitivity to detect physical phenomena such as the dipole-

dipole interaction between highly excited atoms. Also, in order to apply a well-defined field for some experiments, we need to know what fields are already present. For the same reasons, we sometimes need to switch off the AHCs.

3.3 Switching off the anti-Helmholtz coils

The strength of the inhomogeneous magnetic field produced by AHCs in the trap region depends on the coils' current. For an AHCs current of 9.5 A, the magnetic field has an inhomogeneity of 12, 12, and 24 G / cm. The Rydberg cloud in these experiments has a Gaussian profile with FWHMs of 0.190 ± 0.015 mm in two dimensions (dictated by the Rydberg excitation laser) and 0.5 ± 0.1 mm in the third dimension (dictated by the trap size). Measurements of the profile of the Rydberg cloud are presented in Appendix A. The largest magnetic field gradient is along the coils' common axis, which corresponds to the largest dimension of the Rydberg cloud. Therefore, cold atoms experience a magnetic field strength which varies between 0 and approximately 1.2 G. This gives a root mean square (RMS) magnetic field of approximately 0.5 G. The Zeeman shift of atomic energy levels is on the order of 1 MHz / G, as described in section (3-4-2). Therefore, the upper value of the magnetic field is large enough to affect the results of our experiments, as I will explain later. To avoid the line broadening due to the inhomogeneous magnetic field, it should be turned off before doing certain experiments. We have to minimize the amount of time that the MOT is off so that we do not lose a significant number of cold atoms. On the other hand, we have to take into account the fact that switching off the large AHCs current produces an induced magnetic field due to eddy currents (see, for example, Ref. [3]). We need to wait for the eddy currents to die down to an appropriate level before we can conduct our experiments.

Figure (3-1) shows how the magnetic field changes in the trap after turning the AHCs off. The magnetic field measurement was done by placing a Gaussmeter (MEDA μMAG) at the large fused silica window of the MOT (see Fig. 2-3). The time constant of the Gaussmeter (which indicates its response to field changes) was measured to be 1.6 ms. To measure this time constant, a magnetic field was produced by running a current through a wire, then the current was switched off and the time in which the magnetic field (showed by Gaussmeter) had dropped to $1/e$ of its maximum value was measured. To confirm this measurement, a second experiment was carried out in which an ac magnetic field was produced by running an ac current (sine function) through a wire, and the produced magnetic field was measured by the Gaussmeter. Then, the frequency of the applied current was increased until the amplitude of the measured magnetic field dropped to $1/\sqrt{2}$ of its low frequency value. In both measurements, a time constant of 1.6 ms was obtained.

The AHCs current was brought to zero in approximately 1.7 ms (see Fig. (3-1-a). The resulting magnetic field decay is shown in log-linear scale in Fig. (3-1-c). The time constant of the magnetic field decay shown on this graph was measured to be 6.5 ± 0.5 ms; therefore, the obtained behavior of the magnetic field is not due to the time response of the magnetic field sensor. Based on the result of this measurement, the inhomogeneous magnetic field, measured at the large fused silica window of the MOT, almost dropped to zero 25 ms after shutting the AHCs off. As mentioned before, the RMS magnetic field due to the quadrupole field was calculated to be 0.5 G. According to the exponential decay of the field gradient, 25 ms after the coils' current is shut-off the RMS magnetic field is expected to decay to 8 mG. This inhomogeneity is insignificant in the dipole-dipole interaction experiments discussed in the next chapter. An upper bound was put on this field using the microwave spectroscopy of Rydberg atoms, and will be discussed later in this chapter.

The circuit used for switching off the AHCs is shown in Fig. (3-2). The basics of operation of this circuit is as follows: this circuit essentially increases the on and off switching speed of a high current supply. When current supply is on, Q1 and Q2 shown on Fig. (3-2) are switched on, and current flows through the AHCs and is sunk by Q2. R3 controls the amount of time that Q2 stays on. When this time is over (when the desired current is reached), Q2 turns off leaving Q1 to sink the current from the AHCs and external current supply. During turn-off, Q1 is switched off and current flows through the AHCs and D3 until the energy in the coils is dissipated. SW1 allows the circuit to be bypassed so that the coils stay energized continuously. V_{on} is the turn-on voltage; the higher the voltage, the shorter the turn-on time. This was set to 100 V for the experiments in this thesis.

Although the inhomogeneous magnetic field was switched off, we still had a reasonable number of trapped atoms after 25 ms, and it was possible to do the measurements at this time.

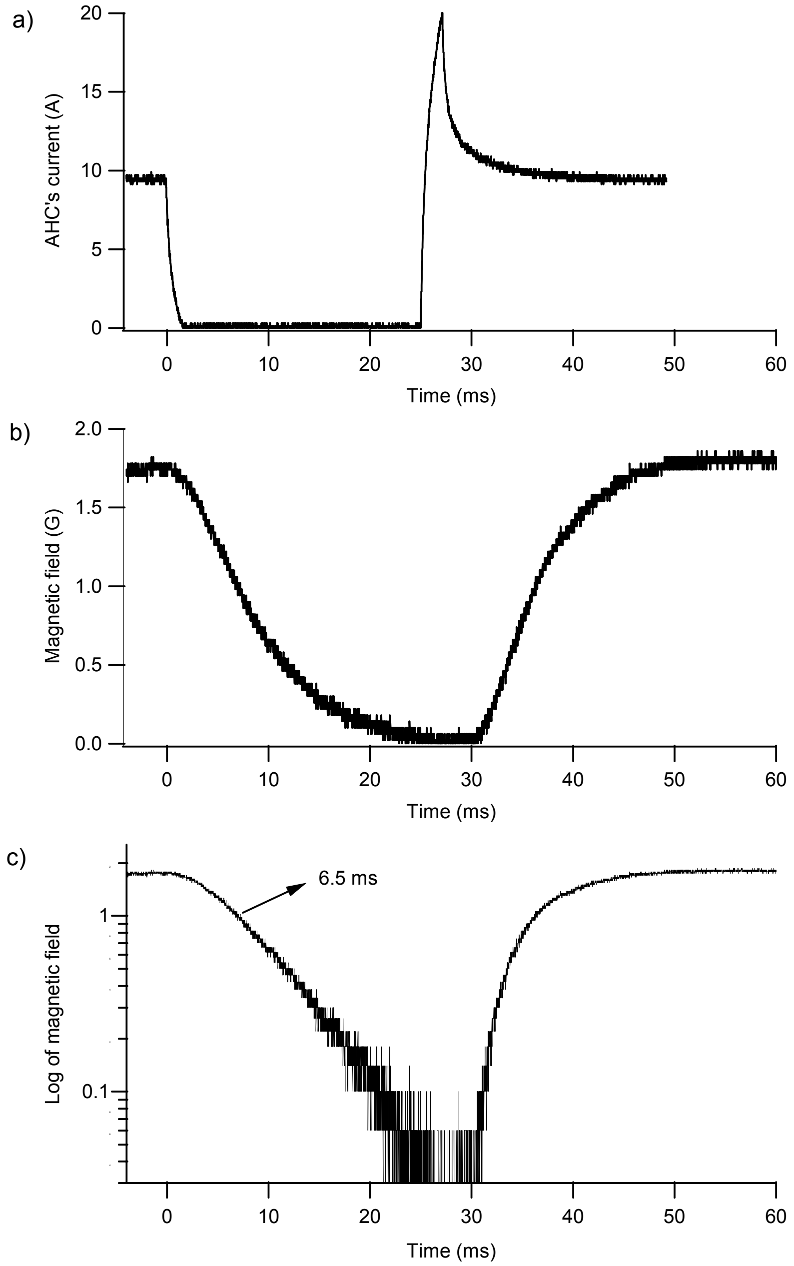

Figure 3-1: Inhomogeneous magnetic field falling off when the anti-Helmholtz coils are turned off for 30 ms; a) AHCs current versus time, b) inhomogeneous magnetic field decay in time, and c) magnetic field decay in time (log-linear graph). Time is measured relative the switching off of AHCs.

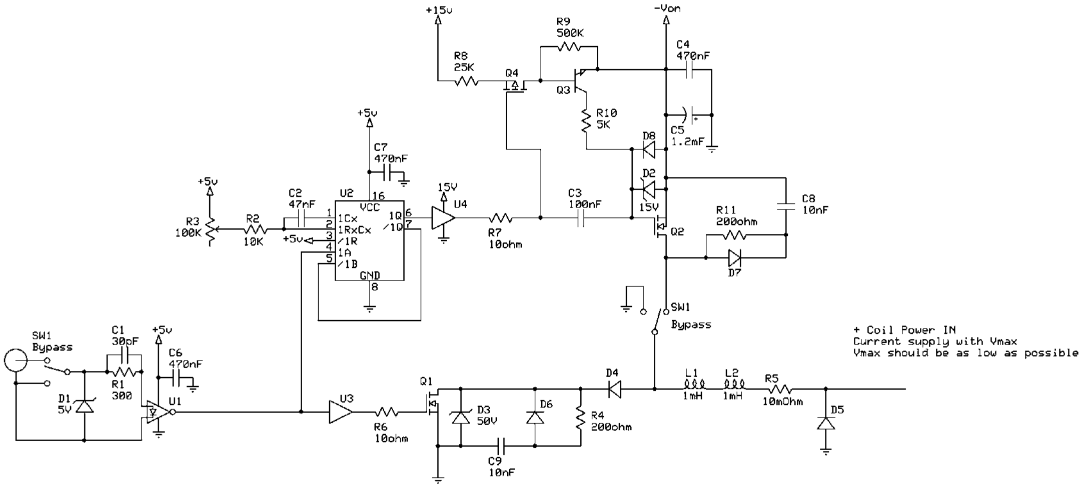

C2 = 22nF polyester film
D1 = 5V TVS (SA5.0ACCCT)
D2 = 15V TVS (SA15ACCCT)
D3 = 50V (can be changed), 2W continous TVS
D4 = 600V, 15A diode (15ETL06)
D5 = Schottky Diode
D6, D7 = 200V, 1A ultra-fast diode (MUR120RLOSCT)
D8 = 30V, 5A Schottky Diode (CMS04)
L1 and L2 = AntiHelmholtz Coils (1mH each)
Q1 = 600V, 70mOhm, 47A N-MOSFET (SPW47N60C2)
Q2 = 900V, 10A N-MOSFET (2SK2968)
Q3 = NPN bipolar transistor (2N3904)
Q4 = 400V, 1.8A N-MOSFET (IRFU9310)
R3 = 100K, 10 turn precision pot
R5 = 10mOhm current sense resistor (CS3FR010)
R6, R7 = reduce turn on transients
U1 = Optoisolator, TTL output (PS9611)
U2 = Monostable Multivibrator, TTL (CD74HCT4538)
U3, U4 = Mosfet Driver, TTL input (UCC27324P)
All non-standard parts obtained from Digi-Key Canada

Figure 3-2: The circuit that was used to switch the AHCs off and quickly turn back on, was built by Ashley Mugford at the University of Waterloo.

The detuning of the cooling and trapping laser, and the relative power of the counterpropagating MOT beams were optimized to keep the atoms in the trap during this waiting period. We need to compensate for stray magnetic fields so that the zero of the inhomogeneous magnetic field lies at the center of the AHCs. This keeps the zero of the magnetic field in the same place when the AHCs are switched off, and prevents the cold atoms from being pushed off to one side. Immediately after the experiment is done, the current to the AHCs is turned back on to recapture cold atoms for the next shot.

3.4 Studying microwave transitions for stray field compensation

Microwave transitions between highly excited Rydberg states were used to study and compensate for stray electric and magnetic fields. The sensitivity to small changes in electric and magnetic fields makes Rydberg atoms perfect tools for this study [2, 3]. Another reason for using microwaves in these experiments is that they can be generated with high frequency stability. In addition, long microwave pulse lengths can be used (for narrow linewidths) to improve the sensitivity of the measurements. Redistribution of Rydberg state population due to thermal radiation limits the microwave pulse length. A microwave pulse length of $36\,\mu$s was used for the experiments presented in this chapter. Although the resonant electric dipole-dipole experiments (presented in the next chapter) were done using energy levels with principal quantum number $n \approx 46$, for electric and magnetic field calibration we used $34s_{1/2} \rightarrow 34p_{1/2}$ microwave transition. The separation of hyperfine states and magnetic sublevels are larger at lower n (these scale as $1/n^3$) [1]; therefore, it is easier to observe transitions between individual energy sublevels for the purpose of detection and measurement of homogeneous and inhomogeneous fields.

3.4.1 Electric field

Electric fields shift the atomic energy levels due to the Stark effect. Stark shifts of atomic transitions have been used for stray electric field measurements [2,3]. M. T. Frey *et al.* [4] used transitions from the ground state to Rydberg states in potassium to compensate homogeneous electric fields to less than $50\,\mu\mathrm{V}\,/\,\mathrm{cm}$, and A. Osterwalder *et al.* [5] exploited millimeter wave spectroscopy of the krypton atom to monitor compensation of homogeneous and inhomogeneous electric fields with a $20\,\mu\mathrm{V}\,/\,\mathrm{cm}$ accuracy.

Due to Stark shifts, the $34s_{1/2} \rightarrow 34p_{1/2}$ transition is shifted to lower frequencies in the presence of an electric field. The plot of microwave transition frequency versus electric field has a parabolic form, since we are dealing with the quadratic Stark effect. To compensate for the stray electric field in a given direction, we apply different electric fields in that direction and record the center value of the microwave transition frequency for the above mentioned transition. Plotting transition frequencies versus electric field values gives a parabola whose apex provides the compensating electric field that we should apply in this direction. This should be done for all three orthogonal directions. Because of the configuration of our magneto-optical trap, we are not able to independently apply electric fields along each axis. Instead, we control the electric field in the vacuum chamber by controlling the voltage of the Rb dispenser relative to the grounded chamber, and also the average and differential voltages of the electric field plates (see Fig 2-3). We find the optimum values of the average and differential voltages of the plates and the voltage of the Rb dispenser in the way explained above. This process is repeated iteratively to improve the optimum field values. Figure (3-3) is an example of such an experiment that shows the change in microwave transition frequency in terms of the differential voltage of the electric field plates. The microwave transition frequency increases after each optimization. We continue this process until the change in transition frequency falls within the experimental error in finding the apex of the parabolic fit. This error was approximately 1 kHz in our measurements. We take the electric field corresponding to the frequency change of 1 kHz to be the upper bound of stray electric field in our setup, which is $10\,\mathrm{mV}\,/\,\mathrm{cm}$.

One of the sources of stray electric fields in our experiments is charged particles produced during photoexcitation or by collisions of Rydberg atoms with other particles in the MOT. These ions appear early in time in field ionization signals as they are free and are pushed to the microchannel plate detector (MCP) by a small electric field. Figure (3-4) shows a field ionization spectrum including ion signal (labeled by ions), and Rydberg state signals. These charged particles produce an inhomogeneous electric field [6]. To estimate the electric field produced by these ions in our setup, we need to know the density of ions. Knowing the density

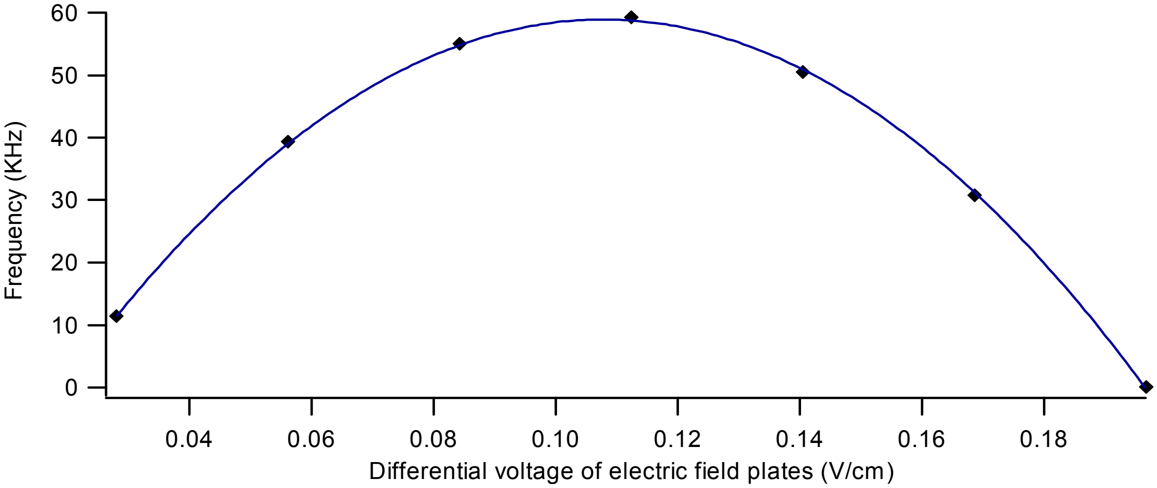

Figure 3-3: Microwave transition frequency as a function of differential voltage of electric field plates. The apex of this parabola gives the optimum value of differential voltage. The vertical axis shows the frequency of microwave transition which is offset by 104.1039595 GHz. The horizontal axis values were obtained by dividing differential voltages by the distance beween the electric field plates.

of Rydberg atoms, the ion density may be obtained approximately by comparing the selective field ionization signal of ions to that of Rydberg atoms. The fraction of ions to Rydberg atoms obtained this way using Fig. (3-4) is approximately 0.5%. Therefore, with a Rydberg atom density of $n_{Ryd} = 1 \times 10^7\,\mathrm{cm}^{-3}$ (see Appendix A for density measurements), we get $n_{ion} = 5 \times 10^4\,\mathrm{cm}^{-3}$ for the ion density. It is explained in Ref. [10] that for a given ion density, approximately 95% of the electric fields produced by the ions is less than

$$E_{\max}(n_{ion}) = 2.78 \times 10^{-8}\ (\,\mathrm{V}\,/\,\mathrm{m}\,)\ n_{ion}^{2/3}. \tag{3.1}$$

The value of $E_{\max}$ for the ion density given above is roughly $4\,\mathrm{mV}\,/\,\mathrm{cm}$. This is lower than the error in compensating stray electric fields, meaning that the inhomogeneous electric field produced by the ions is negligible.

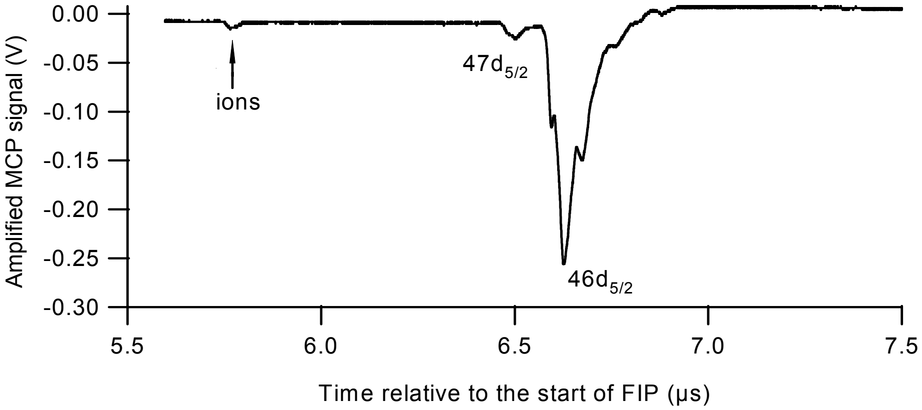

Figure 3-4: Amplified microchannel plate detector signal corresponding to ions and two Rydberg states. The zero time is when the field ionization pulse is applied.

3.4.2 Magnetic field

Atomic spectroscopy has been used for the calibration and compensation of magnetic fields [7]. To compensate for stray magnetic fields, S. Kuhr *et al.* [7] used three pairs of Helmholtz coils to minimize the Zeeman splitting of the hyperfine ground state m_F manifold of cesium which was probed by microwave spectroscopy. Using this method, they achieved residual magnetic fields of $B_{res} < 4$ mG, with the limit being determined by the accuracy within which they could change the coils currents. The earth's magnetic field and an ion pump are two known sources of unwanted stray magnetic fields in our MOT. To calibrate magnetic fields, and compensate for stray fields, we use the one-photon $34s_{1/2} \rightarrow 34p_{1/2}$ microwave transition.

To investigate the effect of magnetic fields on atomic energy levels, the following perturbation should be considered [8]

$$H = -\frac{\mu_B B}{IJ\hbar^2} I \cdot J + \frac{\mu_B g_J B}{\hbar} J_z - \frac{\mu_B B}{\hbar} I_z, \tag{3.2}$$

where I and J are the nuclear spin and total angular momentum of the electron, respectively, and μ_B is the Bohr magneton. In order to find the Zeeman splittings of the atomic energy levels, the eigenvalues of this Hamiltonian should be calculated. Neglecting the last term of this Hamiltonian relative to the others, the shift of the hyperfine structure in a magnetic field for $J = 1/2$ is given by the Breit-Rabi formula [8]

$$\Delta E = -\frac{h\Delta\nu}{2(2I+1)} \pm \frac{h\Delta\nu}{2}\left(1 + \frac{4m_F}{2I+1}x + x^2\right)^{1/2},$$

$$\Delta E = \frac{I}{2I+1}h\Delta\nu \pm \frac{1}{2}g_J\mu_B B, \qquad \text{for } m_F = \pm\left(I + \frac{1}{2}\right) \tag{3.3}$$

where $x = B\mu_B g_J/(h\Delta\nu)$, and $\Delta\nu$ is the hyperfine splitting at the absence of magnetic fields. By measuring the zero field hyperfine splittings of $28s$ and $33s$ states of ^{85}Rb, W. Li *et al.* [9] found the following relationship for the ns hyperfine intervals [10]

$$\Delta\nu = 14.6(\pm 1.4)\,\text{GHz}(n^*)^{-3}, \tag{3.4}$$

where $n^* = n - \delta_s$ is the effective principal quantum number, and δ_s is the quantum defect of the s state. For $s_{1/2}$ states, $\delta_s = 3.1311804$ [9]. The hyperfine interval of the $34s_{1/2}$ state can be obtained using equation (3.4), and the hyperfine intervals of $34p_{1/2}$ can be measured using microwave spectroscopy, as will be explained later. Knowing the zero field hyperfine intervals, Eq. (3.3) can be used to find the Zeeman shifts of different energy states in different magnetic fields. The Zeeman shifts of the $34s_{1/2}$ and $34p_{1/2}$ states are shown on Fig. (3-5).

The $34s_{1/2}$ Rydberg state of rubidium is excited in a two-colour, two-photon process including the red-detuned 780 nm cooling and trapping laser and a 480 nm laser. The 780 nm laser is almost resonant with the $5s_{1/2}F = 3 \rightarrow 5p_{3/2}F = 4$ transition of rubidium, and the 480 nm light completes the excitation to the Rydberg state. To produce the 480 nm light, the 960 nm output of a CW Ti:sapphire laser (Coherent MBR-110) is frequency doubled in an external ring resonator (Coherent MBD 200). The electric dipole selection rule for F is $\Delta F = 0, \pm 1, F = 0 \nrightarrow F = 0$ [11]; therefore, F cannot be changed by more than one in a single photon transition. Since Rydberg state excitation starts from $F = 4$ of the $5p_{3/2}$ state, $F = 3$ is the only populated hyperfine state of $34s_{1/2}$ at zero magnetic field, and $34s_{1/2}F = 2$ is not excited. Therefore, the $34s_{1/2} \rightarrow 34p_{1/2}$ microwave transition shows two resonances at zero magnetic field, as shown on Fig. (3-6-a). These resonances correspond to

Figure 3-5: Splittings of the magnetic sublevels of $34s_{1/2}$ and $34p_{1/2}$ energy levels of ^{85}Rb due to the Zeeman effect, calculated using the Breit-Rabi formula, Eq. 3.3, and Eq. 3.4 for the hyperfine intervals.

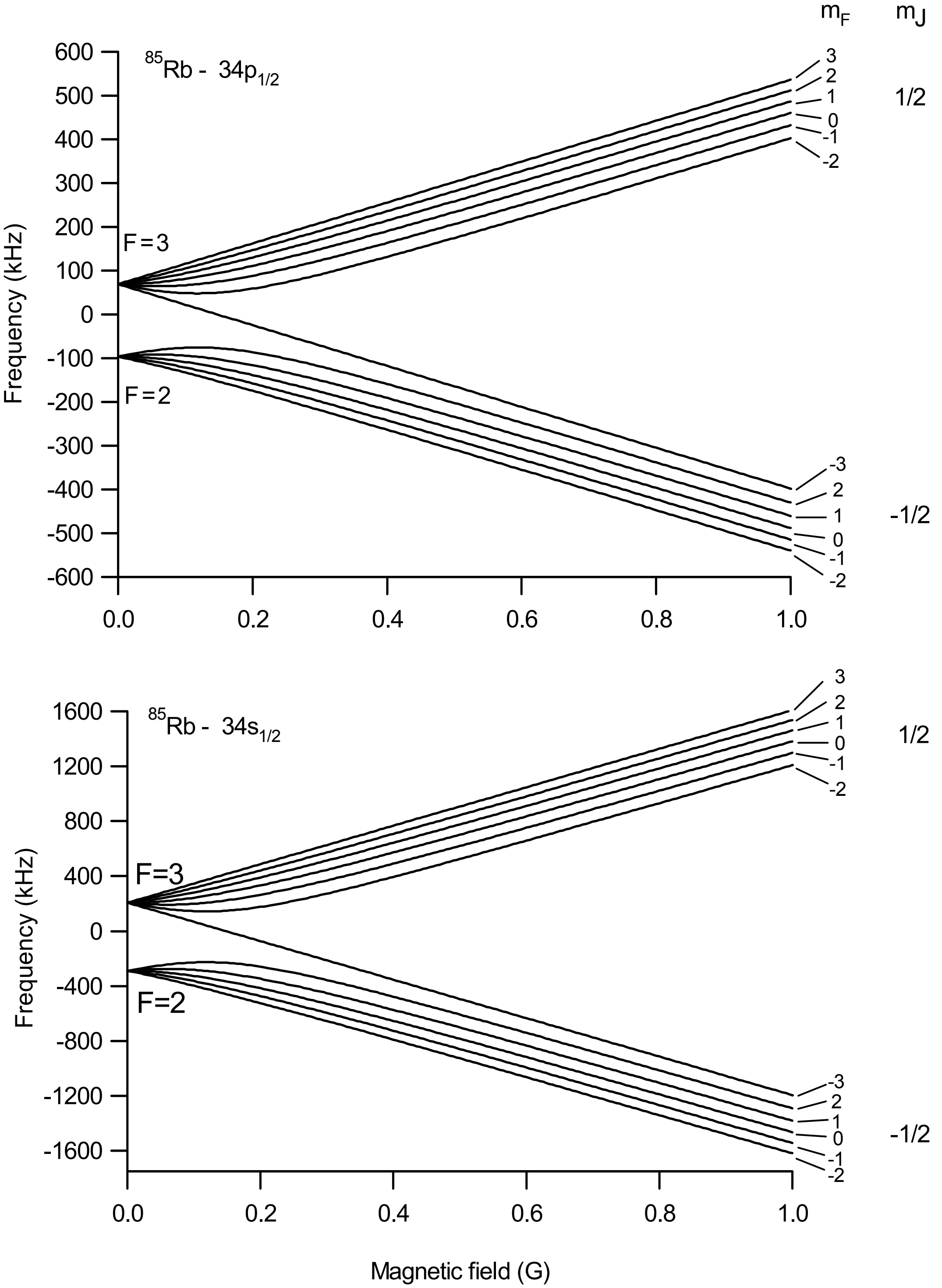

$34s_{1/2}, F = 3 \rightarrow 34p_{1/2}, F = 2$, and $34s_{1/2}, F = 3 \rightarrow 34p_{1/2}, F = 3$ transitions. The separation of these two transitions gives the hyperfine interval of $34p_{1/2}$ in the absence of a magnetic field. This was measured to be approximately $140 \pm 10\,\mathrm{kHz}$.

When a homogeneous magnetic field is applied, the magnetic sublevels of $34s_{1/2}$ and $34p_{1/2}$ are split due to the Zeeman effect, and as a result, the microwave transition between these two states has multiple peaks, as shown in Fig. (3-5) and Fig. (3-6-b). This can be used to guide the compensation for stray magnetic fields. We apply a DC magnetic field along an axis using a pair of compensation coils and record the coils' current. The inhomogeneous magnetic field, produced by AHCs, is switched off 25 ms before photoexcitation to Rydberg states. The detuning of the cooling and trapping laser and the relative power of the counterpropagating MOT beams are changed slightly to minimize the reduction in the number of cold atoms during the wait period. We scan the microwave frequency to drive the $34s_{1/2} \rightarrow 34p_{1/2}$ transition and take spectra. These spectra have multiple lines at different microwave frequencies. By changing the current of the same Helmholtz coils, we try to apply a magnetic field with the same magnitude in the opposite direction. The spectral lines of the $34s_{1/2} \rightarrow 34p_{1/2}$ transition should match those of the opposite magnetic field. The average of these two currents nulls the stray magnetic field along this axis. This procedure is followed for all three orthogonal axes, and the obtained nulling currents were: $I_x = -91 \pm 1\,\mathrm{mA}$, $I_y = -58 \pm 1\,\mathrm{mA}$, $I_z = -395 \pm 1\,\mathrm{mA}$, where x is the axis perpendicular to the electric field plates, y is the axis pointing towards the ion pump in our setup, and z is along the AHCs' axis (see Fig. 2-3). The signs of these currents are chosen so that increasing currents produces larger magnetic fields in the three directions mentioned above. The uncertainty in setting the currents of the magnetic coils determines the upper limit of the homogeneous magnetic field in our MOT, which was determined to be 6 mG.

To investigate the effect of a DC magnetic field on the linewidth broadening due to resonant electric dipole-dipole interaction, we need to apply a known DC magnetic field in a given direction. This can be done by changing the current of a pair of nulling coils from the zero magnetic field value. The magnitude of the applied magnetic field can be calculated using the coils' geometry. Microwave spectroscopy, however, can be used to calibrate magnetic fields more precisely. Figures (3-7) and (3-8) show the microwave spectra corresponding to the $34s_{1/2} \rightarrow 34p_{1/2}$ transition taken in different DC magnetic fields. For taking the spectra in Fig. (3-7), the

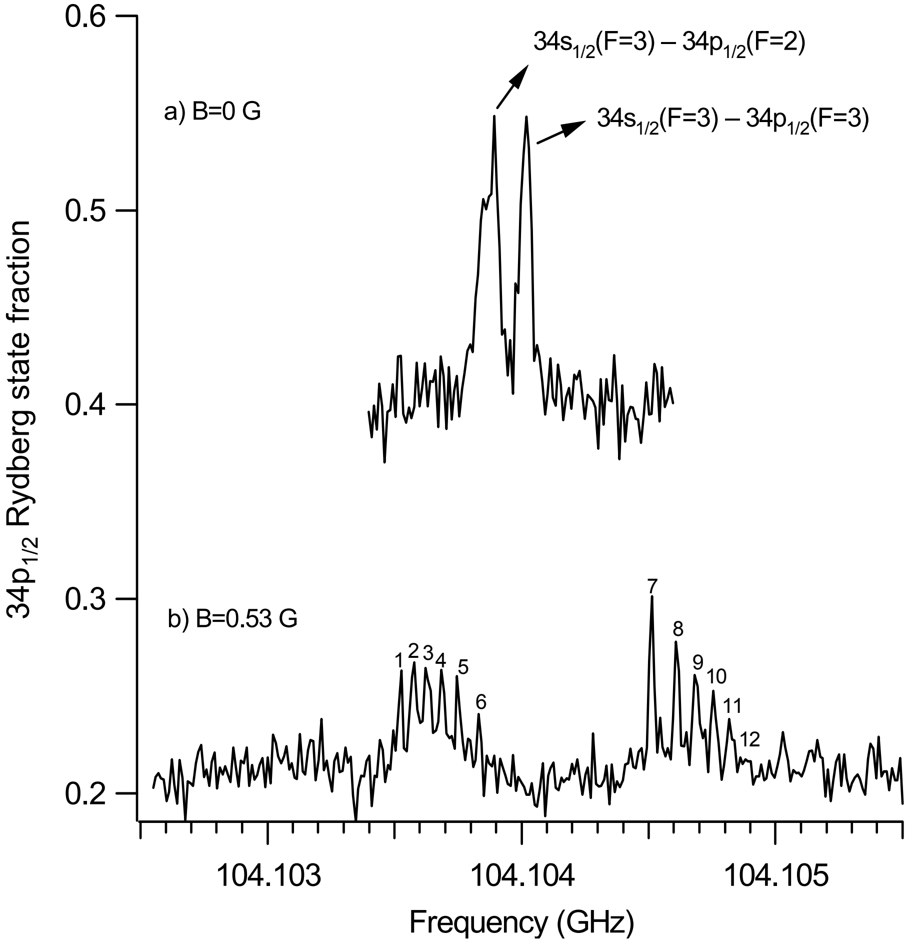

Figure 3-6: The single-photon microwave transition from $34s_{1/2}$ to $34p_{1/2}$ at a) zero applied magnetic field, where the two peaks are labeled, and b) an applied magnetic field of $0.53\,\mathrm{G}$. Data are offset vertically for clarity. Different peaks in b) correspond to:
1) $m_J = 1/2, m_F = 3 \rightarrow m_J = 1/2, m_F = 3$,
2) $m_J = 1/2, m_F = 2 \rightarrow m_J = 1/2, m_F = 2$,
3) $m_J = 1/2, m_F = 1 \rightarrow m_J = 1/2, m_F = 1$,
4) $m_J = 1/2, m_F = 0 \rightarrow m_J = 1/2, m_F = 0$,
5) $m_J = 1/2, m_F = -1 \rightarrow m_J = 1/2, m_F = -1$,
6) $m_J = 1/2, m_F = -2 \rightarrow m_J = 1/2, m_F = -2$,
7) $m_J = -1/2, m_F = -3 \rightarrow m_J = -1/2, m_F = -3$,
8) $m_J = -1/2, m_F = 2 \rightarrow m_J = -1/2, m_F = 2$,
9) $m_J = -1/2, m_F = 1 \rightarrow m_J = -1/2, m_F = 1$,
10) $m_J = -1/2, m_F = 0 \rightarrow m_J = -1/2, m_F = 0$,
11) $m_J = -1/2, m_F = -1 \rightarrow m_J = -1/2, m_F = -1$,
12) $m_J = -1/2, m_F = -2 \rightarrow m_J = -1/2, m_F = -2$.

polarization of the microwave radiation was parallel to the direction of the applied magnetic field, and for Fig. (3-8), the microwave polarization made an angle of roughly 30° with the magnetic field direction.

Single-photon transitions between hyperfine states should satisfy the selection rules: $\Delta F = 0$, $\Delta m_F = 0$, when microwave polarization is parallel to the applied magnetic field direction. Therefore, the number of spectral lines in Fig. (3-7) is less than that of Fig. (3-8), which makes it easier to identify different spectral lines. According to the Breit-Rabi formula, the positions of different spectral lines in this graph generally depend on the magnetic field and hyperfine splitting of $34s_{1/2}$ and $34p_{1/2}$. The exact values of these hyperfine splittings are unknown. However, there is a particular spectral line, corresponding to the $34s_{1/2}, m_F = -3 \rightarrow 34p_{1/2}, m_F = -3$ transition, whose frequency change in the magnetic field only depends on the magnetic field and not on the hyperfine spacing of the energy levels. This line, which is marked with arrows on Fig. (3-7), has a shift of $(2/3)\mu_B B$ ($\approx 0.93\,\mathrm{MHz}\,/\,\mathrm{G}$) in a magnetic field, where μ_B ($\approx 1.4\,\mathrm{MHz}\,/\,\mathrm{G}$) is the Bohr magneton, and B is the magnitude of the applied magnetic field. We plot the frequency of this line as a function of the coils' current and fit it with a straight line to find the relationship between the magnetic field and the coils' current. This plot is shown in Fig. (3-9). The slope of this line is $1.66\,\mathrm{MHz}\,/\,\mathrm{A}$, which gives the relationship between the magnetic field and the coils' current on this axis to be $B_x = 1.77 I_x$, with B in Gauss and I in Amperes. The magnetic field and current relations were also obtained based on the coils' geometry for the three orthogonal directions, and for the x axis on Fig. (2-3) we have $B_x = 1.68 I_x$ which is in good agreement with the previous relation. Since we will only apply a DC magnetic field in one direction for studying interatomic interaction, we only need to calibrate this component of the magnetic field very accurately. This calibration, however, can be done for the other components of the magnetic field, if necessary.

The linewidth of the transition marked on Fig. (3-7) can be used to determine the upper limit of the inhomogeneous magnetic field in the trap. The linewidth of this transition is measured to be almost $30\,\mathrm{kHz}$. The transform limited linewidth associated with a $36\,\mu$s long square pulse is approximately $25\,\mathrm{kHz}$. Assuming that, as a worst case, the linewidth contributions combine in quadrature, the residual line broadening due to the inhomogeneous magnetic field and other mechanisms is $17\,\mathrm{kHz}$. Knowing that the shift of this line in magnetic fields is $(2/3)\mu_B B$, the upper limit of the inhomogeneous magnetic field is measured to be roughly 17mG.

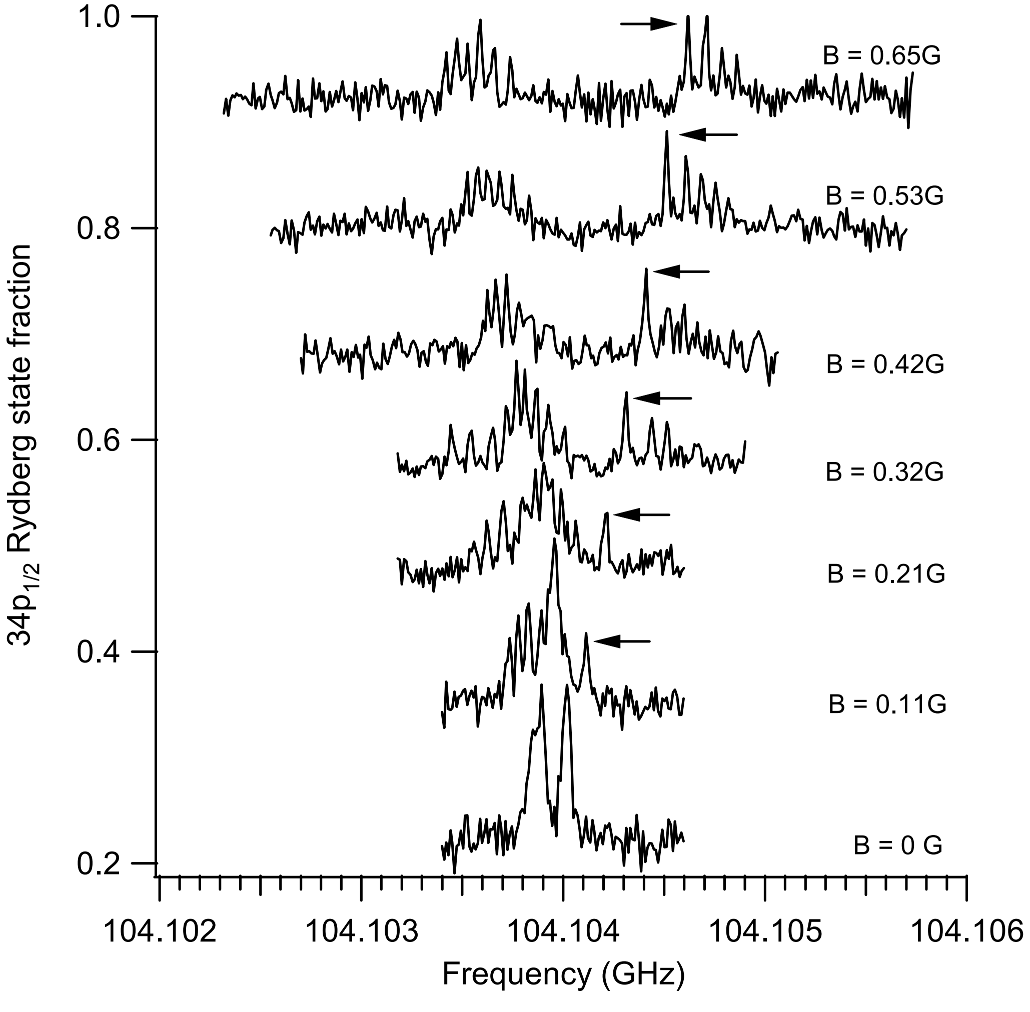

Figure 3-7: The one-photon $34s_{1/2} \rightarrow 34p_{1/2}$ microwave transition in different magnetic fields with microwave polarization parallel to the direction of the applied magnetic field. Data are offset vertically for clarity. Different transitions are labled on Fig. 3-6 for $B = 0.53$ G.

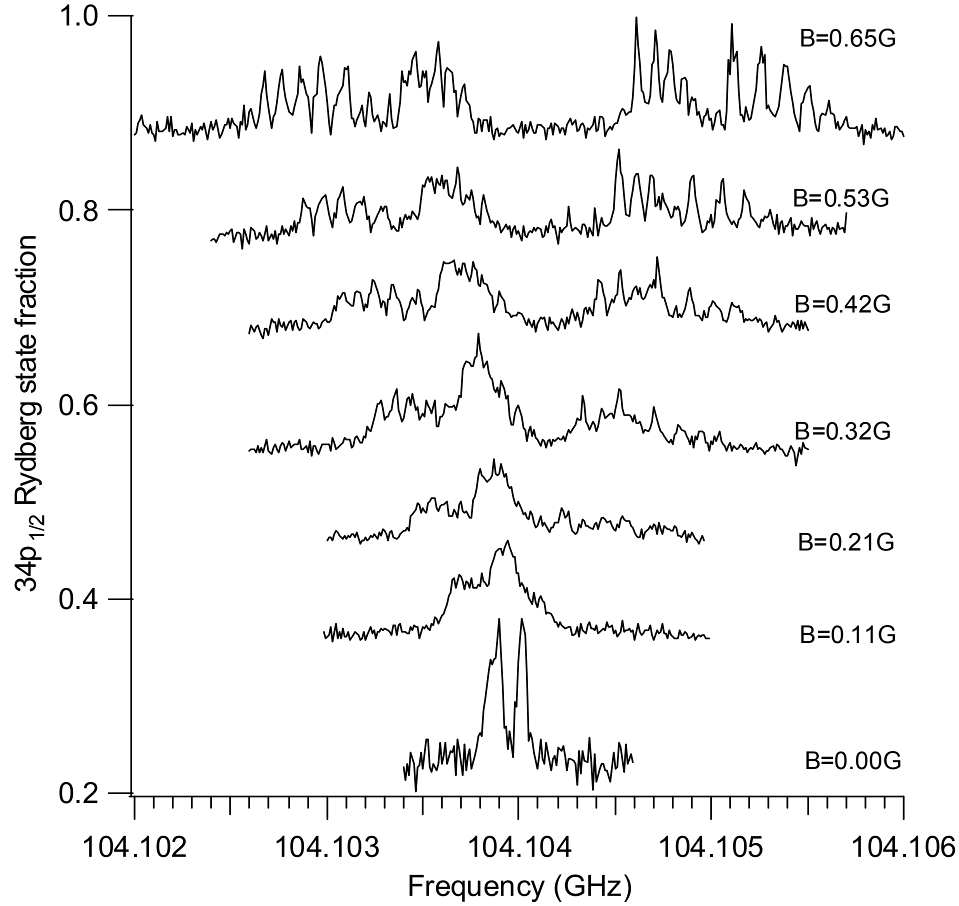

Figure 3-8: The one-photon $34s_{1/2} \rightarrow 34p_{1/2}$ microwave transition in different magnetic fields with the angle between the microwave polarization the magnetic field direction being $\sim 30°$. Data are offset vertically for clarity.

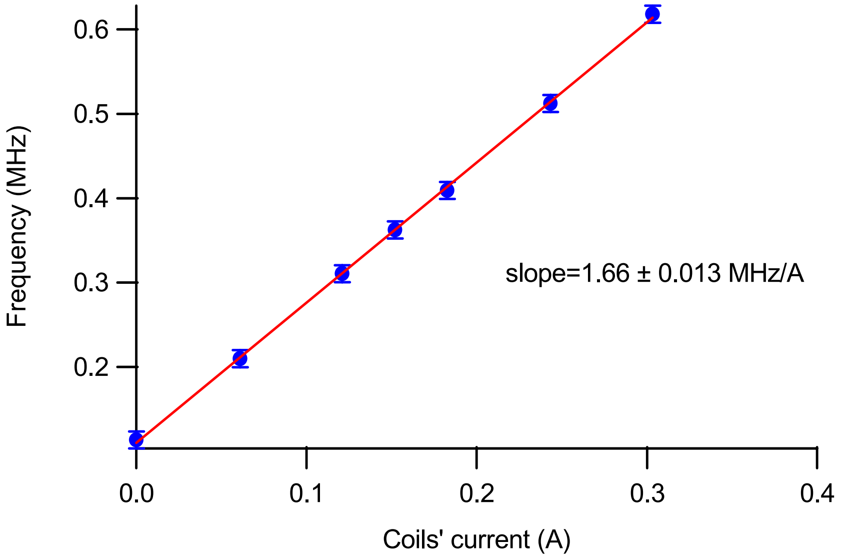

Figure 3-9: The position of the $34s_{1/2}, m_F = -3 \rightarrow 34p_{1/2}, m_F = -3$ transition as a function of the current of a pair of compensating coils which was used to calibrate the corresponding magnetic field component. The frequency values on vertical axis are offset by 104.104 GHz. The error bars on data values show the error in finding the transition peak position.

Bibliography

[1] Thomas F. Gallagher, "*Rydberg Atoms"*, Cambridge, 1st edition, 1994.

[2] D. Kleppner, M. G. Littman, and M. L. Zimmerman, in "*Rydberg states of atoms and molecules*", edited by R. F. Stebbing and F. B. Dunning, Cambridge University Press 1983.

[3] C. J. Dedman, K. G. H. Baldwin, and M. Colla, "*Fast switching of magnetic fields in a magneto-optic trap*", Rev. Sci. Instrum. 72, 4055 (2001).

[4] M. T. Frey, X. Ling, B. G. Lindsay, K. A. Smith, and F. B. Dunning, "*Use of the Stark effect to minimize residual electric fields in an experimental volume*", Rev. Sci. Instrum. 64, 3649 (1993).

[5] A. Osterwalder and F. Merkt, "*Using high Rydberg states as electric field sensors*", Phys. Rev. Lett., 82, 1831 (1999).

[6] D. Redfield, "*Electric fields of defects in solids*", Phys. Rev. 130, 914 (1963).

[7] J. Ringot, P. Szriftgiser, and J. C. Garreau, "*Subrecoil Raman spectroscopy of cold cesium atoms*", Phys. Rev. A, V. 65, pp. 013403, 2001. See also I. Dotsenko, "*Raman spectroscopy of single atoms*", Thesis work, Institute for Angewandte Physik der Universitat Bonn, Page 27 (2002).

[8] H. G. Kuhn, "*Atomic Spectra"*, Longmans, first edition, 1962.

[9] Wenhui Li, I. Mourachko, M. W. Noel, and T. F. Gallagher, "*Millimeter-wave spectroscopy of cold Rb Rydberg atoms in a magneto-optical trap: quantum defects of the ns and np, and nd series*", Phys. Rev. A, V. 67, pp. 052502, 2003.

[10] Parisa Bohlouli Zanjani, "*High resolution microwave spectroscopy of ultra cold Rydberg atoms as a probe of electric and magnetic fields*", Master's thesis, University of Waterloo, 2003.

[11] G. H. Woodgate, "*Elementary atomic structure*", Oxford science publications, 2nd edition, 1998.

Chapter 4

Observation of Resonant Electric Dipole-Dipole Interaction

4.1 Introduction

Resonant electric dipole-dipole interactions between cold Rydberg atoms were observed by optical excitation of laser cooled and trapped atoms to Rydberg states and manipulation of these states with microwaves. In this chapter, the details of the experiments on observation of resonant electric dipole-dipole interaction between cold Rydberg atoms are presented. Initially, an explanation of our method for the production of cold Rydberg atoms will be given, followed by a description of microwave spectroscopy of cold Rydberg atoms. The timing of the experiment is demonstrated next. Then, the details of the resonant electric dipole-dipole interaction and the results of the experiment are presented. This includes studies of the effect of hot Rydberg atoms and other particles in the trap on the linewidths of microwave transitions. Finally, the suppression of resonant electric dipole-dipole line broadening due to the presence of a DC magnetic field is explained.

4.2 Plan for observation of resonant electric dipole-dipole interaction

To study resonant electric dipole-dipole interactions between cold Rydberg atoms, laser cooled Rb atoms are first excited to a Rydberg state. A fraction of these atoms may then be transferred to another Rydberg state that is coupled to the first one through dipole-dipole interaction (see the last paragraph in this section for a discussion on how to verify the strength of the coupling between Rydberg states). In the presence of dipole-dipole interactions, the two Rydberg states of the two atoms involved are shifted, broadening the linewidths of the transitions including either of these states. Therefore, the linewidth broadening of a microwave transition to or from one of the Rydberg states may be used as a means of observing resonant dipole-dipole interactions.

The two Rydberg states that were excited in this work for the observation of resonant dipole-dipole interactions were $46d_{5/2}$ and $47p_{3/2}$, and the transition that was used as the probe of interatomic interactions was $46d_{5/2} - 47d_{5/2}$. To better understand the detail of this interaction we consider the dipole-dipole interaction between two atoms (A and B) which is given by:

$$\hat{\mathrm{V}}_{dd} = \frac{\overrightarrow{\mu}_A \cdot \overrightarrow{\mu}_B - 3\left(\overrightarrow{\mu}_A \cdot \hat{n}\right)\left(\overrightarrow{\mu}_B \cdot \hat{n}\right)}{R_{AB}^3}, \tag{4.1}$$

where $\overrightarrow{\mu}_A$ and $\overrightarrow{\mu}_B$ are the electric dipole matrix element operators evaluated on each atom, $\hat{n}$ is the unit vector pointing between the atoms, and R_{AB} is the separation of the two atoms. This perturbation may split the energy states $|1\rangle = |46d_{5/2} m_{j,A1}\rangle_A |47p_{3/2} m_{j,B1}\rangle_B$ and $|2\rangle = |47p_{3/2} m_{j,A2}\rangle_A |46d_{5/2} m_{j,B2}\rangle_B$ that are all degenerate in the absence of magnetic fields, where $|1\rangle$ and $|2\rangle$ refer to the energy states of the two-atom system. With a 50% mixture of $46d_{5/2}$ and $47p_{3/2}$ atoms we can obtain a very rough idea of the magnitude of the energy splittings from $\Delta v_{dd} \approx \mu^2/R^3$, where $\mu = |\langle 46d_{5/2,1/2}|\mu_z|47p_{3/2,1/2}\rangle| \approx 0.49 \times |\langle 46d_{5/2}|r|47p_{3/2}\rangle|$. The interatomic separation is given by $R = (4\pi n_{47p}/3)^{-1/3}$, where n_{47p} is the $47p_{3/2}$ number density. In this estimate, m_j is considered to be 1/2, r is the radial coordinate of the Rydberg electron, and the radial matrix element $\langle 46d_{5/2}|r|57p_{3/2}\rangle$ is evaluated by numerical integration of the Rydberg electron wave functions [1]. A density of $n_{47p} = 5 \times 10^6\,\mathrm{cm}^{-3}$ gives $\Delta v_{dd} = 33\,\mathrm{kHz}$. This means that in the presence of resonant electric dipole-dipole interactions, the two Rydberg states involved are shifted by roughly ±33 kHz.

Figure 4-1 shows several Rydberg states of ^{85}Rb together with the magnitudes of relevant electric dipole matrix elements $\langle nl_j|r|n\acute{l}_{\acute{j}}\rangle$. This matrix element is a measure of the strength of the dipole-dipole coupling between a pair of states. As shown in Fig. 4-1, resonant electric dipole-dipole interaction is strong between $46d_{5/2}$ and $47p_{3/2}$, and $46d_{5/2}$ and $45f$, and it is weak, for example, between $46d_{5/2}$ and $46p_{3/2}$ states. This suggests that the resonant electric dipole-dipole interaction can be observed by producing a mixture of either $46d_{5/2}$ and $47p_{3/2}$, or $46d_{5/2}$ and $45f$ cold Rydberg atoms. As seen on Fig. 4-1, when exciting $46d_{5/2}$ and $47p_{3/2}$ states, only the initial state of the two-photon probe transition is dipole coupled to $47p_{3/2}$ state and is split by the resonant dipole-dipole interaction with $47p_{3/2}$ atoms. Therefore, the introduction of the resonant dipole-dipole interaction is expected to give rise to a linewidth broadening on the order of $2\Delta v_{dd}$.

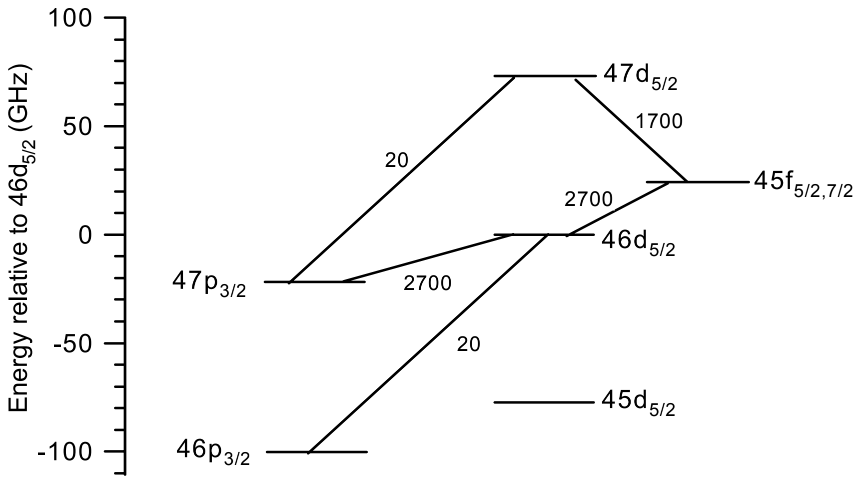

Figure 4-1: Energy levels of Rydberg states of rubidium relevant to our experiment. The electric dipole matrix elements magnitudes $\left\langle nl_j\left|r\right|n\acute{l}_{\acute{j}}\right\rangle$ are shown between appropriate states. These are calculated by numerical integration of the Rydberg electron wave functions [1]. Spectroscopic data are from reference [7].

4.3 Cold Rydberg atom production

4.3.1 Excitation scheme

To produce cold Rydberg atoms, laser cooled and trapped atoms are excited in a magneto-optical trap. Starting from the ground state of rubidium, $5s_{1/2}$, Rydberg states with principal quantum number n close to 45 can be excited in a two-colour, two-photon process using a 780 nm and a 480 nm laser. In a magneto-optical trap, the 780 nm cooling and trapping laser is always on during our experiments, and the Rydberg state production can be completed by shining a 480 nm laser into the trap. Initially, a pulsed dye laser (with an output tunable between 470 nm and 490 nm) pumped by the third harmonic of a nanosecond pulsed YAG laser was used to provide the 480 nm light. This laser was used to excite $45d_{5/2}$ to study the resonant electric dipole-dipole interaction between cold Rydberg atoms [2]. One of the problems with using a multi-mode dye laser is its power and frequency fluctuations. Because of these fluctuations, the density of Rydberg atoms produced varies for different laser shots. Therefore, to have better control over the Rydberg density, an excitation source with better power and frequency stability is required.

In addition, the output bandwidth of the dye laser used was large (~ 20 GHz), resulting in the excitation to Rydberg states of a large number of hot rubidium atoms in the background of the MOT. The linewidth broadening of the microwave transitions arising from the collisions between hot and cold Rydberg atoms makes the effect of the resonant dipole-dipole interaction to look less prominent. To solve the problems associated with the excitation source, it was decided to use a more stable, narrower linewidth light source (a cw 480 nm light described in the next paragraph) for production of Rydberg atoms. The results of the two experiments for observation of resonant dipole-dipole interactions are compared later in this chapter.

The Rydberg state excitation scheme using a cw 480 nm laser was briefly explained in chapter 3, but now will be explained in greater detail. To make the 480 nm laser beam, the 960 nm output of a CW Ti:Sapphire (Coherent MBR-110) is frequency doubled in an external ring resonator (Coherent MBD 200). There are several atmospheric water absorption lines in the vicinity of 960 nm which restrict performance of the Ti:sapphire laser system. For instance, the Ti:sapphire laser is not stable at the wavelength required to excite $45d_{5/2}$ (a list of other wavelengths is given in Appendix B); therefore, to observe the resonant electric dipole-dipole interaction, we excite $46d_{5/2}$ Rydberg state of ^{85}Rb instead of $45d_{5/2}$ that was excited in the pulsed laser experiment [2]. In order to produce these Rydberg atoms, the vacuum MBD wavelength should be approximately 480.32 nm [3]. Roughly 10% efficiency was achieved in frequency doubling, resulting in an MBD output power of 90 mW from a 900 mW MBR power. The doubling efficiency and power stability of the MBD output power was dependent on room conditions such as temperature and humidity. In general, the CW laser works better when the room temperature is constant and the humidity is low. The experiment is done at a 10 Hz repetition rate; therefore, we need to make pulses of the 480 nm laser. To this end, the MBD output is sent through an acousto-optic modulator (AOM) whose driving power was pulsed by an arbitrary wave generator to produce pulses of CW light. The first-order diffracted output of the AOM is coupled into a single mode fibre whose output is collimated using two lenses in a telescopic configuration. A half-wave plate and a polarizing beam splitter (PBS) were used after the collimator to set the polarization of the 480 nm laser beam that was then focussed into the trap using a lens. The position of this lens was changed, relative to the trap, to change the laser spot size in the trap. A schematic of this laser beam collimating and focussing assembly is presented in chapter 6, where the Rydberg atom density measurement is explained. The spot size of the 480 nm laser around the tightest focus was characterized using the knife-edge scanning method. The number of excited cold Rydberg atoms was controlled by changing the excitation laser power. This power was varied using the AOM driver level. The maximum laser power at the output of the fibre was 25 mW. It is verified in chapter 5 that cold Rydberg atoms that are produced this way can be considered to be effectively stationary during the 8 μs time of the experiment.

4.4 Microwave transitions between Rydberg states

After production of $46d_{5/2}$ atoms by optical excitation, microwave radiation is used both to transfer these atoms to other Rydberg states, such as $46p_{3/2}$, $47p_{3/2}$, and $45f_{5/2,7/2}$, and to probe interatomic interactions by driving $46d_{5/2}-47d_{5/2}$ transition. To drive the $46d_{5/2}-47p_{3/2}$ (required frequency ≈ 22.1 GHz), and $46d_{5/2}-45f_{5/2,7/2}$ (required frequency ≈ 24.1 GHz) one-

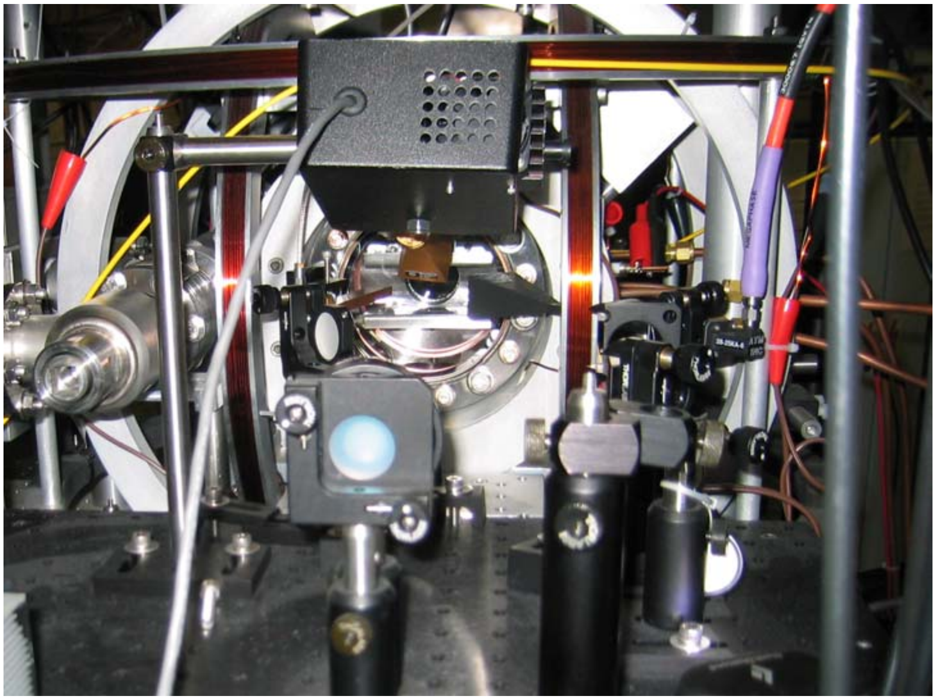

Figure 4-2: The magneto-optical trap used to produce cold Rb atoms. The horns shown in this picture were used to direct microwaves into the trap for Rydberg state manipulation.

photon transitions, the unamplified output of an Agilent E8254A microwave synthesizer was used. This microwave radiation is called the transfer pulse, and was $0.60\,\mu$s long. For a specific orientation and distance of the microwave horn relative to the trap (shown on Fig. 4-2), a microwave power of 0.1μW was used to transfer 50% of $46d_{5/2}$ atoms into the $47p_{3/2}$ state.

To probe the interactions between $46d_{5/2}$ and $47p_{3/2}$ atoms, we measure the linewidth broadening of the two-photon $46d_{5/2} - 47d_{5/2}$ probe transition. The rationale for using a two-photon transition as the probe is as follows. The large inhomogeneous magnetic field required for operation of the MOT in general broadens the spectral lines because of the Zeeman effect. The energy shifts due to this effect are given by $\Delta E = g_J \mu_B B M_J$, where μ_B is the Bohr magneton, M_J is the magnetic quantum number, B is the magnetic field, and g_J is the Landé factor which, ignoring the hyperfine structure at large magnetic fields, is given by [4]

$$g_J = \frac{J(J+1)+L(L+1)-S(S+1)}{2J(J+1)} + g_s\frac{J(J+1)-L(L+1)+S(S+1)}{2J(J+1)}, \tag{4.2}$$

and $g_s \approx 2$. Since g_J is normally different for the initial and final states of transitions, inhomogeneous magnetic fields broaden atomic transitions. However, for a two-photon transition g_J can be the same for the upper and lower states, because S, L, and J can be kept the same. Therefore, two-photon transitions with $\Delta M_J = 0$ are not broadened due to the Zeeman effect. This fact has been demonstrated for optical transitions [5], microwave transitions between Rydberg atoms in an atomic beam [6], and cold Rydberg atoms in a MOT [7]. Figure (4-3) compares one-photon and two-photon transitions in magnetic fields. Hence, the two-photon $46d_{5/2} - 47d_{5/2}$ transition can be used as a sensitive probe of interatomic interactions in a MOT.

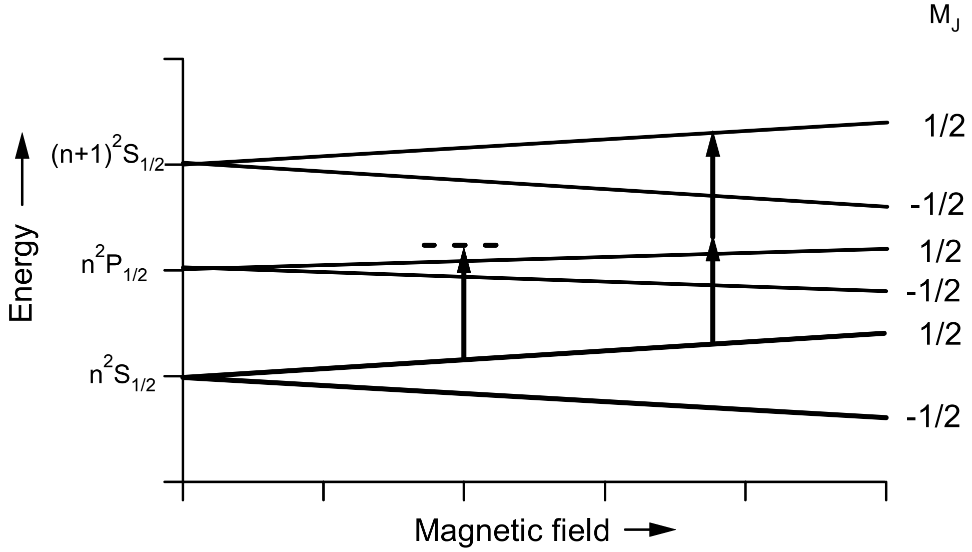

Figure 4-3: The effect of magnetic fields on one-photon and two-photon transitions.

The output of an Agilent E8254A microwave synthesizer was used to drive the probe transition, at a frequency of $\approx$ 35.7 GHz. The frequency of this probe transition is scanned between experiment shots and its linewidth is studied to measure interatomic interactions. In

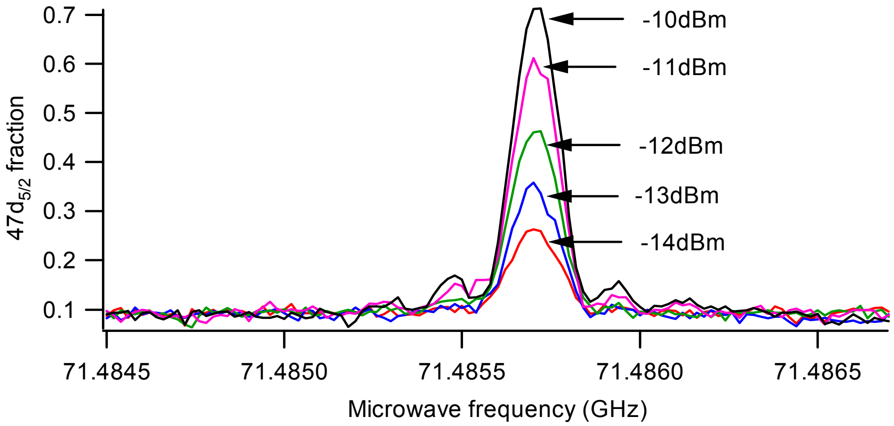

Figure 4-4: Microwave spectra for the two-photon $46d_{5/2} - 47d_{5/2}$ transition at different microwave power.

the absence of interatomic interactions, microwave spectra should have a $sinc^2(\pi f T)$ lineshape for a microwave square pulse of length T [8]. Figure (4-4) shows the microwave spectra for $46d_{5/2}-47d_{5/2}$ transition at different microwave powers. At high microwave powers, the spectra show power broadening. Since we are going to measure linewidth broadening due to interatomic interactions, we should eliminate other sources of line broadening. Therefore, to improve the sensitivity of our probe transition to dipole-dipole interactions, the microwave power should be set so that the power broadening is negligible. The microwave power used to drive the two-photon probe transition with a $6\,\mu$s pulse was approximately $60\,\mu$W. On the other hand, the linewidths of the probe transition at low microwave powers are dictated by the length of the microwave pulse. The transform-limited linewidth (ultimate linewidth due to the finite length of the pulse) for a square pulse is given by $5.6/(2\pi T)$, where T is the length of the pulse [8]. This ultimate linewidth for a $6\,\mu$s long pulse is 148 kHz. Introduction of the dipole-dipole interaction by production of $47p_{3/2}$ atoms will broaden the linewidth of the probe transition beyond the transform limit.

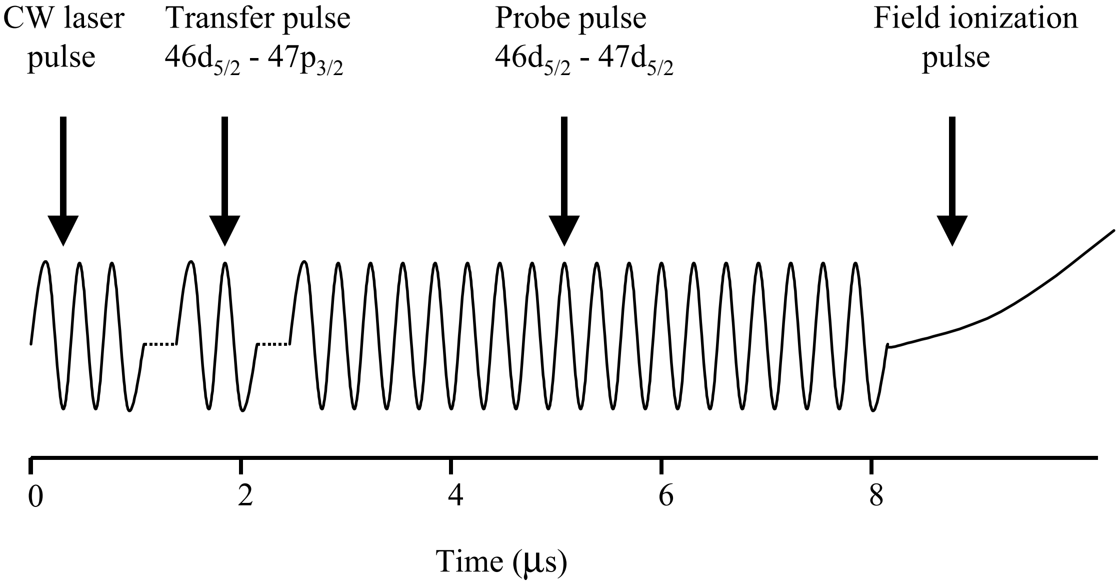

Figure 4-5: Timing of the resonant electric dipole-dipole experiment.

4.5 Observation of resonant electric dipole-dipole interaction

4.5.1 Timing of the experiment

The timing of the resonant electric dipole-dipole interaction experiment for a single shot is shown on figure (4-5). After the 1 μs-long optical excitation pulse that excites atoms to $46d_{5/2}$, a microwave pulse, 0.6 μs long, may transfer a fraction of these atoms to other Rydberg states, such as $47p_{3/2}$, $46p_{3/2}$, or $45f_{5/2,7/2}$ in this experiment. Then, a 6 μs-long microwave pulse drives the $46d_{5/2}-47d_{5/2}$ two-photon transition, whose linewidth is studied to probe interatomic interactions. The Rydberg state populations are detected at the end using the selective field ionization technique. Figure (4-6) shows the field ionization signal corresponding to a) $46d_{5/2}$ atoms, b) $46d_{5/2}$ and $47d_{5/2}$ atoms, and c) $46d_{5/2}$, $47d_{5/2}$,and $47p_{3/2}$ atoms. Since $46d_{5/2}$ and $47p_{3/2}$ states are indistinguishable in the field ionization technique, we verify production of $47p_{3/2}$ atoms by observing the reduction in the $47d_{5/2}$ signal.

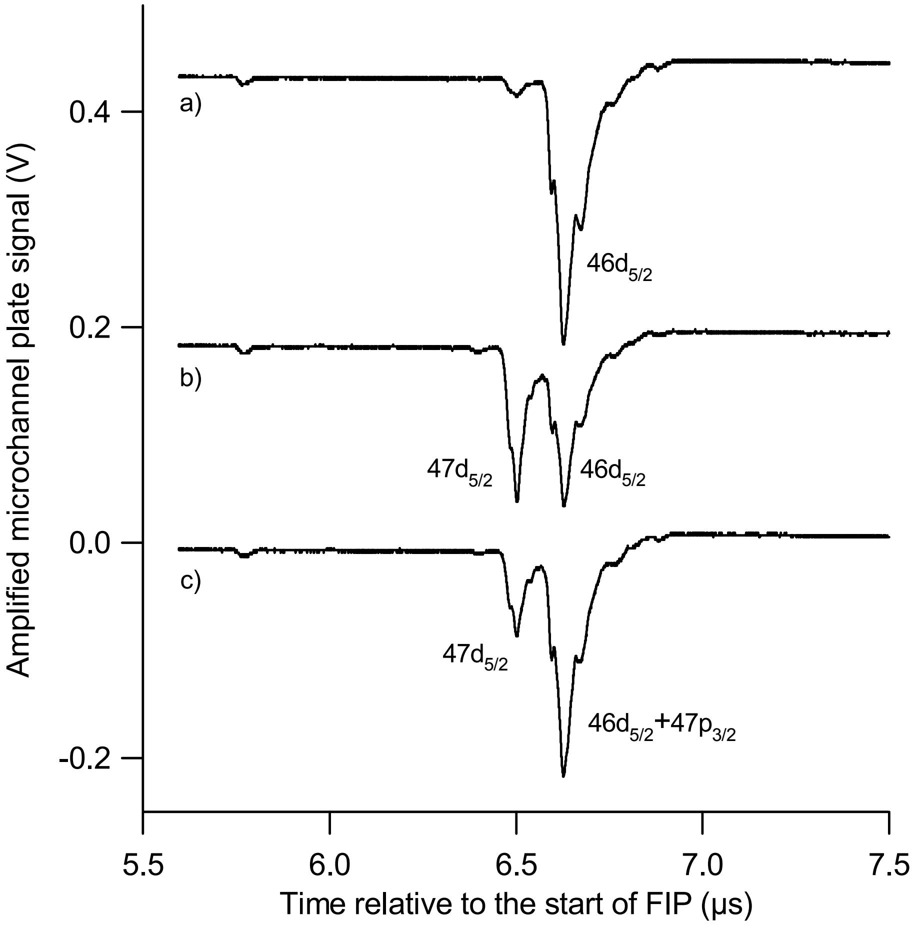

Figure 4-6: Field ionization signal for a) $46d_{5/2}$, b) $46d_{5/2}$ + $47d_{5/2}$, and c) $46d_{5/2}$ + $47p_{3/2}$ + $47d_{5/2}$. The zero of time is the start of field ionization pulse (FIP). Data are offset vertically for clarity.

4.5.2 Results and discussion

The experimental procedure for observation of resonant dipole-dipole interaction is as follows: after optically exciting $46d_{5/2}$, in one experiment, the two-photon probe transition is driven whose linewidth is measured as will be explained later. In the second experiment, $47p_{3/2}$ atoms are produced by transfer pulse before driving the probe transition. The microwave spectra for the two-photon $46d_{5/2} - 47d_{5/2}$ transition is given in Fig. (4-7-a) in the absence of $47p_{3/2}$ atoms, and in Fig. (4-7-b) when $47p_{3/2}$ atoms are produced. The power of the probe transition is adjusted so that the power broadening is negligible, and in the limit of low Rydberg densities, the transition linewidths are entirely due to the transform broadening. As it is shown on Fig. (4-7), production of $47p_{3/2}$ atoms broadens the linewidth of the two-photon probe transition.

The dipole-dipole interaction between two atoms is given by Eq. 4.1. According to Fig. 4-1, the magnitude of the electric dipole matrix element $\langle nl_j|r|n\acute{l}_{\acute{j}}\rangle$ is large between the $46d_{5/2}$ and $47p_{3/2}$ states; therefore, these states are strongly coupled by resonant dipole-dipole interaction, whereas the $47d_{5/2}$ and $47p_{3/2}$ states are not. Hence, only the initial state of the two-photon probe transition is split by the resonant dipole-dipole interaction with $47p_{3/2}$ atoms. As will be explained, the linewidth broadening in Fig. (4-7-b) is due to this resonant dipole-dipole interaction. To analyze interatomic interactions, microwave spectra are fit to the transform limited lineshape for a square pulse , $\text{sinc}^2(\pi fT)$, convolved with a Lorentzian of variable linewidth $\delta\nu$ adjusted to give the best least-squares fit to individual spectra. A theoretical model of the resonant dipole-dipole interaction, explained in chapter 5, results in lineshapes with Lorentzian tails.

Because of the dependence of V_{dd} in Eq. 4.1 on the interatomic separations ($1/R^3$ dependence), the linewidth broadening of the two-photon probe transition should depend linearly on the average density of Rydberg atoms. For a spatially averaged Rydberg density of $1\times10^7\text{cm}^{-3}$, for example, the linewidth broadening $\delta\nu$ increases from approximately $10\pm5\,\text{kHz}$ to $120\pm10\,\text{kHz}$. Measurement of Rydberg state densities is presented in chapter 6. Figure (4-8) shows the linewidth broadening of the two-photon $46d_{5/2} - 47d_{5/2}$ transition as a function of the spatially averaged Rydberg density, with and without production of $47p_{3/2}$ atoms. The $\delta\nu$ in the two cases converge in the limit of low Rydberg densities which shows that the broadening effect is due to interatomic interactions. According to Fig. (4-1), only the initial state of the probe transition is coupled with $47p_{3/2}$ state through resonant electric dipole-dipole interaction; therefore, the broadening effect is due to the interaction of $46d_{5/2}$ and $47p_{3/2}$ atoms.

Figure (4-1) shows strong coupling between $46d_{5/2}$ and $45f$ states, and poor coupling between $46d_{5/2}$ and $46p_{3/2}$ states. This suggests two tests of our understanding; transition broadening due to resonant electric dipole-dipole interaction is expected to be observed if $45f$ states are excited instead of $47p_{3/2}$, and no broadening is anticipated if $46p_{3/2}$ states are excited. In the first experiment, an active quadrupler (Spacek Labs P/N A100-4XW) is driven by an Agilent E8254A synthesizer to produce the required frequency of $\approx 100.1\,\text{GHz}$ to drive $46d_{5/2} - 46p_{3/2}$ one-photon transition. The length of this transfer pulse was $0.6\,\mu$s, same as before, and the power input to the active quadrupler was -15dBm. In this situation, as shown in Fig. (4-9), the linewidths of the two-photon probe transition when the transfer pulse is on or off, are experimentally indistinguishable, confirming that the resonant electric dipole-dipole interaction between $46d_{5/2}$ and $46p_{3/2}$ states is weak. On the other hand, transferring a fraction of $46d_{5/2}$ atoms to $45f_{5/2,7/2}$ state introduces interatomic interactions, and as Fig. (4-9) demonstrates, linewidth broadening is observed for the probe transition. The $46d_{5/2} - 45f_{5/2,7/2}$ one-photon transition is driven using the output of an Agilent E8254A microwave synthesizer, and a microwave power of $100\,\mu$W is needed to transfer 30% of atoms to $45f_{5/2,7/2}$ state. These tests confirm that the linewidth broadening observed in Figs. (4-8) and (4-9) are due to resonant electric dipole-dipole interactions.

One issue is the fact that we almost always observe some linewidth broadening when p atoms are not produced. There could be different interactions responsible for this linewidth broadening such as collisions with hot Rydberg atoms, interactions with cold less excited ($5p_{3/2}$) atoms, and collisions with particles emitted from the Rb dispenser. Several tests have confirmed that this line broadening arises from collisions with hot Rydberg atoms.

The 480 nm excitation laser can produce both cold Rydberg atoms from laser cooled and trapped atoms, and hot Rydberg atoms from the hot Rb atoms in the background of the trap. If collisions with these hot Rydberg atoms are responsible for the slope of "no transfer" line in Fig. (4-8) and Fig. (4-9), reducing the number of these atoms should lower this slope. To check this, the current of the Rb dispenser is lowered to reduce the number of hot Rb atoms. If the power of the excitation laser and the number of cold atoms in the trap are kept constant

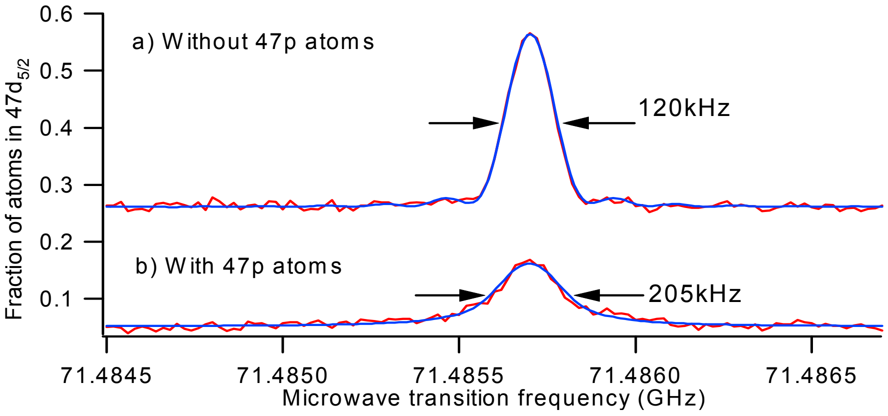

Figure 4-7: The two-photon microwave probe transition with and without production of $47p_{3/2}$ atoms. The overall linewidth increases from 120 kHz to 205 kHz when $47p_{3/2}$ atoms are produced.

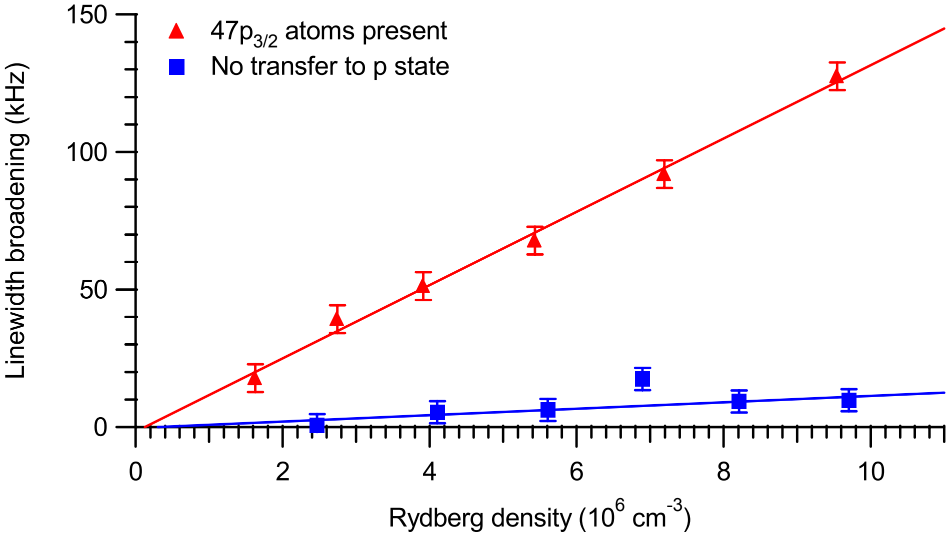

Figure 4-8: Linewidth broadening of the two-photon $46d_{5/2} - 47d_{5/2}$ probe transition with and without production of $47p_{3/2}$ atoms. The errors on the linewidths are roughly 7 kHz, and come from uncertainty in fitting the data.

(by changing the detuning of the cooling and trapping laser), less hot Rydberg atoms will be excited, but the number of cold Rydberg atoms will stay the same in this case. Figure (4-10) shows that the linewidth broadening is indeed lower when less hot Rydberg atoms are created. Therefore, collisions with hot Rydberg atoms produce linewidth broadening when p atoms are not excited.

To check the effect of cold $5p_{3/2}$ atoms, we change the cooling and trapping laser detuning to reduce the number of these atoms keeping the Rydberg density constant by increasing the excitation laser power. If collisions with less excited $5p_{3/2}$ atoms has an effect, we should observe less linewidth broadening; however, no reduction in broadening was detected, ruling out the effect of less excited cold atoms.

The effect of particles coming off the Rb dispenser on the linewidth of the two-photon probe transition should be studied, because the number of these particles will change when the dispenser current is varied. The number of particles emitted from the dispenser should change immediately when the current of the Rb dispenser is changed, but it takes some time for the number of background atoms to change. Therefore, if the linewidth of the two-photon transition is studied before and immediately after changing the dispenser current, keeping all other conditions the same, any observed change in the linewidth should be attributed to collisions with the particles from the dispenser. This experiment was done, and the results showed that these collisions do not have any observable effect on the transition linewidths.

4.6 Magnetic field effect

It was shown in the previous section that the linewidths of microwave transitions between cold Rydberg states are broadened because of the resonant electric dipole-dipole interaction when one of the states involved in the transition resonantly interacts with another state. So far, we have assumed that there is no magnetic field in the experimental region, and therefore that all the magnetic sublevels of any atomic state are energy degenerate. This degeneracy is responsible for the strength of the resonant electric dipole-dipole interaction between Rydberg atoms. With an external magnetic field, however, the degeneracy of the magnetic sublevels is removed, and atoms in different magnetic sublevels have different energies. As a result, a two-atom state

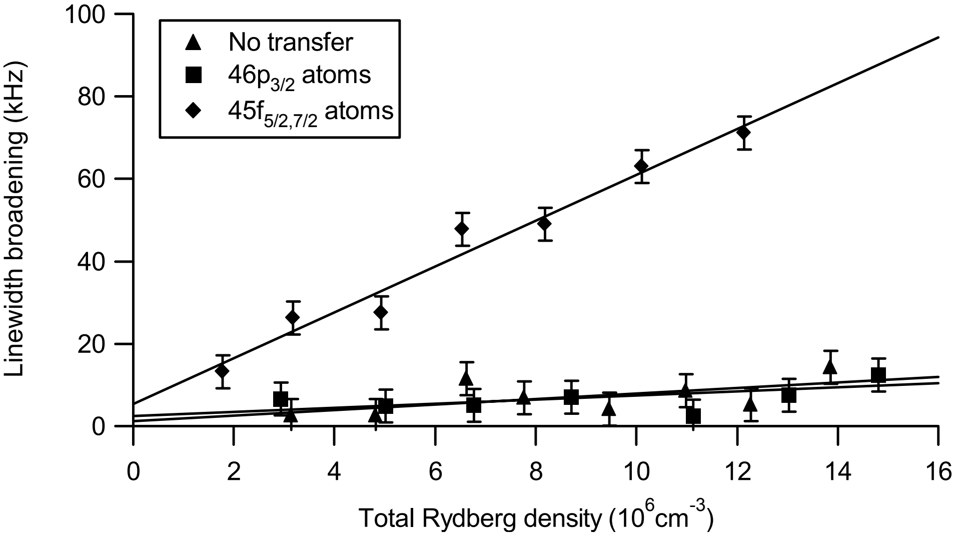

Figure 4-9: Production of $46p_{3/2}$ atoms instead of $47p_{3/2}$ does not show transition broadening due to resonant electric dipole-dipole interaction, and is experimentally indistinguishable from the case when no p atoms are produced. Production of $45f$ atoms, on the other hand, does show broadening.

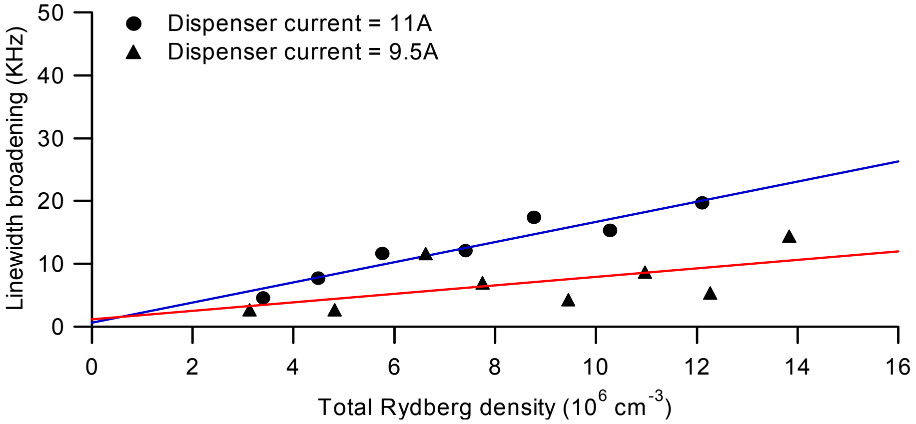

Figure 4-10: Comparison of the linewidth broadening of the two-photon probe transition in the absence of p atoms at two different densities of hot Rydberg atoms shows that collisions with these atoms are the reason for this broadening.

of $|46d_{5/2}, m_{jA1}\rangle_A|47p_{3./2}, m_{jB1}\rangle_B$ can resonantly interact with $|47p_{3/2}, m_{jA2}\rangle_A|46d_{5/2}, m_{jB2}\rangle_B$ only if $m_{jA1} = m_{jB2}$ and $m_{jB1} = m_{jA2}$. This means that the external magnetic field spoils part of the degeneracy that is responsible for the strength of the resonant electric dipole-dipole interaction, and suppression of this interaction is expected when a magnetic field is applied. In this section, the result of the experiment when a DC magnetic field is applied is discussed.

To study the effect of external magnetic fields on linewidth broadening due to interatomic interactions, a calibrated DC magnetic field is applied (by changing the current of a pair of compensating coils) while doing the experiment. The timing sequence of the experiment is the same as before, only this time the anti-Helmholtz coils are switched off 25 ms before doing the experiment. Our method of measuring magnetic fields, together with the reasons for switching off the quadrupole field are explained in chapter 3. Figure (4-11) shows the microwave spectra corresponding to the two-photon probe transition at the presence of $47p_{3/2}$ atoms with and without the application of an external magnetic field; when a magnetic field of $0.47 \pm 0.005\,\mathrm{G}$ is applied the linewidth broadening due to interatomic interactions is reduced by roughly $60{\pm}5\,\mathrm{kHz}$ at a Rydberg atom density of $1 \times 10^7 \mathrm{cm}^{-3}$. The suppression of the resonant dipole-dipole interaction by external magnetic fields is also clear in Fig. (4-12), in which the measured linewidth broadening of the probe transition is shown at different applied magnetic fields for two different Rydberg densities. These results are compared with those obtained from a theoretical model in chapter 5.

As was explained in chapter 3, the stray magnetic field should be nulled out so that the zero of the inhomogeneous magnetic field lies at the center of the AHCs. This keeps the zero of the magnetic field in the same place when the AHCs are switched off, and prevents the cold atoms from being pushed off to one side. In this situation, when a DC magnetic field is deliberately applied, the zero of the quadrupole magnetic field is shifted and so is the trap location. For the DC magnetic fields less than $0.6\,\mathrm{G}$ used in these experiments, the shift of the zero of the quadrupole field is small enough that it stays at the intersection of the trap lasers, and we still have a reasonable trap. This said, the trap position is slightly different for different DC magnetic fields. This causes different expansion of the trap and consequently different average Rydberg density when AHCc are switched off. To solve this problem, the alignment and the relative power of the counterpropagating MOT beams were adjusted for each applied magnetic field, so

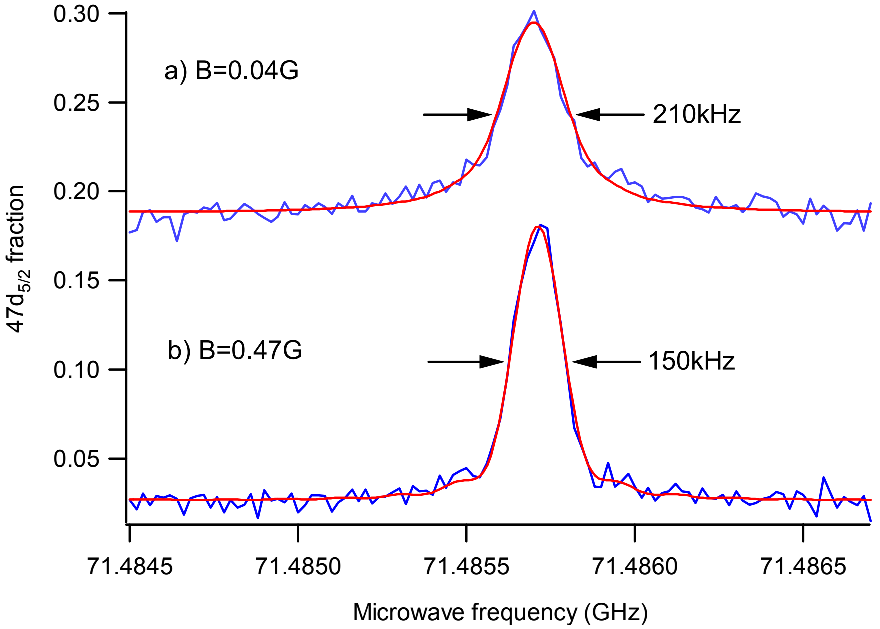

Figure 4-11: Magnetic field suppresses the resonant dipole-dipole line broadening; in this figure, application of a DC magnetic field of 0.47 G reduces the overal linewidth of the probe transition from 210 kHz to 150 kHz.

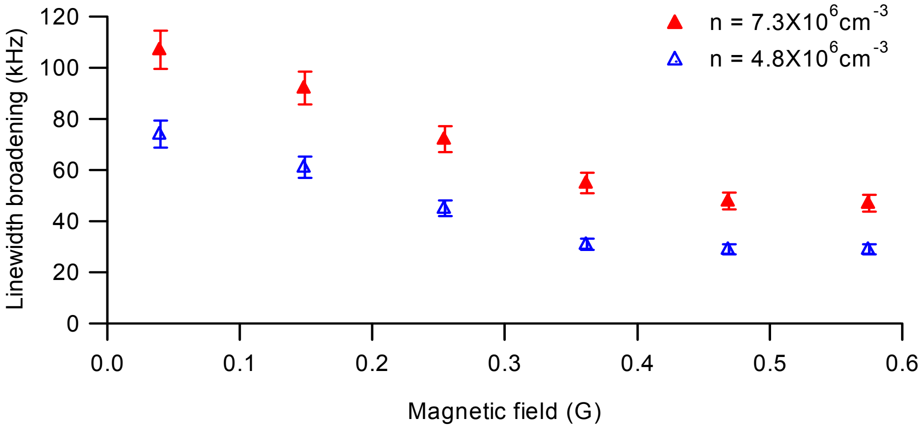

Figure 4-12: Suppression of the resonant electric dipole-dipole interaction by external magnetic fields for two different Rydberg atom densities of $7.3 \times 10^6\,\mathrm{cm}^{-3}$ and $4.8 \times 10^6\,\mathrm{cm}^{-3}$.

that at a fixed excitation laser power, a constant average Rydberg density is maintained for each set of data in Fig. (4-12). This is verified by keeping a constant selective field ionization signal corresponding to the $46d_{5/2}$ Rydberg state. Figure (4-13) shows two spectra corresponding to the lowest and highest magnetic fields applied in Fig. (4-12) for the Rydberg atom density of $n = 7.3 \times 10^6\,\mathrm{cm}^{-3}$. The similarity of the baselines and the signal levels on this graph confirms a constant density. The results of the experiments presented in this chapter are published in Ref. [9].

4.7 Conclusion

The resonant electric dipole-dipole interaction between cold Rydberg atoms has been observed using microwave spectroscopy. This is a step towards the realization of “dipole blockade” which was proposed by Lukin *et al.* [10]. The magnetic field induced partial suppression of the resonant electric dipole-dipole interaction has also been presented. Theoretical models that predict similar effects will be presented in the next chapter.

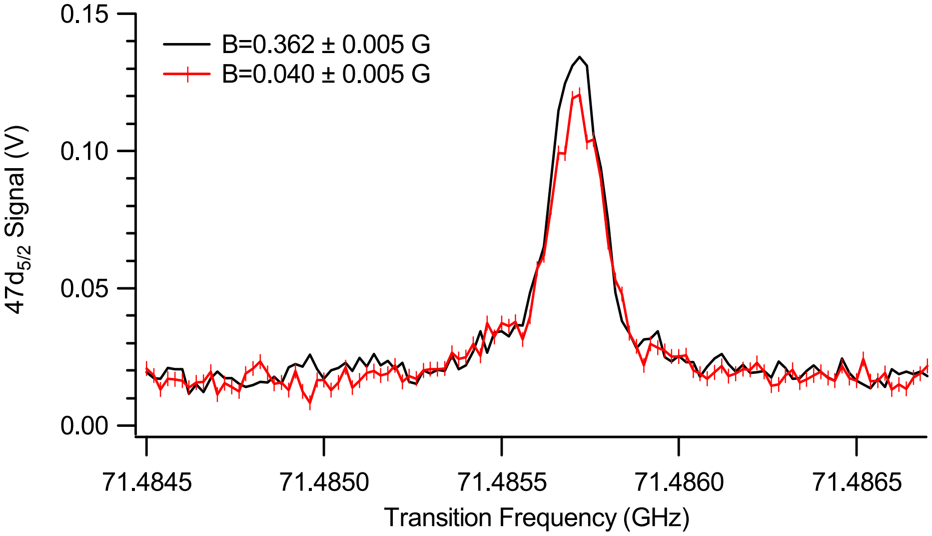

Figure 4-13: The microwave spectra for the two-photon probe transition for two different magnetic fields of 0.040 G and 0.362 G and a Rydberg density of $7.3 \times 10^6\,\mathrm{cm}^{-3}$.

Bibliography

[1] M. L. Zimmerman, M. G. Littman, M. M. Kash, and D. Kleppner, "*Stark structure of the Rydberg states of alkali-metal atoms*", Phys. Rev. A **20**, 2251 (1979).

[2] K. Afrousheh, P. Bohlouli-Zanjani, D. Vagale, A. Mugford, M. Fedorov, J. D. D. Martin, " *Spectroscopic observation of resonant electric dipole-dipole interactions between cold Rydberg atoms*", Phys. Rev. Lett. **93**, 233001 (2004).

[3] NIST web-site on atomic spectra database: http://physics.nist.gov/cgi-bin/AtData/main_asd.

[4] G. Kuhn, "*Atomic Spectra"*, Longmans, first edition, 1962.

[5] N. Bloembergen, M. D. Levenson, and M. M. Salour, "*Zeeman effect in the two-photon 3s-5s transition in sodium vapor*", Phys. Rev. Lett. **32**, 867 (1974).

[6] P. Goy, C. Fabre. M. Gross. and S. Haroche, "*High-resolution two-photon millimeter spectroscopy in sodium Rydberg states: possible applications to metrology*", J. Phys. B **13**, L83 (1980).

[7] W. Li, I. Mourachko, M.W. Noel, and T. F. Gallagher, "*Millimeter-wave spectroscopy of cold Rb Rydberg atoms in a magneto-optical trap: Quantum defects of the ns, np, and nd series*", Phys. Rev. A **67**, 052502 (2003).

[8] W. Demtroder, "*Laser Spectroscopy"*, Springer, Third edition (2003).

[9] K. Afrousheh, P. Bohlouli-Zanjani, J. Carter, A. Mugford, and J. D. D. Martin, "*Resonant electric dipole-dipole interactions between cold Rydberg atoms in a magnetic field*", Phys. Rev. A. **73**, 063403 (2006).

[10] M. D. Lukin, M. Fleischhauer, and R. Cote, "*Dipole Blockade and quantum information processing in mesoscopic atomic ensembles*", Phys. Rev. Lett. **87**, 037901 (2001).

Chapter 5

Theoretical Models of The Line Broadening Due To The Resonant Electric Dipole-Dipole Interaction

5.1 Introduction

In this chapter a theoretical model will be presented which estimates the line broadening due to the resonant electric dipole-dipole interaction both with and without the application of a homogeneous magnetic field. Initially, the motion of the cold Rydberg atoms during the timescale of the experiments is estimated, verifying the assumption of dealing with stationary atoms. In the following sections, estimates of the line broadening due to resonant electric dipole-dipole interactions, and the suppression of this interaction by a DC magnetic field are presented.

5.2 Motion of cold Rydberg atoms

In the simulations, it is assumed that cold Rydberg atoms are effectively stationary during the experiment period. This can be checked by estimating the motion of cold Rydberg atoms during each experiment. Assuming the cold Rydberg atoms to be a classical gas, their speed and temperature are related according to $(1/2)mv^2 = (3/2)kT$, where m is the mass of Rb,

v is its speed, k is the Boltzman constant, and T is temperature. For ^{85}Rb, $m = 84.912$ amu$\simeq 1.4 \times 10^{-25}$ kg (1 amu$= 1.66053886 \times 10^{-27}$ kg); therefore, assuming a typical MOT temperature of $T = 300\mu$K, we get $v \simeq 0.3$ m/s. Each experiment is done in approximately $8\,\mu$s, and during this time, cold Rydberg atoms move for $x \simeq 2.4\,\mu$m. For an average cold Rydberg atom density of $n = 5 \times 10^6$cm^{-3}, using $R = (4\pi n/3)^{-1/3}$, the average interatomic separation is $R \simeq 35\,\mu$m; therefore, because of their thermal energy, cold Rydberg atoms on average move by only 7% of their separation over the $8\,\mu$s experiment time.

When excited to Rydberg states, cold atoms experience a force due to the dipole-dipole interaction and accelerate towards one another [1]. This force, which is the gradient of the dipole-dipole interaction potential, is given by $F = |\nabla V_{dd}| \simeq 3\mu^2/R^4$, where μ is the electric dipole moment, and R is the interatomic separation. For two atoms in the $46d_{5/2}$ and $47p_{3/2}$ states, μ can be calculated using

$$\mu = \left|\langle 46d_{5/2,1/2}|\mu_z|47p_{3/2,1/2}\rangle\right|, \tag{5.1}$$

which gives $\mu = 1268$. Assuming cold atoms to be $35\,\mu$m apart, or $R = 6.614 \times 10^5 a_0 = 6.614 \times 10^5$a.u., where $a_0 = 5.2918 \times 10^{-11}$ m is the Bohr radius, we get $F = 2.52 \times 10^{-17}$a.u. The acceleration of Rydberg atoms due to this force is $a = F/m = 2.969 \times 10^{-19}$a.u.$= 3.4 \times 10^4$ m/s^2, using 1a.u.$= 2.4189 \times 10^{-17}$ s, and $a_0 =$ 1a.u.$= 5.2918 \times 10^{-11}$ m, to convert a.u. to m/s^2. As a result of this acceleration, Rydberg atoms move by $3.5\,\mu$m during $8\,\mu$s; therefore, interatomic distance changes by only 10% because of the dipole-dipole interaction force. Since the separation of Rydberg atoms does not change appreciably during the experiment period, one can assume that they are stationary in this time.

5.3 Simulation of the line broadening due to resonant electric dipole-dipole interactions

To obtain estimates of the line broadening, we consider interactions between pairs of atoms (A and B) due to the electric dipole-dipole interaction operator:

$$\hat{\mathrm{V}}_{dd} = \frac{\overrightarrow{\mu}_A \cdot \overrightarrow{\mu}_B - 3(\overrightarrow{\mu}_A \cdot \hat{n})(\overrightarrow{\mu}_B \cdot \hat{n})}{R_{AB}^3}, \tag{5.2}$$

where $\overrightarrow{\mu}_A$ and $\overrightarrow{\mu}_B$ are the electric dipole matrix element operators evaluated on each atom, $\hat{n}$ is the unit vector pointing between the atoms, and R_{AB} is the separation of the two atoms. In the absence of magnetic fields, this perturbation may split the otherwise energy degenerate states $|1\rangle = \left|46d_{5/2}m_{j,A1}\right\rangle_A \left|47p_{3/2}m_{j,B1}\right\rangle_B$ and $|2\rangle = \left|47p_{3/2}m_{j,A2}\right\rangle_A \left|46d_{5/2}m_{j,B2}\right\rangle_B$. A rough estimation of the resonant dipole-dipole line broadening was presented in Ch. 4 using $\Delta v_{dd} \approx \mu^2/R^3$ as an approximation. There we used a fixed interatomic separation, and neglected different orientations of dipole moments relative to one another.

To make a better estimate of the line broadening due to the resonant electric dipole-dipole interactions, one should account for the orientations of the dipole and $\hat{n}$ operators and the distribution in interacting atoms separations. Also, different possibilities for the distribution of atoms over different magnetic sublevels should be considered. In the absence of magnetic fields, all the different magnetic sublevels of the two-atom states $|1\rangle = \left|46d_{5/2}m_{j,A1}\right\rangle_A \left|47p_{3/2}m_{j,B1}\right\rangle_B$ and $|2\rangle = \left|47p_{3/2}m_{j,A2}\right\rangle_A \left|46d_{5/2}m_{j,B2}\right\rangle_B$ are energy degenerate; therefore, all the atoms in $46d_{5/2}$ state can resonantly interact with those in $47p_{3/2}$ state. However, in the presence of a magnetic field, different magnetic sublevels experience different Zeeman shifts; therefore, only pairs of states for which $m_{jA1} = m_{jB2}$ and $m_{jB1} = m_{jA2}$ are energy degenerate. For example, in the presence of a magnetic field, the $|1\rangle = \left|46d_{5/2}, m_j = -3/2\right\rangle_A \left|47p_{3/2}, m_j = -1/2\right\rangle_B$ state of the two-atom system can resonantly interact only with $|2\rangle = \left|47\mathrm{p}_{3/2}\mathrm{m}_j\text{=-}1/2\right\rangle_A \left|46\mathrm{d}_{5/2}\mathrm{m}_j\text{=-}3/2\right\rangle_B$ state. On the other hand, in the absence of magnetic fields, the $|1\rangle$ state is also coupled to other states such as $|2\rangle = \left|47p_{3/2}m_j = -3/2\right\rangle_A \left|46d_{5/2}m_j = -1/2\right\rangle_B$ through the resonant dipole-dipole interaction. The reduction in the number of interacting states results in a decrease in the strength of the resonant dipole-dipole interaction. In this section it is assumed that there is no magnetic field applied to the interacting atoms; the effect of an applied magnetic field on linewidths will be discussed in the next section.

In order to calculate the linewidth broadening due to the dipole-dipole interaction, the matrix elements $\left\langle 1 \left| \hat{\mathrm{V}}_{dd} \right| 2 \right\rangle$should be computed in which $|1\rangle$ and $|2\rangle$ were defined in the previous paragraph, and $\hat{\mathrm{V}}_{dd}$ is given by Eq. 5.2. To do this calculation, we need to know the magnetic quantum number m_j of the interacting atoms. Due to the presence of the quadrupole magnetic field required for the operation of the MOT, different atoms experience different magnetic fields and might be in different magnetic sublevels. Without a detailed knowledge of the distribution of atoms over magnetic sublevels, two cases can be considered in our calculation: 1) all atoms are in the same magnetic sublevel, and 2) atoms are randomly distributed over different magnetic sublevels.

5.3.1 Case 1: similar magnetic sublevels

In the first case, it is assumed that the common magnetic sublevel is $m_j = 1/2$; therefore, for these calculations we have

$$|1\rangle = \left|46d_{5/2}, 1/2\right\rangle_A \left|47p_{3/2}, 1/2\right\rangle_B ,$$

$$|2\rangle = \left|47p_{3/2}, 1/2\right\rangle_A \left|46d_{5/2}, 1/2\right\rangle_B . \tag{5.3}$$

The single atom states may be transformed from j, m_j representation to m_l, m_s representation using [2]

$$|n, l, j, m_j\rangle = \sum_{m_l, m_s} |n, l, m_l, m_s\rangle \langle l, s, m_l, m_s | l, s, j, m_j\rangle , \tag{5.4}$$

where $\langle l, s, m_l, m_s | l, s, j, m_j\rangle$ are Clebsch-Gordan coefficients. Therefore, $\left|46d_{5/2}, m_j = 1/2\right\rangle$ and $\left|47p_{3/2}, m_j = 1/2\right\rangle$ can be written as

$$\begin{aligned} \left|46d_{5/2}, m_j = 1/2\right\rangle &= |46, 2, 0, 1/2\rangle \langle 2, 1/2, 0, 1/2 | 2, 1/2, 5/2, 1/2\rangle \\ &\quad + |46, 2, 1, -1/2\rangle \langle 2, 1/2, 1, -1/2 | 2, 1/2, 5/2, 1/2\rangle , \end{aligned} \tag{5.5}$$

$$\begin{aligned} \left|47p_{3/2}, m_j = 1/2\right\rangle &= |47, 1, 0, 1/2\rangle \langle 1, 1/2, 0, 1/2 | 1, 1/2, 3/2, 1/2\rangle \\ &\quad + |47, 1, 1, -1/2\rangle \langle 1, 1/2, 1, -1/2 | 1, 1/2, 3/2, 1/2\rangle . \end{aligned} \tag{5.6}$$

The Clebsch-Gordan coefficients for the case of $s = 1/2$, and $m_s = \pm 1/2$ are given by (note that $j = l \pm 1/2$, and $m_l = m_j \pm 1/2$)

$$\langle l, 1/2, m_j - 1/2, 1/2 | l, 1/2, l + 1/2, m_j \rangle = \left[\frac{l + m_j + 1/2}{2l+1} \right]^{1/2},$$

$$\langle l, 1/2, m_j - 1/2, 1/2 | l, 1/2, l - 1/2, m_j \rangle = \left[\frac{l - m_j + 1/2}{2l+1} \right]^{1/2},$$

$$\langle l, 1/2, m_j + 1/2, -1/2 | l, 1/2, l + 1/2, m_j \rangle = \left[\frac{l - m_j + 1/2}{2l+1} \right]^{1/2},$$

$$\langle l, 1/2, m_j + 1/2, -1/2 | l, 1/2, l - 1/2, m_j \rangle = \left[\frac{l + m_j + 1/2}{2l+1} \right]^{1/2}. \tag{5.7}$$

The dipole moment operators may be expanded in Cartesian coordinates as $\overrightarrow{\mu} = \mu_x \hat{\imath} + \mu_y \hat{\jmath} + \mu_z \hat{k}$, where the three orthogonal components are written as: $\mu_x = r sin\theta sin\varphi$, $\mu_y = r sin\theta cos\varphi$, and $\mu_z = r cos\theta$. These components can also be expressed in spherical harmonics as:

$$\mu_x = \sqrt{\frac{2\pi}{3}} (Y_{1,-1} - Y_{1,1}) r,$$

$$\mu_y = i\sqrt{\frac{2\pi}{3}} (Y_{1,-1} + Y_{1,1}) r,$$

$$\mu_z = \sqrt{\frac{4\pi}{3}} Y_{1,0} r. \tag{5.8}$$

Using Eqs 5.5, 5.6, and 5.8, one can verify that for states $|1\rangle$ and $|2\rangle$ given in Eq. 5.3: $\langle 1 |\mu_x| 2 \rangle = \langle 1 |\mu_y| 2 \rangle = 0$, since $\langle l, m_l = 1 |Y_{1,\pm1}| l, m_l = 1 \rangle = \langle l, m_l = 0 |Y_{1,\pm1}| l, m_l = 0 \rangle = 0$, and we only need to keep μ_z in our calculations. Therefore, Eq. 5.2 in this case can be written as

$$\hat{V}_{dd} = \frac{\mu_z^2 (1 - 3n_z^2)}{R_{AB}^3}. \tag{5.9}$$

To calculate the value of $\left| \hat{\mathrm{V}}_{dd} \right|$ for a given R_{AB} and $\hat{n}$, we need to determine $\langle 1 |\mu_z| 2 \rangle$, where $|1\rangle$ and $|2\rangle$ are the two states given in Eq. 5.3. This can be written as

$$\langle 1 \left| \mu_z \right| 2 \rangle = \langle l_1 m_{l1} \left| \cos\theta \right| l_2 m_{l2} \rangle \langle n_1 l_1 \left| r \right| n_2 l_2 \rangle , \tag{5.10}$$

where r is the radial coordinate of the Rydberg electron. For this particular case, the angular part of the dipole moment operator $\langle \cos\theta \rangle$ is given by

$$\begin{aligned} \langle l_1 m_{l1} \left| \cos\theta \right| l_2 m_{l2} \rangle &= \sqrt{\frac{4\pi}{3}} (\langle l=2, m_l=0 \left| Y_{1,0} \right| l=1, m_l=0 \rangle \\ &\quad + \langle l=2, m_l=1 \left| Y_{1,0} \right| l=1, m_l=1 \rangle). \end{aligned} \tag{5.11}$$

The two terms inside brackets can be calculated using spherical harmonics, resulting in $\langle l_1 m_{l1} | \cos\theta | l_2 m_{l2} \rangle = 0.490$. The radial part of the dipole moment operator $\left\langle nl \left| r \right| n\acute{l} \right\rangle$ is obtained from integrating the radial part of the Rydberg electron wavefunction [3]. For the two states involved, this gives: $\left\langle 46d_{5/2} \left| r \right| 47p_{3/2} \right\rangle = 2700$ in atomic units [4].

To account for random distributions of atoms in the sample, the interatomic separation R_{AB} is chosen using the nearest neighbor probability distribution given by [5]:

$$\frac{dP(R_{AB})}{dR_{AB}} = 4\pi R_{AB}^2 n_{47p_{3/2}} \exp\left(-\frac{4\pi}{3} R_{AB}^3 n_{47p_{3/2}} \right) , \tag{5.12}$$

where $n_{47p_{3/2}}$ is the density of $47p_{3/2}$ atoms, as half of the atoms are in $47p_{3/2}$ and interact with the other half in $46d_{5/2}$. Here, we only consider interactions between pairs of atoms, and neglect multi-body interactions. Also, unit vectors $\hat{n}$ is chosen randomly so that we have spherically uniform distributions of atoms for a fixed R_{AB}. The value of $\left\langle 1 \middle| \hat{\mathrm{V}}_{dd} \middle| 2 \right\rangle$ is then calculated for each R_{AB} and $\hat{n}$ picked as above. This process is repeated numerous times to get a distribution for the resonant dipole-dipole interaction energy $\hat{\mathrm{V}}_{dd}$. This distribution is histogrammed and is shown in Fig. 5-1. In the spectra presented in the previous chapter for resonant dipole-dipole line broadening, the ultimate transition linewidth was dictated by the finite length of the probe microwave. This finite pulse length results in a $\mathrm{sinc}^2(\pi f T)$ lineshape [6], where $T = 6\,\mu$s. Therefore, to compare the linewidth broadening with experimental data, the calculated distribution is convolved with a $\mathrm{sinc}^2(\pi f T)$ lineshape, and fitted using a $\mathrm{sinc}^2(\pi f T)$ lineshape convolved with a Lorentzian of adjustable width $\delta\nu$, see Fig. 5-2. The linewidth broadening

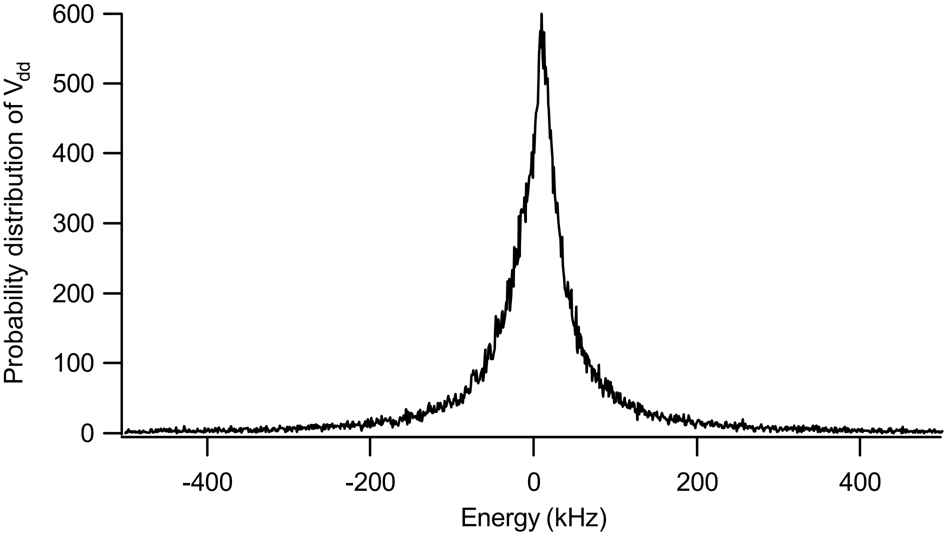

Figure 5-1: The distribution of the resonant dipole-dipole interaction energies for the case of $m_{jA} = m_{jB} = 1/2$, and a total Rydberg density of $10^7\,\mathrm{cm}^{-3}$.

obtained from this calculation for a $47p_{3/2}$ density of $5 \times 10^6\,\mathrm{cm}^{-3}$ (corresponding to a total Rydberg density of $10^7\,\mathrm{cm}^{-3}$) was $\delta\nu = 69\,\mathrm{kHz}$.

5.3.2 Case 2: atoms distributed over magnetic sublevels

In the second case, when atoms are randomly distributed between different magnetic sublevels, some pairs of atoms are not coupled by the resonant dipole-dipole interaction. For example, an atom A with $m_j = 3/2$ does not resonantly interact with an atom B with $m_j = -1/2$. In this case, only those states that satisfy $m_{jA_1} = m_{jB_2}$ and $m_{jA_2} = m_{jB_1}$ are exactly degenerate and are coupled by the resonant dipole-dipole interaction. To calculate the linewidth broadening due to the resonant electric dipole-dipole interaction, the above calculation is repeated when m_{jA} and m_{jB} are chosen randomly from different possibilities for $j_A = 5/2$ and $j_B = 3/2$. With this selection, $\left\langle 1 \middle| \hat{\mathrm{V}}_{dd} \middle| 2 \right\rangle$ is zero 50% of the time. This means that the strength of the resonant dipole-dipole interaction is reduced, and we expect to observe less linewidth broadening in this case. The distribution of the resonant interaction energies was obtained in the same way as above, and so was the linewidth broadening $\delta\nu$. This results in a resonant dipole-dipole line broadening of $\delta\nu = 23\,\mathrm{kHz}$.

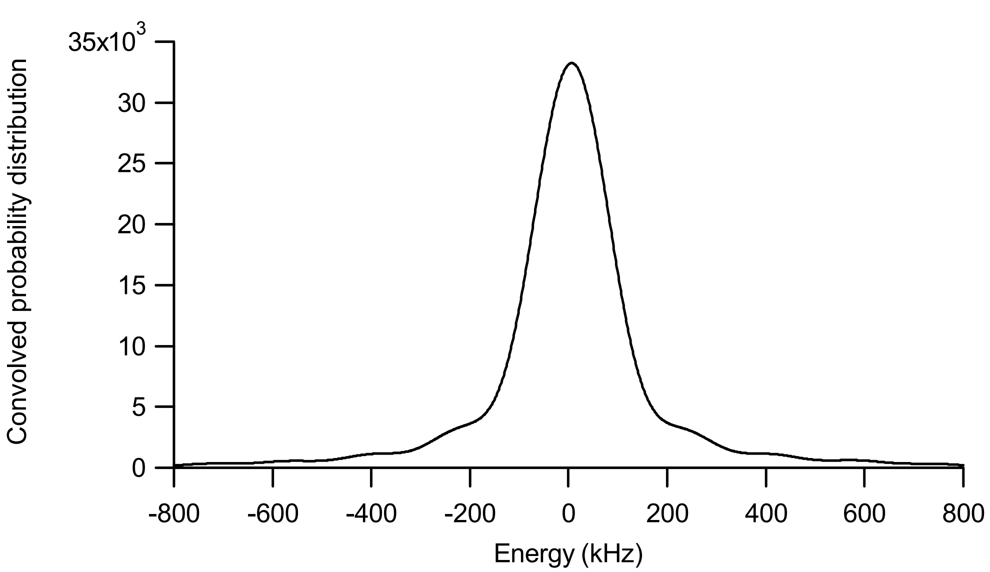

Figure 5-2: The calculated line shape for resonant dipole-dipole line broadening that is the result of convolving the histogram given in Fig. 5-1 with a $\mathrm{sinc}^2(\pi f T)$ function with $T = 6\,\mu$s.

At a Rydberg density of $10^7\,\mathrm{cm}^{-3}$, introduction of the resonant electric dipole-dipole interaction, in the experiments presented in Ch. 4, results in a linewidth broadening of roughly $100 \pm 7\,$kHz. This is in the same order as the broadening obtained from the theoretical model. The main reason for the difference could be the error in estimating the density of Rydberg atoms. This is presented in the next chapter where it is explained that the densities used for analysis of experimental data are uncertain by a factor of 2. Also, multi-body effects were neglected in our estimate. As demonstrated by experimental observations of resonant energy transfer between cold Rydberg atoms [8,9], a more accurate calculation should take multi-body interactions into account.

5.4 Suppression of resonant dipole-dipole interactions by a DC magnetic field

In the calculation presented in the previous section, it was assumed that there was no homogeneous magnetic field present in the experimental region. If the hyperfine structure is neglected, in the absence of dipole-dipole interactions, all 24 states of the two-atom system

$\vert\mathbf{1}\rangle$	$\vert\mathbf{2}\rangle$
$\vert 46d_{5/2}m_j = 1/2\rangle_A \vert 47p_{3/2}m_j = 1/2\rangle_B$	$\vert 47p_{3/2}m_j = -1/2\rangle_A \vert 46d_{5/2}m_j = -1/2\rangle_B$
	$\vert 47p_{3/2}m_j = 3/2\rangle_A \vert 46d_{5/2}m_j = -1/2\rangle_B$
	$\vert 47p_{3/2}m_j = 1/2\rangle_A \vert 46d_{5/2}m_j = 1/2\rangle_B$
	$\vert 47p_{3/2}m_j = -1/2\rangle_A \vert 46d_{5/2}m_j = 3/2\rangle_B$
	$\vert 47p_{3/2}m_j = 3/2\rangle_A \vert 46d_{5/2}m_j = 3/2\rangle_B$

Table 5.1: List of states that are coupled to $|46d_{5/2}m_j = 1/2\rangle_A |47p_{3/2}m_j = 1/2\rangle_B$by resonant dipole-dipole interactions at zero magnetic field.

of the form $|1\rangle = |46d_{5/2}m_{j,A1}\rangle_A |47p_{3/2}m_{j,B1}\rangle_B$ are energy degenerate with all 24 states of the form $|2\rangle = |47p_{3/2}m_{j,A2}\rangle_A |46d_{5/2}m_{j,B2}\rangle_B$. It is this degeneracy which is responsible for the line broadening due to resonant electric dipole-dipole interactions. However, the application of a magnetic field shifts the atomic energy levels due to the Zeeman effect, removing part of the degeneracy of the system. At a non-zero magnetic field, only pairs of states for which $m_{jA1} = m_{jB2}$ and $m_{jA2} = m_{jB1}$ are energy degenerate. For example, consider the state $|46d_{5/2}m_j = 1/2\rangle_A |47p_{3/2}m_j = 1/2\rangle_B$. This state is coupled by $\hat{\mathrm{V}}_{dd}$ to several states as shown in Table 5.1.

All of these states are energy degenerate in the absence of magnetic fields and dipole-dipole interactions. Once a magnetic field is applied, only $|47p_{3/2}m_j = 1/2\rangle |46d_{5/2}m_j = 1/2\rangle$ remains degenerate with state $|1\rangle$, since they have the same Zeeman shift. Since the application of a magnetic field lowers the energy degeneracy within the system, it is expected that it reduces the strength of the resonant dipole-dipole interaction. In this section, a theoretical model is presented that predicts the suppression of the resonant interatomic interactions by an applied magnetic field. The results of this calculation are compared with the experimental data presented in previous chapters.

In the presence of an applied magnetic field and dipole-dipole interaction, the Hamiltonian of the two-atom system can be written as

$$H = \hat{\mathrm{V}}_{dd} + \hat{\mathrm{V}}_{Zeeman}, \tag{5.13}$$

where $\hat{\mathrm{V}}_{dd}$ is given by Eq. 5.2, and $\hat{\mathrm{V}}_{Zeeman}$ is the Zeeman interaction. We consider a magnetic field B applied in the z direction, and take this axis as the quantization axis. With this choice of quantization axis, $\hat{\mathrm{V}}_{Zeeman}$ gives the diagonal elements of the Hamiltonian matrix and does not contribute to off-diagonal elements, since it only couples similar states. This can be expressed as

$$\left\langle \Psi_b \left| \hat{\mathrm{V}}_{Zeeman} \right| \Psi_b^{'} \right\rangle = (\mu_B g_{Jd} m_{jA} + \mu_B g_{Jp} m_{jB}) B, \qquad \text{if } \Psi_b = \Psi_b^{'}, \tag{5.14}$$

$$\left\langle \Psi_b \left| \hat{\mathrm{V}}_{Zeeman} \right| \Psi_b^{'} \right\rangle = 0, \qquad \text{if } \Psi_b \neq \Psi_b^{'}.$$

g_J is the Landé factor and is given by $g_{Jd} = 6/5$, and $g_{Jp} = 4/3$ for d and p state respectively [7]. The Bohr magneton in frequency units is given by $\mu_B = 1.40 \times 10^3\,\mathrm{kHz}\,/\mathrm{G}$. On the other hand, $\hat{V}_{dd}$ does not couple identical states, and only has off-diagonal elements. In finding the matrix elements of $\hat{V}_{dd}$, we observe the following selection rules

$$\left\langle \Psi_a \left| \hat{\mathrm{V}}_{dd} \right| \Psi_b \right\rangle = 0, \tag{5.15}$$

except possibly in cases where $\Delta m_{jA} = 0$ and $\Delta m_{jB} = 0$, or $\Delta m_{jA} = \pm 1$ and $\Delta m_{jB} = \pm 1$.

Using the two-atom states of the form $|1\rangle$ and $|2\rangle$ as the basis set, we will get a 48×48 Hamiltonian matrix for a given R_{AB}, $\hat{n}$, and an applied magnetic field B. The diagonal elements of this matrix are given by Eq. 5.14, and the off-diagonal elements come from the dipole-dipole interactions and are calculated in the exact same manner as presented in the previous section. After writing the Hamiltonian matrix, it is diagonalized to find the energy eigenvalues E_i and corresponding eigenvectors $|\Psi_i\rangle$.

As it was explained in previous chapters, the two-photon $46d_{5/2} - 47d_{5/2}$ transition that was used to probe the interatomic interactions is not sensitive to magnetic fields. Therefore, to compare the result of our simulation with the experimental data, the Zeeman energy contribution is subtracted from each energy eigenvalue

$$E_{ci} = E_i - \left\langle \Psi_i \left| \hat{\mathrm{V}}_{Zeeman} \right| \Psi_i \right\rangle. \tag{5.16}$$

These corrected energies may be calculated for a fixed value of R_{AB}, $\hat{n}$, and B. The distribution of these corrected energies corresponds to the linewidth broadening due to resonant dipole-dipole

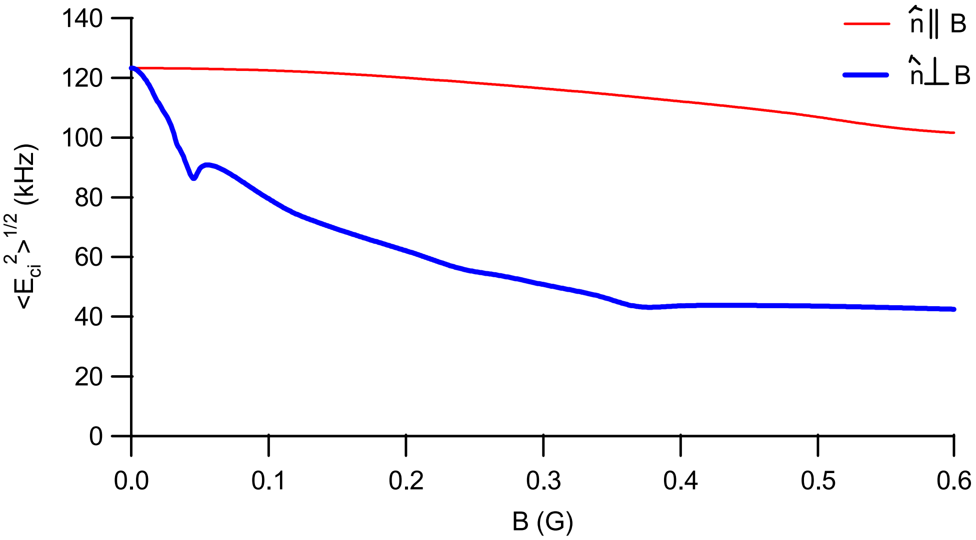

Figure 5-3: Variation of root mean square corrected energies as a function of applied magnetic field for relative orientations of $\hat{n}$ and $\overrightarrow{B}$, and $R_{AB} = 28.5\,\mu\text{m}$.

interactions. As the magnetic field is increased this distribution becomes narrower resulting in a smaller broadening. The application of a magnetic field suppresses the resonant electric dipole-dipole interaction. To show this suppression of interactions numerically, the root mean square of the corrected energies $\left\langle E_{ci}^{2}\right\rangle^{1/2}$ is calculated for $R_{AB} = 28.5\,\mu\text{m}$ as a function of magnetic field B for two cases of $\hat{n} \parallel \overrightarrow{B}$, and $\hat{n} \perp \overrightarrow{B}$. The results of this calculation are shown on Fig. 5-3. The observed reduction in the value of $\left\langle E_{ci}^{2}\right\rangle^{1/2}$ corresponds to a narrower range for the distribution of eigenenergies of the system, or in other words, to smaller resonant dipole-dipole linewidth broadening.

According to Fig. 5-3, the effect of magnetic field on the linewidth broadening is stronger when $\hat{n} \perp \overrightarrow{B}$ than $\hat{n} \parallel \overrightarrow{B}$, at least for fields less than 0.6 G. To justify this difference, we consider the example in Table 5.1, and calculate the dipole-dipole interaction energies $\left\langle 1 \left| \hat{\text{V}}_{dd} \right| 2 \right\rangle$, and the relative Zeeman energy shifts $\left\langle 2 \left| \hat{\text{V}}_{Zeeman} \right| 2 \right\rangle - \left\langle 1 \left| \hat{\text{V}}_{Zeeman} \right| 1 \right\rangle$ for different states involved. This is summarized in Table 5.2. As it is seen on Table 5.2, when $\hat{n}$ is parallel to the direction of the applied magnetic field (the quantization axis), only states of the same $m_{j,tot}$ are coupled by $\hat{\text{V}}_{dd}$, where $m_{j,tot} = m_{j,A} + m_{j,B}$. These states have similar Zeeman shifts compared with states of different $m_{j,tot}$, see the last column of Table 5.2. This is because of the similarity of g_J values

$\|2\rangle$			$\left\langle 2 \middle\| \hat{\mathrm{V}}_{dd} \middle\| 1 \right\rangle$ (kHz)		$\left\langle 2 \middle\| \hat{\mathrm{V}}_{Zeeman} \middle\| 2 \right\rangle - \left\langle 1 \middle\| \hat{\mathrm{V}}_{Zeeman} \middle\| 1 \right\rangle$
$m_{j,A}$	$m_{j,B}$	$m_{j,tot}$	$\hat{n}\|\|\overrightarrow{B}$	$\hat{n} \perp \overrightarrow{B}$	(kHz / G)
$-1/2$	$-1/2$	-1	0	55	-3547
$3/2$	$-1/2$	1	21	-11	187
$1/2$	$1/2$	1	-147	74	0
$-1/2$	$3/2$	1	52	-26	-187
$3/2$	$3/2$	2	0	45	3547

Table 5.2: Non-zero matrix elements $\left\langle 2 \middle| \hat{\mathrm{V}}_{dd} \middle| 1 \right\rangle$ where $|1\rangle = \left|46d_{5/2}m_j = 1/2\right\rangle \left|47p_{3/2}m_j = 1/2\right\rangle$ and $|2\rangle = \left|47p_{3/2}m_{j,A2}\right\rangle_A \left|46d_{5/2}m_{j,B2}\right\rangle_B$, and $R_{AB} = 28.5\,\mathrm{um}$. Also shown are the Zeeman energy shifts of the $|2\rangle$ states relative to $|1\rangle$ state.

for d and p states (6/5 versus 4/3). Therefore, a higher magnetic field is required to break the degeneracy of these states and observe a more significant drop in the linewidth broadening shown on Fig. 5-3. However, when $\hat{n}$ is perpendicular to the magnetic field direction, the selection rule $m_{j,tot} = m_{j,A} + m_{j,B}$ does not apply, and all the states of the form $|2\rangle$ are coupled to the state $|1\rangle$ by $\hat{\mathrm{V}}_{dd}$. Since, the Zeeman shifts of the states with different $m_{j,tot}$ are quite different, as shown on the last column of Table 5.2, a small magnetic field is able to break their degeneracy and have a profound effect on the resonant dipole-dipole line broadening.

In the real case, the interatomic separation R, and the orientation of the unit vector $\hat{n}$ vary randomly over the sample. Therefore, the above calculation should be done for different interatomic separations and different orientations of $\hat{n}$. Using the nearest neighbor probability distribution given in Eq. 5.12, and random orientations of $\hat{n}$, the above calculation is repeated numerous times for different magnetic fields. At each magnetic field, the corrected energies given in Eq. 5.16 are calculated and histogrammed to find the distribution of the energy of the system. Figure 5-4 shows two of these histograms for two different magnetic field magnitudes and a density of $n_{47p_{3/2}} = 8 \times 10^6\,\mathrm{cm}^{-3}$. As the magnetic field is increased, the corrected energies are spread over a smaller energy range showing the suppression of resonant dipole-dipole interaction by a magnetic field.

To compare with the experimental data, these histograms are convolved with a $\mathrm{sinc}^2(\pi f T)$ function with $T = 6\,\mu\mathrm{s}$. In the same manner as the spectra obtained in the experiment, the resultant line shapes are fit with a $\mathrm{sinc}^2(\pi f T)$ function convolved with a Lorentzian of

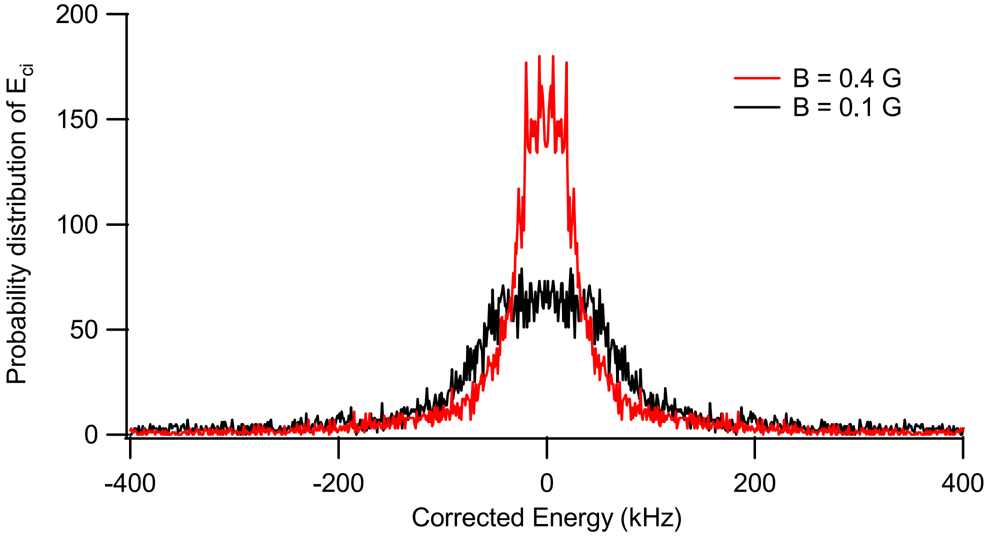

Figure 5-4: Histograms of corrected eigenenergies for two different magnetic field magnitudes. The spread in corrected energies decreases with magnetic field: magnetic field suppresses the resonant electric dipole-dipole interactions.

variable linewidth $\delta\nu$ to obtain the linewidth broadening. To make the comparison with the experimental data, the calculation should be done at the same density as those recorded with the results presented in Ch. 4. However, since our density estimation could contain a 50% error, as it is explained in Appendix A, we adjust the density in the calculation so that the calculated line broadening best fits the experiment. The results of this calculation for two total average Rydberg densities of $1.4\times10^7\text{cm}^{-3}$ and $9.5\times10^6\text{cm}^{-3}$, together with the corresponding experimental data, are shown in Fig. 5-5. The estimated Rydberg densities for high and low density data in Fig. 5-5 were $(8\pm5)\times10^6\text{cm}^{-3}$ and $(5.4\pm3.3)\times10^6\text{cm}^{-3}$ respectively.

The variation of the resonant electric dipole-dipole line broadening as a function of magnetic field is similar in the experimental data and theoretical calculations. However, there is some disagreement, especially at lower magnetic fields: the experimental data seem to extrapolate to lower values for zero magnetic field. The hyperfine structure was neglected in these calculations. This is not a good approximation at lower magnetic fields where the hyperfine splitting exceeds the Zeeman shifts of magnetic sublevels, and can partially suppress resonant interactions.

Another reason for the small disagreement between experimental data and theoretical model

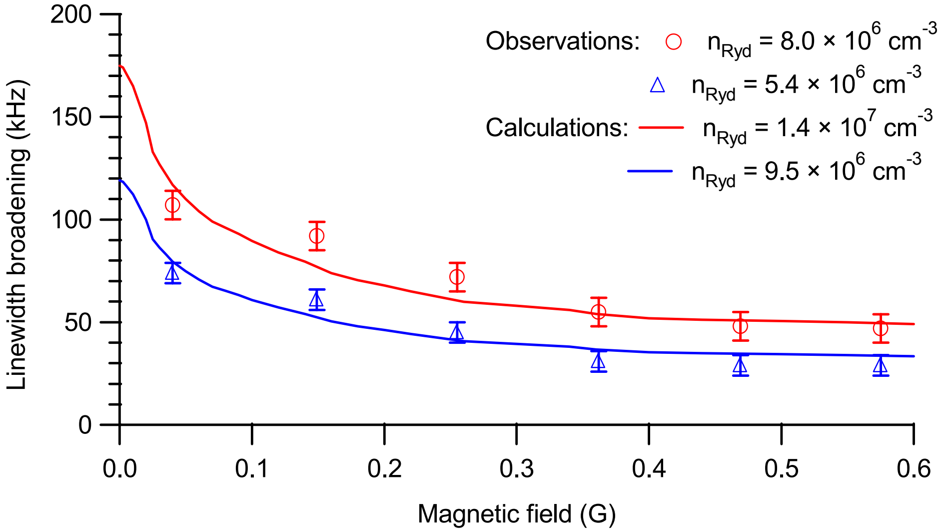

Figure 5-5: Magnetic field suppression of the resonant electric dipole-dipole interactions for two different Rydberg densities. The densities recorded for the experimental data are obtained from density estimations explained in Ch. 6, and the densities used in calculations are the ones that give the best fits to the data.

may be the neglect of multi-body interactions. Experimental observation of the resonant energy transfer between cold Rydberg atoms have demonstrated that this picture in not complete [8, 9]. Also, it is expected that at higher densities the two-body van der Waals interactions which behave as $\frac{1}{R^6}$ become important. Taking these factors into account would further complicate the calculations [10, 11], but should result in a better agreement with the data.

5.5 Conclusion

Calculations of the linewidth broadening due to the resonant dipole-dipole interactions are presented in this chapter. These are of the same order as the linewidth broadening that was obtained in experiments for the same density. The exact comparison of the calculated linewidth broadening with the observed data may not be possible, as the estimated Rydberg density could be off by a factor of 2, and only binary interactions are considered in the calculations.

The other theoretical model that is presented in this chapter predicts the magnetic field partial suppression of resonant electric dipole-dipole interactions. Because of the uncertainty in the estimated Rydberg density, the density was adjusted in the calculation to obtain the best fit to the experimental data. The theory predicts a reduction in the resonant electric dipole-dipole interactions with the magnetic field that is similar to the observed suppression of interactions. The small discrepancies between experiment and theory are possibly due to neglecting the hyperfine structure and many-body interactions.

Bibliography

[1] A. Fioretti, D. Comparat, C. Drag, T. F. Gallagher, and P. Pillet, "*Long-range forces between cold atoms*", Phys. Rev. Lett. **82**, 1839 (1999).

[2] G. K. Woodgate, "*Elementary atomic structure"*, Oxford, 1998.

[3] M. L. Zimmerman, M. G. Littman, M. M. Kash, and D. Kleppner, "*Stark structure of the Rydberg states of alkali-metal atoms*", Phys. Rev. A **20**, 2251 (1979).

[4] D. Vagale, "*Stark Calculations using Matlab*", University of Waterloo, 2003.

[5] S. Chandrasekhar, "*Stochastic problems in physics and astronomy*", Rev. Mod. Phys. **15**, 1 (1943).

[6] W. Demtroder, "*Laser Spectroscopy"*, Springer, Third edition (2003).

[7] H. G. Kuhn, "*Atomic Spectra"*, Longmans, London, 1962.

[8] I. Mourachko, W. Li, and T. F. Gallagher, "*Controlled many-body interactions in a frozen Rydberg gas*" Phys. Rev. A **70**, 031401 (2004).

[9] W. R. Anderson, J. R. Veale, and T. F. Gallagher, "*Resonant dipole-dipole energy transfer in a nearly frozen Rydberg gas*", Phys. Rev. Lett. **80**, 249 (1998).

[10] F. Robicheaux and J. V. Hernández, "*Many-body wave function in a dipole blockade configuration*", Phys. Rev. A **72**, 063403 (2005).

[11] J. S. Fraiser, V. Celli, and T. Blum, "*Resonant processes in a frozen gas*", Phys. Rev. A **59**, 4358 (1999).

Chapter 6

Summary and Future Work

6.1 Summary of research

6.1.1 Observation of the resonant electric dipole-dipole interaction between ultracold Rydberg atoms using microwave spectroscopy

Resonant electric dipole-dipole interactions between ultracold Rydberg atoms have been studied both experimentally and theoretically. In the experimental part, line broadening in the microwave spectra of cold Rydberg atoms due to the resonant electric dipole-dipole interaction has been observed using a combination of laser and microwave excitations of Rydberg states. In this observation, microwave transitions between Rydberg states of cold rubidium atoms have been used both to introduce and to probe the resonant electric dipole-dipole interaction. Rydberg atoms were produced using optical excitation of laser cooled and trapped ^{85}Rb atoms. To introduce interatomic interactions, a fraction of these atoms was transferred to another Rydberg state by microwaves. The linewidth broadening of a two-photon microwave transition between Rydberg states was used to probe the resonant electric dipole-dipole interaction. Using this technique, it has been observed that introduction of interatomic interactions broadens the linewidth of the two-photon probe transition. The observed line broadening increases linearly with the density of interacting atoms, which is consistent with the $1/R^3$ dependence of the dipole-dipole interaction.

A theoretical model has been presented that predicts the linewidth broadening due to the resonant electric dipole-dipole interaction. In this calculation, it has been assumed that each Rydberg atom interacts resonantly with its nearest neighbour. The simulated line broadening for a given Rydberg density is of the same order of magnitude as observed in the experiment.

6.1.2 Magnetic field suppression of the resonant electric dipole-dipole interaction

The effect of magnetic fields on the resonant electric dipole-dipole interaction has also been studied both experimentally and theoretically. It has been observed that a homogeneous magnetic field suppresses resonant interactions. For this observation, the resonant dipole-dipole experiment has been performed at a fixed Rydberg density when a calibrated magnetic field is varied from zero to $0.6\,\mathrm{G}$. The effect of magnetic fields is to remove the energy degeneracy of different magnetic sublevels and, therefore, reduce the number of resonant coupled states. This is the basis of a theoretical model that predicts the suppression of resonant electric dipole-dipole interactions. The predicted reduction in the strength of resonant interatomic interactions agrees with that observed in the experiment, especially for higher magnetic fields. At lower magnetic fields, there is a discrepancy between theory and experiment that could be because of neglecting the hyperfine structure. The theoretical model does not take into account the suppression of resonant interactions due to hyperfine splitting, which becomes more important than the Zeeman shift at low magnetic fields. Another problem with the theoretical model is the assumption of binary interactions. Mourachko et al. [1] have demonstrated that the dipole-dipole interaction is indeed a many-body effect. Therefore, a more accurate model should take into account multi-body interactions, which would complicate the calculations [2,3].

6.1.3 Development of a novel technique for sensitive measurement of magnetic fields

To study the effect of magnetic fields on the resonant electric dipole-dipole interaction, a calibrated magnetic field should be applied. This magnetic field has been generated using a pair of compensating coils of the MOT setup. A novel technique has been developed that uses the microwave spectroscopy of Rydberg atoms to calibrate the magnetic field in the experimental apparatus. This technique is based on the fact that the frequency change, as a function of the magnetic field, of the microwave transition between some of the hyperfine sublevels of Rydberg states depends only on the magnetic field and not on the hyperfine spacing of energy levels. Using this method has made it possible to calibrate the homogeneous magnetic field within the MOT to an accuracy of ±10mG, and put an upper bound of 17mG on any remaining inhomogeneity.

6.2 Future Work

The resonant electric dipole-dipole interaction that has been observed and discussed in this work may be used for the realization of the *dipole blockade* proposed by Lukin *et al.* [4]. The dipole blockade is achieved by interactions between atoms excited to the same Rydberg state. An electric field should be applied in this case to tune the Rydberg interactions into resonance.

To further study the magnetic field suppression of the resonant electric dipole-dipole interaction, especially the angular dependence of this phenomenon as predicted by the presented theoretical model, a one-dimensional sample of Rydberg atoms could be produced. This may be achieved by focussing down the excitation laser so that the beam waist across the sample is less than the average interatomic separation [5]. By changing the orientation of the applied magnetic field relative to the excitation laser, the two cases of $\hat{n} \parallel B$ and $\hat{n} \perp B$ may be studied individually.

As demonstrated in this research, homogeneous magnetic fields cannot completely suppress the resonant dipole-dipole interaction. The reason for this is that there are some states that will remain energy degenerate, and interact resonantly, even in very large magnetic fields; for instance, $|46d_{5/2}, 5/2\rangle\, |47p_{3/2}, 3/2\rangle$and $|47p_{3/2}, 3/2\rangle\, |46d_{5/2}, 5/2\rangle$. Inhomogeneous magnetic fields, however, may be used to obtain perfect suppression of resonant interactions by producing space dependent Zeeman shifts. If the field inhomogeneity is large enough, the resonant condition may be spoiled completely. Strong magnetic field gradients have recently been used in electron spin resonance (ESR) to suppress spin diffusion due to the magnetic dipolar flip-flop interaction [6]. An analogous experiment could be performed in the case of resonant electric dipole-dipole interactions. The observed line broadening due to the resonant electric dipole-dipole interaction is roughly $100\,\text{kHz}$ for an average interatomic separation of $30\,\mu\text{m}$.

Considering Zeeman shifts of $1\,\mathrm{MHz}\,/\,\mathrm{G}$, a magnetic field inhomogeneity of roughly $50\,\mathrm{G}\,/\,\mathrm{cm}$ is necessary to achieve significant suppression of the resonant dipole-dipole interaction. This field inhomogeneity is achievable in magnetic microtraps for example [7].

Bibliography

[1] I. Mourachko, W. Li, and T. F. Gallagher, "*Controlled many-body interactions in a frozen Rydberg gas*" Phys. Rev. A **70**, 031401 (2004).

[2] F. Robicheaux and J. V. Hernández, "*Many-body wave function in a dipole blockade configuration*", Phys. Rev. A **72**, 063403 (2005).

[3] J. S. Fraiser, V. Celli, and T. Blum, "*Resonant processes in a frozen gas*", Phys. Rev. A **59**, 4358 (1999).

[4] M. D. Lukin, M. Fleischhauer, R. Cote, L. M. Duan, D. Jaksch, J. J. Cirac, and P. Zoller "*Dipole Blockade and quantum information processing in mesoscopic atomic ensembles*", Phys. Rev. Lett. **87**, 037901 (2001).

[5] T. J. Carrol, K. Claringbould, A. Goodsell, M. J. Lim, and M. W. Noel, "*Angular dependence of the dipole-dipole interaction in a nearly one-dimensional sample of Rydberg atoms*" Phys. Rev. Lett. **93**, 153001 (2004).

[6] R. Budakian, H. J. Mamin, and D. Rugar, "*Suppression of spin diffusion near a micron-size ferromagnet*", Phys. Rev. Lett. **92**, 037205 (2004).

[7] R. Folman, P. Krüger, J. Schmiedmayer, J. Denschlag, and C. Henkel, "*Microscopic atom optics: from wires to an atom chip*", Adv. At. Mol. Opt. Phys. **48**, 263 (2002).

Appendix A

Rydberg Atom Density Measurement

A.1 Introduction

As mentioned in previous chapters, the resonant dipole-dipole interaction is a density dependent effect. This is because of the dependence of dipole-dipole interaction potential to interatomic separation. Therefore, it is necessary to estimate the Rydberg atom density for the experiments presented in this thesis. It is explained later in this chapter that the cold atom sample has a Gaussian profile; hence, the density of Rydberg atoms varies over the sample. Because of this, the comparison of line broadening is made using the average Rydberg density. Estimation of the average density of cold Rydberg atoms requires knowing the total number of these atoms produced by photoexcitation, and their spatial profile. This density depends on the spatial profile of the excitation laser, its power, the number of the trapped atoms, and their profile. In this chapter, the estimation of the number of cold Rydberg atoms is presented in the first section. To determine the spatial profile of the Rydberg atoms requires evaluating the trap and the laser beam profiles. These measurements are explained in the following sections.

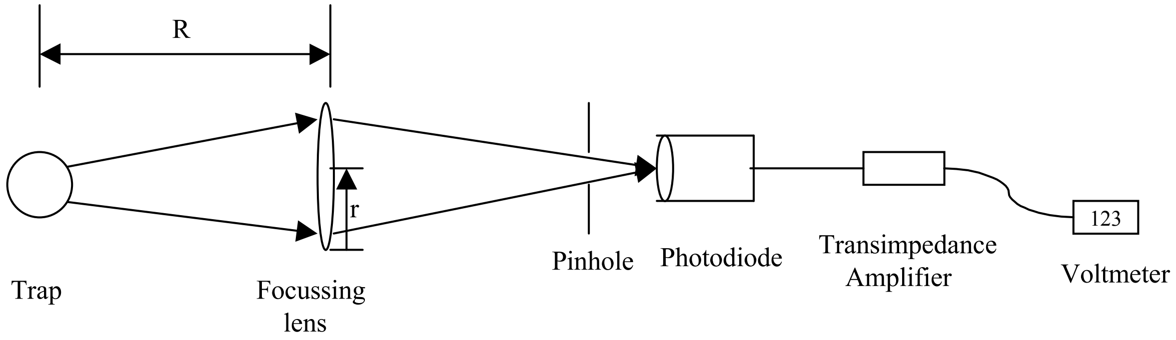

Figure A-1: Measuring the trap fluorescence in order to calibrate the microchannel plate detector.

A.2 Estimate of the total number of Rydberg atoms

The number of cold Rydberg atoms was obtained by calibrating the gain of the microchannel plate detector (MCP). This calibration was done in two different ways. Once, by measuring the number of ions produced in photoionization of a known number of $5p_{3/2}$ atoms and comparing to the signal detected by MCP. The second method was observing the average total charge due to single events at higher bias voltages than normal operating conditions of MCP.

A.2.1 MCP calibration using photoionization

To estimate the number of ions produced in photoionization of $5p_{3/2}$ atoms we need to know the number of these atoms, the ionization laser power, and the ionization cross-section. The total number of $5p_{3/2}$ atoms was estimated by measuring the fluorescence of trapped atoms using a photodiode. The schematic of the setup used for this measurement is given in Fig. A-1.

The trap fluorescence light was collected and focussed onto a photodiode (Thorlabs Inc, FDS100) using a lens, and a pinhole was used before the photodiode to block the scattered light and reduce the background light relative to the trap fluorescence. The photodiode output was amplified and then measured using a voltmeter. This measurement was done with the trap on and then off to correct for the background light contribution. Because of the finite collection angle, the measured signal represents a fraction of the total number of photons emitted by $5p_{3/2}$ atoms; therefore, it was multiplied by a correction factor to reflect the total number of emitted

Amplifier gain (V/A)	10^8
Trap fluorescence (V)	0.71 ± 0.01
Photodiode responsivity (A/W)	0.5
Transmission factor for fused silica	0.92
Power received by photodiode (W)	$(3.95 \pm 0.05) \times 10^{-6}$
Emitted photon wavelength (nm)	780
Photon energy (J)	2.55×10^{-19}
Lifetime of Rb $5p_{3/2}$ (s) [1]	26.63×10^{-9}
Power emitted by each atom (W)	9.4×10^{-12}
Number of $5p_{3/2}$ atoms	$(4.2 \pm 0.3) \times 10^5$

Table A.1: Sample measurement of the number of $5p_{3/2}$ atoms.

photons. This correction factor is given by $4\pi R^2/\pi r^2$, where R is the trap lens distance, and r is the lens radius. For the setup in Fig. A-1, $R = 4\,\text{in}$, and $r = 0.5\,\text{in}$; therefore, the finite angle correction factor was 256. We should also account for the finite transmission of the fused silica window of the trap, and the responsivity of the photodiode at 780 nm. The room background light should be excluded from our measurements.

In one experiment, with an amplifier gain of 10^8 V / A, the amplified photodiode voltage was 3.13 ± 0.005 V and 2.42 ± 0.005 V for the trap being on and off respectively; therefore, the net voltage due to the trap fluorescence is 0.71 ± 0.01 V. A sample measurement, which considers all the factors mentioned above, is given in Table A.1.

For ionizing $5p$ atoms a pulsed dye laser pumped by the third harmonic (355 nm) of a nanosecond pulsed YAG laser (Spectron Laser Systems, SL858G-SLM) was used. The wavelength of the dye laser was tuned above the ionization potential of the $5p$ state of rubidium ($\sim$ 477 nm), and was sent into the trap through a fused silica window. The output power of this laser was measured by a pyroelectric detector to be $\sim 1\,\mu$J. The laser beam hits eight surfaces (six mirrors and two prisms) after the output mirror and before hitting the trap. The reflection efficiency for each mirror given by the company (CVI Laser Optics) is 0.965, and the transmission efficiency of the fused silica (prism) for 480 nm is roughly 96% (Melles Griot Optics Guide). Therefore, the power in the trap was: $1 \times 10^{-6}\,\text{J} \times (0.965)^6 \times (0.96)^2 = 7.44 \times 10^{-7}\,\text{J}$. The photon energy for the ionization laser with $\lambda = 477.6\,\text{nm}$ is given by $hc/\lambda = 4.16 \times 10^{-19}$ J /photon; therefore, the number of photons hitting the trap is

$N_{Ph} = 7.44 \times 10^{-7}\,\mathrm{J}/(4.16 \times 10^{-19}\,\mathrm{J}/\mathrm{photon}) = 1.79 \times 10^{12}$ photons.

The column density that indicates the number of atoms per unit area is $C = 0.833 N_A / (FWHM)^2_{||}$, where $(FWHM)_{||}$ is the full width at half maximum of the profile of the cloud of trapped atoms in the direction of ionization laser. This profile was obtained in two ways: 1) by 780 nm fluorescence imaging of the trap, 2) by scanning the Rydberg excitation laser (480 nm) across the trap and measuring the number of excited Rydberg atoms. In the first method, after taking the trap image with a CCD camera, it was fit with a Gaussian profile to obtain the trap FWHM. This measurement resulted in $(FWHM)_{||} = 0.54 \pm 0.05\,\mathrm{mm}$, and $(FWHM)_{\perp} = 0.62 \pm 0.05\,\mathrm{mm}$, where $\perp$ labels the direction perpendicular to the laser beam. The trap size depends on the cooling and trapping and repump beam sizes and also the Rb pressure in the trap (dictated by the current of the Rb dispenser).

In the second method, the Rydberg excitation laser frequency was tuned to excite a specific Rydberg state; then, this laser was scanned across the trap and the Rydberg signal was measured. Scanning of the laser direction was performed by turning the mirror that directs the laser into the trap using a stepper motor driver (Newport, ESP300). Figure A-2 shows an example of the variation of the detected Rydberg ion signal as the laser is scanned across the trap. The data was then fit with a Gaussian profile to find the FWHM of the signal. This measurement was performed both with and without switching the AHCs off, resulting in $(FWHM)_{\perp} = 0.55 \pm 0.05\,\mathrm{mm}$, and $(FWHM)_{\perp} = 0.82 \pm 0.05\,\mathrm{mm}$ respectively. It was not possible to obtain the $(FWHM)_{||}$ with this method because of the limited optical access to the MOT. However, the similarity of the results obtained for $(FWHM)_{\perp}$ in the two methods confirms that the fluorescence imaging measurement is valid to within 10%.

The ionization cross section for $5p_{3/2}$ state of rubidium is given as $\sigma = 13 \times 10^{-22}\,\mathrm{m}^2$ [2]. The number of ions produced by photoionization of $5p_{3/2}$ atoms is $N_{ions} = C\sigma N_{Ph} = 7.37 \times 10^{11}\,\mathrm{m}^{-2} \times 13 \times 10^{-22}\,\mathrm{m}^2 \times 1.79 \times 10^{12} = 1710 \pm 120$ ions. The average amplified boxcar voltage corresponding to this number of ions was $1.6 \pm 0.2\,\mathrm{V}$; therefore, the calibration factor for converting the boxcar voltage to number of ions is $(1710 \pm 120)/(1.6 \pm 0.2)\,\mathrm{V} = 1100 \pm 200$ ions/ V.

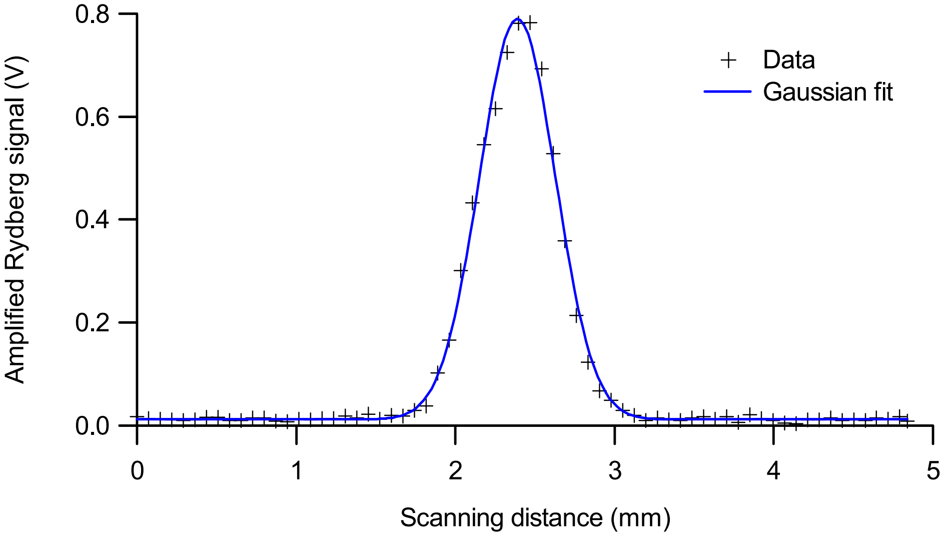

Figure A-2: Measurement of the FWHM of the trap by scanning the Rydberg excitation laser across the trap.

A.2.2 MCP calibration using single particle pulses

The calibration of the gain of the MCP was also done using single particle pulses. In this method, the average total charge due to single particles was measured at a higher bias voltage (1700 V) of the MCP relative to the normal operating voltage (1530 V). Then, to determine the MCP gain at the operating voltage, a series of measurements were taken at constant charged particle signal level with variable bias voltages. To measure the total charge due to a single particle pulse, we shine a light into the vacuum chamber when setting the MCP bias voltage at 1700 V. The area under the pulse is measured on an oscilloscope for different trigger levels, and the data is extrapolated to find the single particle signal. This data, which is shown on Fig. A-3, results in a value of $(130 \pm 15)\times 10^{-12}$ V s for the area under a single particle signal.

Determination of the MCP gain requires knowledge of the absolute detection efficiency. The absolute detection efficiency of an MCP depends on the kinetic energy at impact, the species involved, and surface conditions [3]. A recommended efficiency for our specific conditions was not available. Based on information from the manufacturer and from the literature [3], an initial detection efficiency of 50% was estimated; however, this could be as high as 80% or as low as 20%. Calculation of the gain of the MCP at 1700 V is summarized in Table A.2.

MCP detection efficiency [3]	0.5
Area/pulse at 1700 V	$(130 \pm 15)\times10^{-12}$ V s
Boxcar width	160 ns
Boxcar gain	50 mV
MCP gain	$(8.1 \pm 0.9)\times10^{-3}$ V /ion

Table A.2: The MCP gain calibration using single particle pulses.

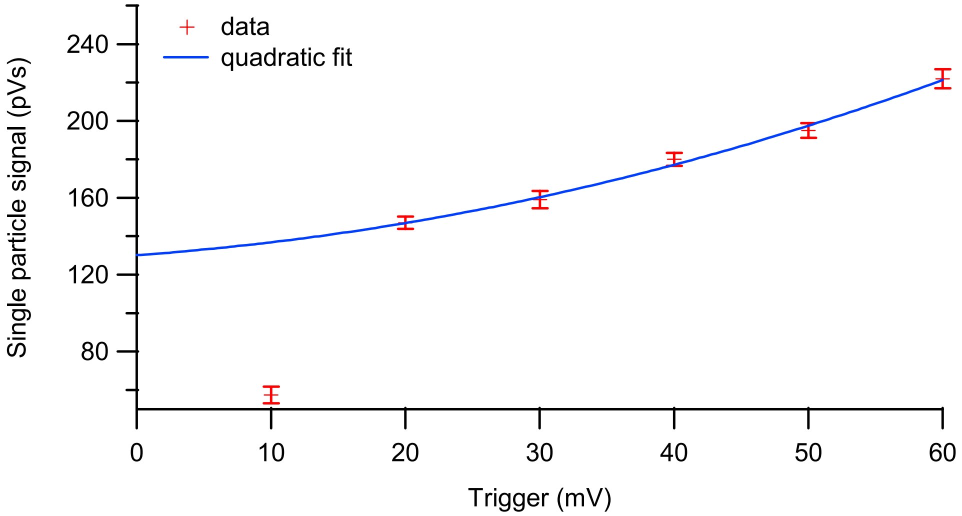

Figure A-3: Single particles areas as a function of scope trigger level at MCP voltage of 1700 V.

The MCP operating voltage for the experiments done in this thesis was 1530 V; therefore, the MCP calibration should be obtained for this voltage. To this end, the MCP gain at 1700 V should be related to that of 1530 V. To do this, we compare the time averaged field ionization signal corresponding to a Rydberg state (for example $46d_{5/2}$) for these MCP voltages. This was done in a single step going from 1700 V to 1530 V with a fixed signal level, and also in two steps with different signal levels (first step 1700 V to 1600 V, and second 1600 V to 1530 V). The conversion factor obtained in this way that should be used to get the gain at 1530 V from the gain at 1700 V is $(10 \pm 0.5)^{-1}$. Therefore, the MCP gain for our operating voltage of 1530 V is given by $(8.2 \pm 1)\times10^{-4}$ V /ion, or 1240 ± 150 ions/V. This is in good agreement with the gain factor of 1100 ± 200 ions/ V that was obtained from photoionization of $5p_{3/2}$ atoms.

A.3 Density measurement

As it was explained at the beginning of this chapter, since the density of Rydberg atoms varies over the sample of cold atoms, the interatomic interactions are compared with the spatially averaged Rydberg density. The average density of Rydberg atoms is obtained from

$$\bar{n} = \frac{\displaystyle\int_0^\infty \left[n\left(\overrightarrow{r}\right)\right]^2 dV}{\displaystyle\int_0^\infty n\left(\overrightarrow{r}\right) dV}, \tag{A.1}$$

where $n\left(\overrightarrow{r}\right)$ is the density distribution function and is given by

$$n\left(\overrightarrow{r}\right) = n_0 \exp\left[-\frac{(4\ln 2)z^2}{(FWHM_{||})^2}\right] \exp\left[-\frac{(4\ln 2)x^2}{(FWHM_{\perp})^2}\right] \exp\left[-\frac{(4\ln 2)y^2}{(FWHM_{\perp})^2}\right], \tag{A.2}$$

where $FWHM_{||}$ is the full width at half maximum of the Gaussian profile of the trap, $FWHM_{\perp}$ is the full width at half maximum of the irradiance profile of the excitation laser in x and y directions, and n_0 is the peak Rydberg density. Evaluating the integrals in A.1 gives $\bar{n} = \left(\frac{1}{2}\right)^{3/2} n_0$.

Since it is the total number of Rydberg atoms that we obtain from the calibration of the MCP gain, we should derive an expression for the peak Rydberg density as a function of the total number of Rydberg atoms. If the waist of the excitation laser is smaller than the width of the trap profile, and it does not change significantly over the size of the trap, the total number of Rydberg atoms is obtained from

$$N_{Ryd} = \int_{-\infty}^{\infty}\int_{-\infty}^{\infty}\int_{-\infty}^{\infty} n_0 \exp\left[\frac{-(4\ln 2)z^2}{(FWHM_{||})^2}\right] \exp\left[\frac{-(4\ln 2)x^2}{(FWHM_{\perp})^2}\right] \exp\left[\frac{-(4\ln 2)y^2}{(FWHM_{\perp})^2}\right] dxdydz. \tag{A.3}$$

From Eq. A.3 an expression for peak Rydberg density in terms of the total Rydberg atoms is obtained:

$$n_0 = \left(\frac{4\ln 2}{\pi}\right)^{3/2} \frac{N_{Ryd}}{(FWHM_{\perp})^2\ (FWHM_{||})}. \tag{A.4}$$

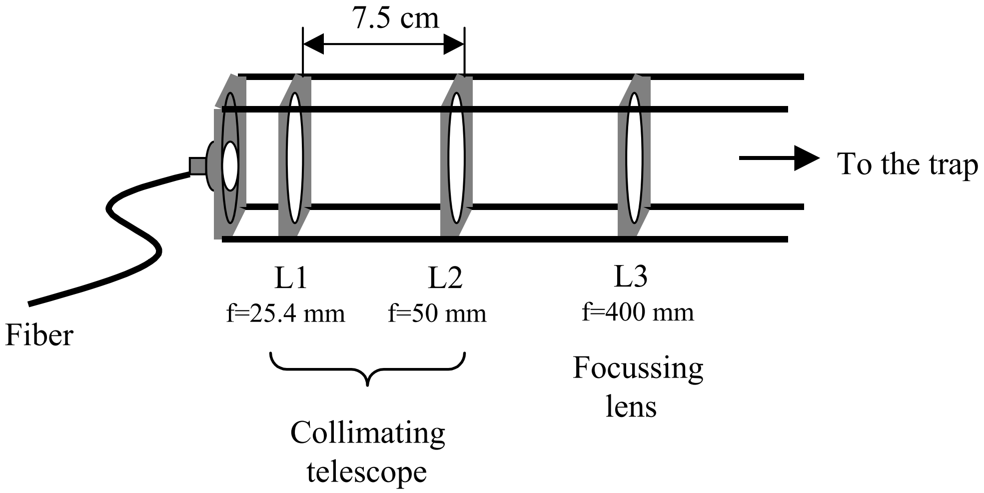

Figure A-4: Collimating and focussing assembly used to collimate the 480 nm laser beam at the output of the fiber, and focus it into the trap. L1 and L2 are the two lenses used for collimation, and L3 is the focussing lens. Part numbers: L1: Thorlabs LA1951, L2: Thorlabs LA4148, and L3: Thorlabs LA1172.

Therefore, the average Rydberg density is obtained from the following formula

$$\bar{n} = \left(\frac{2\ln 2}{\pi}\right)^{3/2} \frac{N_{Ryd}}{(FWHM_{\perp})^2\ (FWHM_{||})}. \tag{A.5}$$

A.4 Laser beam spot size measurement

The frequency doubled output of a single frequency cw Ti: sapphire laser (Coherent MBR-110) was used for the excitation to Rydberg states. To shape the output of this laser, and also to avoid the need for daily realignment of it into the trap, it was coupled into a single mode fiber. The output of the fiber was collimated using a two-lens telescope and then focussed into the trap using a lens. This assembly is shown in Fig. A-4.

The output end of the fiber, the collimating telescope, and the focussing lens were mounted on four rods. This way, the telescope configuration and its distance to the fiber were kept fixed in order to maintain a collimated laser beam with a fixed beam size. Also, it was possible to slide the focussing lens on these rods to change the laser beam spot size in the trap. The output beam assembly was moved to an optical table for the beam spot size measurements since it was not possible to do this measurement within the vacuum chamber.

Measurement of the waist of the ionization laser was done utilizing the scanning knife-edge beam profile measurement technique [4]. In this technique, a knife-edge is scanned through the laser beam while monitoring the drop in the laser beam power using a photodiode. The knife-edge was scanned using a stepper motor driver (Newport ESP300) that was controlled by a LabView program that was also used to collect the data corresponding to the transmitted laser power. The data was then plotted and fit by the function given in Eq. A.6 to obtain the width of the laser beam;

$$f(x) = c_1 + c_2/2 \times \left\{ 1 + \mathrm{erf}\left[\frac{\sqrt{2}(x - c_3)}{c_4} \right] \right\}, \tag{A.6}$$

where c_1, c_2, c_3, and c_4 are factors corresponding to offset, amplitude, center, and waist of the obtained curve. This function gives the transmitted laser power as the knife-edge is scanned through the laser beam, and is obtained by integrating the Gaussian profile of the laser beam in two dimensions.

This measurement was done in horizontal and vertical directions (x and y) for a few different points throughout the focal region. Figure A-5 shows one of these scans. The laser beam spot size as a function of the distance from the beam waist at the focus is plotted in Fig. A-6 for both x and y directions. These curves are fit by a Gaussian beam form [5] to get the waists of the beam in the two directions;

$$f(z) = w_0 \left\{ \left[1 + \left(\frac{z - z_0}{\pi w_0^2 / M_2 \lambda} \right)^2 \right] \right\}^{1/2}, \tag{A.7}$$

where w_0 is the waist, z_0 is the position of the waist, λ is the wavelength, and M_2 is a parameter describing the deviation from a perfect Gaussian profile [5].

There are some density dependent processes in the trap that were used to locate the laser beam focus in the MOT. The Rydberg density was varied by moving the focussing lens L3 in Fig. A-4 relative to the trap. Ionizing collisions between Rydberg atoms are examples of density dependent processes that should increase with density. The resultant ion signal, which is marked with ions in Fig. A-7, is observed at earlier times in field ionization spectra. The normalized ion signal (resulting from density dependent processes) in terms of the total ion

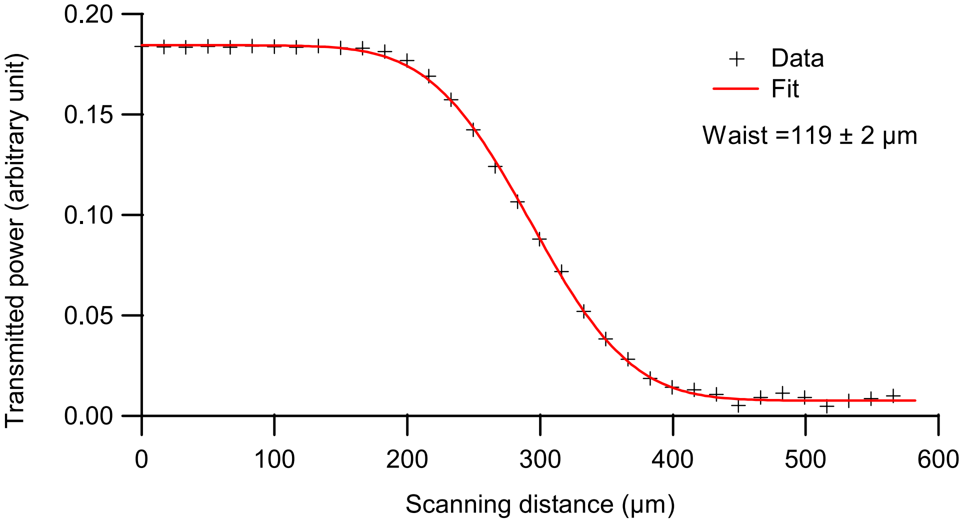

Figure A-5: Measurement of the width of the excitation laser beam by scanning knife-edge technique. The beam waist at the measurement location is obtained from fitting the data by the knife-edge function.

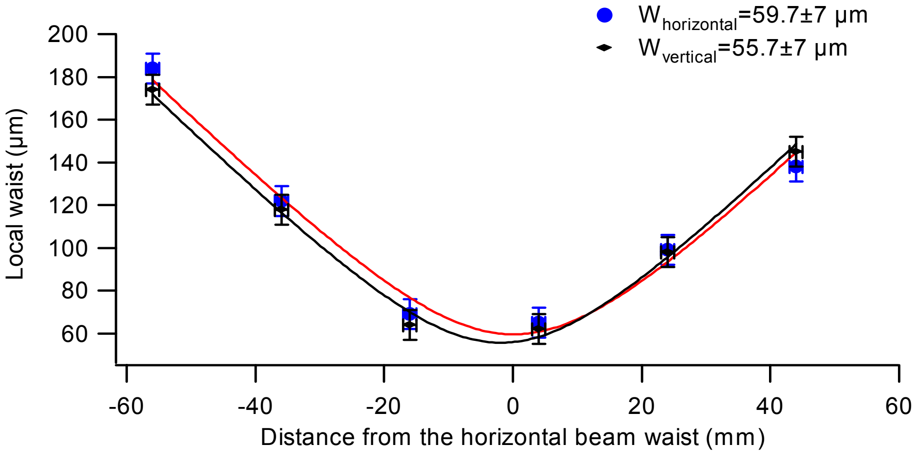

Figure A-6: Rydberg excitation beam waist measurement. To find the waist of the laser beam at the focus, the beam waist is plotted as a function of distance from the focus, and fit with waist function. The beam waists for the two orthogonal directions normal to the propagation direction are shown.

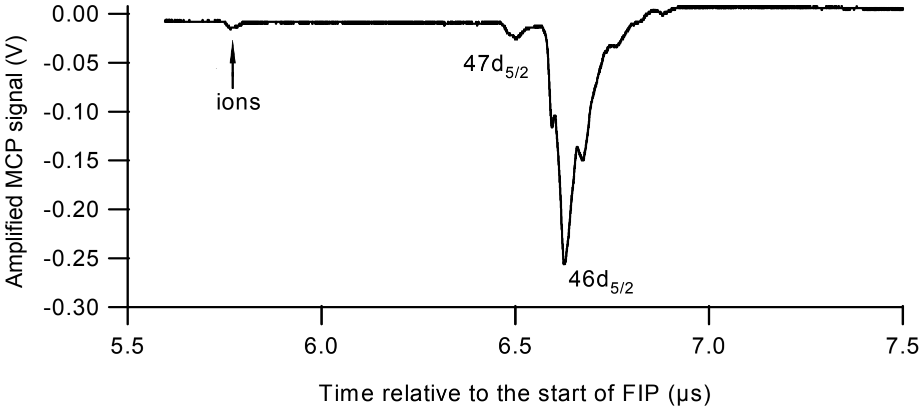

Figure A-7: Amplified microchannel plate detector signal for Rydberg states and ions produced by density dependent processes.

signal for different positions of the focussing lens is shown in Fig. A-8. The normalized ion signal level was then tabulated for a given total ion signal, and plotted in terms of the focussing lens position. This is shown in Fig. A-9. According to this figure, for the lens L3 used in Fig. A-4, the tightest focus hits the trap when L3 is a distance $43.5 \pm 0.5\,\mathrm{cm}$ away from the trap.

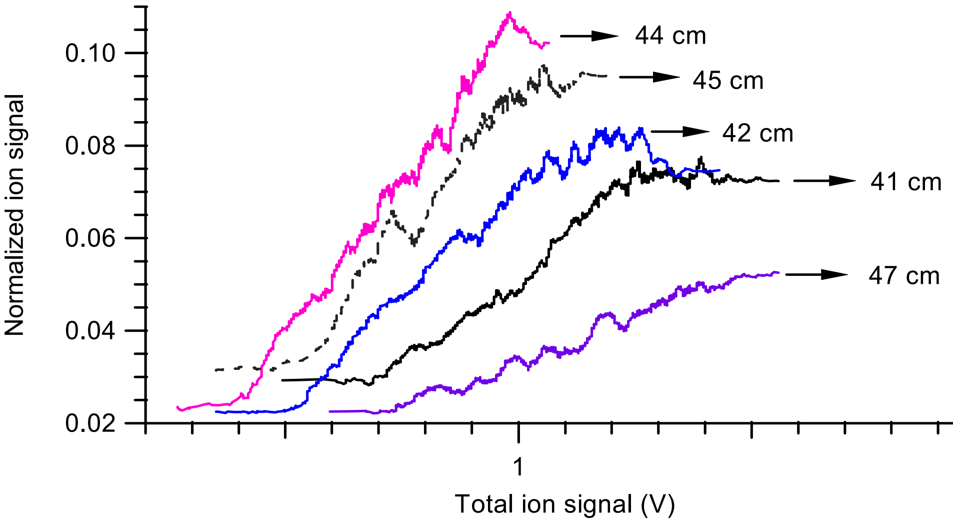

Figure A-8: Normalized free ion signal in terms of total ion signal for different focussing lens distances from the trap, which label each set of data.

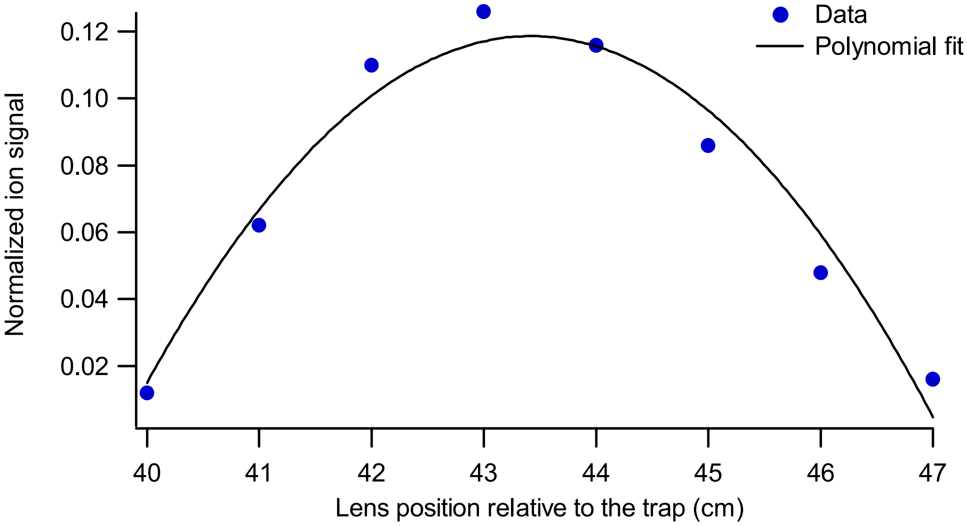

Figure A-9: Finding the position of the tightest focus of the laser with respect to the trap. Data shows the normalized free ion signal level for a given total ion signal and different lens positions. Data is fit with a polynomial function to find the focus position which is located a distance 43.5 ± 0.5 cm from the trap.

A.5 Conclusion

To estimate the average Rydberg density in the cold atom sample, the total number of Rydberg atoms produced by photoexcitation and the spatial profile of the Rydberg atoms are needed. Two different techniques for measuring the total number of Rydberg atoms were used. Both techniques used calibration of the MCP gain, and resulted in similar answers. In one method, the number of ions produced by photoionization of $5p_{3/2}$ atoms was estimated and compared to the signal detected by the MCP. Difficulties in estimating the number of excited atoms ($5p_{3/2}$), and obtaining the trap profile using fluorescence imaging limits the accuracy of this method. The problems in estimating the number of excited atoms come from the fact that we cannot directly measure the focusing lens-trap separation in Fig. A-1. On the other hand, depending on how well the trap image is focussed onto the CCD camera used for fluorescence measurement, we may get different answers for the size of the cloud of trapped atoms.

In the second method, the MCP gain was calibrated using single particle pulses. The lack of accurate knowledge of the MCP detection efficiency is the biggest limitation in this method. In this estimate a detection efficiency of 0.5 was used. However, depending on the conditions (particles involved, energy of particles at impact, and MCP surface conditions [3]) the detection efficiency can change by 50%.

Bibliography

[1] H. J. Metcalf, and P. van der Straten, "*Laser cooling and trapping*", Springer 1999.

[2] I. D. Petrov, V. L. Sukhorukov, E. Leber, and H. Hotop, "*Near threshold photoionization of excited alkali atoms Ak(np) (Ak=Na, Rb, Cs; n=3-6)*", The European Physical Journal D **10**, 53-65 (2000).

[3] G. W. Fraser, "*The ion detection efficiency of microchannel plates (MCPs)*", Int. J. Mass Spectrom. **215**, 13 (2002).

[4] Y. Suzaki and A. Tachibana, "*Measurement of* μm *sized radius of Gaussian laser beam using the scanning knife-edge*", Appl. Opt. **14** (12), 2809 (1975).

[5] A. E. Siegman, "*Lasers*", Mill Valley, California, 1986.

Appendix B

MBR and MBD Conditions for Excitation of Some Rydberg States

Rydberg State	λ_{MBR} (vac) (nm)	MBR Conditions	MBD Power (mW)
$46d_{5/2}$	960.650 ± 0.005	Stable	$80 - 90$
$48s_{1/2}$	960.628 ± 0.005	Stable	$80 - 90$
$45d_{5/2}$	960.771 ± 0.005	Unstable	30
$44d_{5/2}$	960.868 ± 0.005	Stable	50
$34s_{1/2}$	963.436 ± 0.005	Stable	60
$32s_{1/2}$	964.189 ± 0.005	Unstable	40

Table B.1: MBR and MBD conditions for some Rydberg state excitations.